Journal of Engineering Mathematics **39:** 261–343, 2001.

Asymptotic adaptive methods for multi-scale problems in fluid mechanics

R. KLEIN[1,2], N. BOTTA[2], T. SCHNEIDER[1,3], C. D. MUNZ[4], S. ROLLER[4], A. MEISTER[5], L. HOFFMANN[5] and T. SONAR[5]
[1]*FB Mathematik & Informatik, Freie Universität Berlin, Konrad Zuse Zentrum für Informationstechnik, Takustr. 7, 14195 Berlin, Germany (e-mail: rupert.klein@zib.de)*
[2]*Potsdam Institut für Klimafolgenforschung, Germany*
[3]*Konrad-Zuse-Zentrum für Informationstechnik, Berlin, Germany*
[4]*Institut für Aerodynamik und Gasdynamik, Universität Stuttgart, Germany*
[5]*Institut für Angewandte Mathematik, Universität Hamburg, Germany*

Received 14 February 2000; accepted in revised form: 25 September 2000

Abstract. This paper reports on the results of a three-year research effort aimed at investigating and exploiting the role of physically motivated asymptotic analysis in the design of numerical methods for singular limit problems in fluid mechanics. Such problems naturally arise, among others, in combustion, magneto-hydrodynamics, and geophysical fluid mechanics. Typically, they are characterized by multiple-space and/or -time scales and by the disturbing fact that standard computational techniques fail entirely, are unacceptably expensive, or both. The challenge here is to construct numerical methods which are robust, uniformly accurate, and efficient through different asymptotic regimes and over a wide range of relevant applications. Summaries of multiple-scales asymptotic analyses for low-Mach-number flows, magneto-hydrodynamics at small Mach and Alfvén numbers, and of multiple-scales atmospheric flows are provided. These reveal singular balances between selected terms in the respective governing equations within the considered flow regimes. These singularities give rise to problems of severe stiffness, stability, or to dynamic-range issues in straight-forward numerical discretizations. A formal mathematical framework for the multiple scales asymptotics is then summarized by use of the example of multiple-length-scale single-time-scale asymptotics for low-Mach-number flows. The remainder of the paper focuses on the construction of numerical discretizations for the respective full governing equation systems. These discretizations avoid the pitfalls of singular balances by exploiting the asymptotic results. Importantly, the asymptotics are not used here to derive simplified equation systems, which are then solved numerically. Rather, numerical integration of the full equation sets is aimed at and the asymptotics are used only to construct discretizations that do not deteriorate as a singular limit is approached. One important ingredient of this strategy is the numerical identification of a singular limit regime given a set of discrete numerical state variables. This problem is addressed in an exemplary fashion for multiple-length single-time-scale low-Mach-number flows in one space dimension. The strategy allows a dynamic determination of an instantaneous relevant Mach number, and it can thus be used to drive the appropriate adjustment of the numerical discretizations when the singular limit regime is approached.

Key words: asymptotic analysis, fluid mechanics, singular limit regimes, asymptotics-based numerical methods

1. Introduction

Here we report on the results of a three-year research effort aimed at investigating and exploiting the role of physically motivated asymptotic analysis in the design of numerical methods for singular limit problems in fluid mechanics. Such problems naturally arise, among others, in combustion, magneto-hydrodynamics, and geophysical fluid mechanics. Typically, they are characterized by multiple space and/or time scales and by the disturbing fact that standard computational techniques fail entirely, are unacceptably expensive, or both. The challenge

here is to construct numerical methods which are robust, uniformly accurate, and efficient through different asymptotic regimes and over a wide range of relevant applications.

1.1. KEY IDEAS

In order to successfully address the goal stated above one must first accept a shift of paradigm as compared to standard applications of asymptotics: The goal of most of these applications is to derive a simplified asymptotic set of equations which can be solved analytically or with less numerical effort than the original full equation system. The target in this situation is to obtain approximate solutions to a restricted class of problems, which can then be used instead of the unavailable or expensive solutions to the full problem. This utilization of asymptotics could be labeled 'solution oriented'.

We contrast this with a 'structure oriented' exploitation of asymptotics: The ultimate goal here is the numerical solution of the full equation systems. The key questions in this context are: "What are the reasons for the failure of standard numerical schemes in singular limit regimes?" and "How are these reasons related to the asymptotic behavior of the full equation system?". To answer these questions, one must focus on the process of deriving simplified asymptotic limit equations rather than on these equations themselves. In the course of an asymptotic analysis one gains improved insight into the mathematical structure of the singular limit and obtains systematic hints at the origins of the failure of standard numerical methods. It is hoped, and has been verified in a number of examples by now, that this insight can be used to develop improved numerical techniques that avoid the pitfalls of standard schemes and allow one to treat singular and non-singular cases numerically in a unified fashion.

As an example, let us consider the case of low-Mach-number flow, which has been pursued extensively within this project. Asymptotic analysis is most comprehensive, and often considered most elegant, when carried out in terms of a suitably chosen system of coordinates and dependent variables. The probably most efficient choice of dependent variables for low-Mach-number flow are the so-called 'primitive variables', namely density, velocity and pressure. Suppose, however, that we intend to extend a standard compressible flow solver to the low- and zero- Mach-number regime. One quickly finds that modern compressible flow solvers are in conservation form for mass, momentum and energy and that the key quantities of these numerical methods are grid-cell averages of the mass, momentum, and energy densities and their respective flux densities.

The challenge then is to derive and incorporate the singular limit behavior of these fluxes in an extended numerical scheme. Obviously, the most appropriate choice of variables for a related asymptotic analysis are now the conserved quantities, regardless of the efficiency or elegance of the procedure. The results - to be described in more detail below - are somewhat surprising in that the familiar divergence constraint for the velocity field in this formulation has nothing to do with mass continuity, but is rather a consequence of energy conservation. This in turn implies that a numerical scheme in conservation form should automatically incorporate suitable elliptic constraints as part of solving the energy-conservation equation, rather than by imposing velocity-divergence conditions externally.

Technically, the following program needs to be pursued in order to realize the desired merging of numerical and asymptotic methods:

1. Identify an equation system and one of its singular limit regimes in which standard numerical methods deteriorate,

2. Reformulate existing asymptotic analyses to match the numerical framework or, if necessary, invent an appropriate new asymptotic approach such that conclusions can be drawn regarding the failure of the standard numerical method,

3. Develop modifications of the numerical technique to overcome its limitations in the singular regime on the basis of the asymptotic analysis.

The implementation of this program requires the close collaboration of scientists from a wide range of backgrounds: The first step should be driven by applications from natural sciences and engineering. It is hardly possible to cover all conceivable singular limit regimes for any given equation system, so that an educated judgement regarding the importance of any particular regime in applications should guide the selection of the target problem. The second step requires the input of both a skilled 'asymptotician' and a numerical analyst, familiar with the mathematical structure of the considered numerical methods. The third step should be pursued by the same combination of experts, this time with the major work load on the specialist in numerical methods. Ultimately, the applied scientist or engineer is required again in defining suitable tests and applications for the new method that would serve the validation of the method and be sufficiently close to applications to be meaningful in the first place.

An important additional branch of work is concerned with a mathematically precise formulation of both the asymptotic analysis and its translation into extended numerical techniques. The incorporation in a numerical method of asymptotic results, which are generally derived under specific simplifying assumptions regarding the considered physical problems, requires discrete numerical operations that properly match the asymptotic limit processes. Therefore, particular emphasis is given to the derivation of rigorous guidelines and rules which determine under which conditions it is possible to use the asymptotics and under which it is not.

The joint project summarized in this paper has brought together scientists with partly overlapping and partly complementary competences in order to cover the required range of scientific expertise. The authors acknowledge the generous support by the Deutsche Forschungsgemeinschaft under grants KL 611/6-*i*, MU 1319/2-*i* and SO 363/2-*i* ($i \in \{1, 2\}$).

1.2. Overview

There are three main sections to this paper. Section 2 summarizes asymptotic analyses for a number of fluid-mechanical problems. These analyses have been developed as guidelines in the construction of improved numerical methods. Thus, even though some of the considered regimes have been discussed in the literature before, both the presentation and the conclusions drawn here should be new. Specifically we address the following issues:

- low-Mach-number weakly compressible flows in a single-time multiple-space-scale regime,

- Magneto-hydrodynamics for small Mach and Alfvén numbers, and

- Atmospheric flows under a particular distinguished limit for the Mach and Froude numbers, namely $\mathrm{Fr} = \mathrm{M}$ as $\mathrm{M} \to 0$.

Section 3 provides a general mathematical framework for the asymptotics and prepares for its later 'translation' into numerical procedures for the multiple-scales analysis given in Section 2.1. We state in unambiguous terms what assumptions and conditions have to be

satisfied by solutions of the systems considered in order to allow an asymptotic (multiple-scales) approximation. Note that the analyses do not prove that such solutions actually do satisfy those constraints. Such proofs are formidable tasks for each application. They are hardly generalizable and beyond the scope of the present paper. Even though the discussion is motivated by the low-Mach-number limit, its results are more generally applicable. These developments are important in the context of transferring asymptotic results into numerical algorithms: Asymptotic multiple-scales procedures typically involve averaging procedures and the extraction of small-scale fluctuations, which are easily defined formally and in the limit of vanishing scale separation parameters. However, in a numerical application one is typically faced with small, *but finite* values of these parameters and the exact definitions of averaging operators and their discrete analogues become crucial. This section as well as Section 4.1 should be considered as exemplary in the sense that such a rigorous, detailed analysis should ideally be pursued for any asymptotics/ numerics merger.

Section 4 describes the announced translation of asymptotic results into improved numerical procedures. Subsection 4.1 addresses an issue that is a cornerstone of any attempt at using asymptotics in the construction of numerical methods. Asymptotic analysis may be described as a systematic procedure for the construction of particular approximate solutions to a given equation system. Such solutions are proper approximations only in the particular limit regime they are designed for. As an example consider low-Mach-number flows: the disparity between flow velocities and the speed of sound can, under suitable initial and boundary conditions, induce a time-scale separation. In this case one finds high-frequency acoustics superimposed over a much slower, quasi-incompressible flow field (see, *e.g.*, [1, 2, 3, 4, 5]). If, on the other hand, acoustic perturbations are of sufficiently long wave length, the material flow and the sound waves evolve on the same time, but on disparate spatial scales (see [6]). These physically very different regimes amount to equally different asymptotic solutions. Thus, if one is interested in exploring asymptotic results to improve numerical methods, it is necessary to employ testing procedures that determine which particular asymptotic regime is valid for the application at hand. The identification of multiple-space-scales asymptotic limit regimes by means of discrete filtering operators is the topic of Subsection 4.1.

Subsection 4.2 describes the necessary steps needed to allow the computation of weakly compressible flows using the principal machinery of standard incompressible flow solvers. The asymptotic analysis developed earlier in Section 2 shows that in weakly compressible flows the pressure plays a multiple role as a thermodynamic variable, as an acoustic mode amplitude, and as a an agent (sometimes called a 'Lagrangian multiplier') guaranteeing that, in the limit of zero Mach number, the velocity field satisfies an elliptic divergence constraint. These three roles are attributed to the leading, first, and second-order solutions in a power-series expansion of the pressure in terms of the Mach number. Only the second-order pressure survives in the limit of zero Mach number, and this is the only pressure variable known to a standard incompressible flow solver. An extension of such a method to weakly compressible flows requires the introduction of additional pressure variables, which account for global thermodynamic pressure changes and acoustic waves. Thus, this subsection describes the development of a Multiple Pressure Variable (MPV) scheme for low-Mach-number flows from the basis of a standard incompressible flow solver. Applications include examples showing baroclinic vorticity generation through long-wave acoustic pulses and a thermally driven cavity flow.

Subsection 4.3 describes the extension of conservative finite-volume methods for compressible flows to zero Mach number from [7]. The key ingredients of this extension are

(i) again the introduction of multiple pressure variables and (ii) a semi-implicit determination of numerical fluxes of mass, momentum, and energy. This procedure involves explicit estimates for the convective flux contributions based on the original upwind machinery of the underlying compressible flow solver and elliptic corrections that are derived directly from low-Mach-number asymptotics. Applications include 'falling droplets' (motion of high-density blobs of fluid under gravitational forces) and a model for thermo-acoustic devices.

Subsection 4.4 reconsiders the extension of a standard numerical method designed for the compressible Euler equations. Emphasis is now on *small, but finite* Mach numbers. In particular, the techniques described in Section 4.1 for the identification of an asymptotic regime through discrete filters is used here to automatically adjust the (small) numerical reference parameter that represents the low-Mach-number effects. A scheme is developed that allows a smooth transition from very weakly compressible to fully compressible flows with shock waves. This transition is associated with a change of the Mach-number reference parameter from very small values, where numerical flux corrections similar to those described in Section 4.3 are applied, to unity, in which case the scheme automatically reduces to the original underlying compressible flow solver. Examples include the passage of a long-wave acoustic pulse over a gas layer with high frequency, large-amplitude density variations and the nonlinear steepening of an acoustic wave into a weak shock.

The aim in Subsection 4.5 is to use results of Section 2.2 in distinguishing between terms related to pure convection and terms related to the fast wave speeds in magneto-hydrodynamics. As in the case of the Euler equations the idea behind the approach is to obtain a splitting of the system that enables one to treat the convection terms, which remain hyperbolic in the limit, and the fast-wave-speed terms, which become elliptic, with different numerical methods optimized for the respective task. In MHD there are additional hyperbolic waves besides the acoustic ones. As a consequence, there are two characteristic numbers, the Mach and Alfvén numbers, which characterize the ratio of a typical flow velocity *vs.* the respective hyperbolic wave speeds. New split systems are proposed that are used in our current work for the construction of efficient and accurate numerical methods.

In Section 5 we present conclusions and an outlook on current and future work.

2. Asymptotic analyses

2.1. Low-Mach-number asymptotics for compressible fluid flows

In this section we discuss low-Mach-number asymptotics in a sufficiently general fashion to include low-speed reacting flows. Much of the discussion will in fact be motivated by applications from combustion, although, by applying suitable simplifications, all the analytical steps carry over to non-reacting flows as well. We begin by introducing the governing equations and some general considerations regarding scaling and non-dimensionalization. This subsection will also define the non-dimensional scalar parameters that will allow us to identify the relevant asymptotic limit regimes.

2.1.1. *Governing equations*

Unscaled formulation. The full governing equations of gas-phase combustion with as little approximation as probably doable can be found in comprehensive textbooks on combustion

theory, such as [8]. Here we shall consider a simplified system only, so that the essential lines of thought can be worked out straightforwardly.

The simplified system to be discussed here consists of the conservation equations for mass, momentum and energy

$$\begin{aligned}
&(\rho)_t + \nabla \cdot (\rho \boldsymbol{v}) = 0,\\
&(\rho \boldsymbol{v})_t + \nabla \cdot (\rho \boldsymbol{v} \circ \boldsymbol{v} + 1p) + \nabla \cdot \tau = 0,\\
&(\rho e)_t + \nabla \cdot (\boldsymbol{v}[\rho e + p]) + \nabla \cdot \left(\boldsymbol{j}_T + \tau \cdot \boldsymbol{v} + \sum_{i=1}^{n_{\text{spec}}} (\Delta H)_i \boldsymbol{j}_i \right) = 0.
\end{aligned} \tag{2.1.1}$$

Here $\rho, \boldsymbol{v}, p, e$ are the mass density, fluid flow velocity, pressure, and total energy per unit mass, respectively, and $\boldsymbol{\tau}, \boldsymbol{j}_T, \boldsymbol{j}_i$ denote the molecular transport of momentum, heat, and of the mass of the ith species. These transport terms and the pressure are related to the mass, momentum, energy and species densities $\rho, \rho\boldsymbol{v}, \rho e, \rho Y_i$ through the caloric equation of state

$$\rho e = \frac{p}{\gamma - 1} + \frac{1}{2}\rho \boldsymbol{v}^2 + \sum_{i=1}^{n_{\text{spec}}} (\Delta H)_i \rho Y_i \tag{2.1.2}$$

and the transport models

$$\begin{aligned}
\boldsymbol{\tau} &= -\mu \left(\nabla \boldsymbol{v} + (\nabla \boldsymbol{v})^T \right) - \eta (\nabla \cdot \boldsymbol{v}) 1,\\
\boldsymbol{j}_T &= -\kappa \nabla T,\\
\boldsymbol{j}_i &= -D_i \nabla Y_i.
\end{aligned} \tag{2.1.3}$$

The temperature T is related to pressure and density via the thermal equation of state

$$T = \frac{p}{\rho R}. \tag{2.1.4}$$

The quantities $\gamma, R, \mu, \eta, \kappa, D_i, (\Delta H)_i$ are the isentropic exponent, the ideal gas constant, the shear and bulk viscosities, the heat conductivity, the species diffusivities and the species' formation enthalpies, respectively. All of these are assumed constant throughout this text.

The species mass fractions Y_i satisfy the inhomogeneous balance laws

$$(\rho Y_i)_t + \nabla \cdot (\rho Y_i \boldsymbol{v}) + \nabla \cdot \boldsymbol{j}_i = \rho \omega_i, \quad (i = 1 \ldots n_{\text{spec}}), \tag{2.1.5}$$

where $\omega_i = \omega_i(p, \rho, \{Y_j\}_{j=1}^{M_{spec}})$ is the net production rate of species i per unit mass of the gas mixture. When n_{spec} actually denotes the total number of chemical species in the system, then the sum of all equations in (2.1.5) leads back to the mass conservation equation in $(2.1.1)_1$ and yields a constraint for the rate expressions

$$\sum_{i=1}^{n_{\text{spec}}} \rho \omega_i = 0. \tag{2.1.6}$$

In this case, the mass conservation equation or one of the species balances are redundant.

In order to specify a single solution to these equations uniquely one must provide suitable initial and boundary conditions determining the solution behavior at some start-up time and close to the physical boundaries of the system. Since these conditions define the distinctions

between all systems that follow the same set of governing equations, we cannot exhaustively discuss them here.

Non-dimensionalization, similarity and scaling. Within the above governing equations one can identify four fundamental physical dimensions $\{\chi_i\}_{i=1}^4$: Length $\mathcal{L}$, Time $\mathcal{T}$, Mass $\mathcal{M}$ and Temperature Θ. Each physical quantity ϕ_j that appears in the governing equations has a physical dimension that is a product of these fundamental ones, so that

$$\mathrm{Dim}(\phi_j) = \prod_{i=1}^{4} (\chi_i)^{b_j^i} . \tag{2.1.7}$$

To name a few examples,

Quantity ϕ	*Physical dimension* $\mathrm{Dim}(\phi)$
ρ	$\mathcal{M}/\mathcal{L}^3$
$\boldsymbol{v}$	$\mathcal{L}/\mathcal{T}$
e	$\mathcal{L}^2/\mathcal{T}^2$
p	$\mathcal{M}/(\mathcal{L}\mathcal{T}^2)$
R	$\mathcal{L}^2/(\Theta\mathcal{T}^2)$

. (2.1.8)

Once a system of units is chosen based on which these fundamental dimensions shall be measured, each of the physical quantities and coefficients in the governing equations can be quantified by a sole number. The familiar SI-system is one example, where $(\mathcal{L}, \mathcal{T}, \mathcal{M}, \Theta)$ are measured in terms of (Meter, m; Second, s; Kilogram, kg; Kelvin, K). Knowing a quantity's physical dimension and the underlying system of units, one can always transform these non-dimensional numbers back into measurable physical values. Obviously, there is a one-to-one map between any two different systems of units, so that the exact solutions of the governing equations will not depend on which system is chosen.

As they stand, the governing equations given above do not reveal anything besides what was built into them from the start: conservation of mass, momentum and energy (2.1.1), conversion of one set of chemical species into another (2.1.5), transformations between various forms of energy (2.1.2) and some thermodynamic relations between the state quantities (2.1.4). To obtain a somewhat improved intuition about possible solutions one may study classes of solutions distinguished by some particular global mathematical characterization.

For any given solution of the equations one can identify 'characteristic values' $\left[\phi_{j,\mathrm{ref}}\right]_{j=1}^{N}$ of the total of N physical quantities in the system which roughly describe their orders of magnitude throughout the solution or at least during a certain time interval and within a selected region in space. These dimensional characteristic quantities can be combined into non-dimensional characteristic numbers

$$\Pi_k = \prod_{j=1}^{N} \left(\phi_{j,\mathrm{ref}}\right)^{a_k^j} , \tag{2.1.9}$$

with the exponents a_k^j chosen so as to guarantee that the Π_k do not have a physical dimension as will be explained shortly.

These numbers are extremely useful as they provide a comparison between various quantities that may have the same physical dimension but very different physical origin. An example is the Mach number

$$\mathrm{M} := \frac{|v_{\mathrm{ref}}|}{c_{\mathrm{ref}}}, \tag{2.1.10}$$

which compares a typical flow velocity with a characteristic speed of sound or, equivalently, the momentum flux due to convection with the momentum flux due to pressure forces (note that the speed of sound is $c^2 = \gamma p/\rho$. Here we simply take $c^2_{\mathrm{ref}} := p_{\mathrm{ref}}/\rho_{\mathrm{ref}}$, *i.e.*, $\mathrm{M}^2 = \rho_{\mathrm{ref}} u^2_{\mathrm{ref}}/p_{\mathrm{ref}}$).

For the non-dimensional Π's to be actually non-dimensional, all the physical dimensions have to cancel exactly in the product. Using (2.1.7), we may rephrase this statement as

$$\mathrm{Dim}(\Pi_k) = \prod_{j=1}^{N}\left[\prod_{i=1}^{4}(\chi_i)^{b^i_j}\right]^{a^j_k} = \prod_{i=1}^{4}\left[\prod_{j=1}^{N}(\chi_i)^{b^i_j a^j_k}\right] = \prod_{i=1}^{4}(\chi_i)\left[\prod_{i=1}^{N} b^i_j\, a^j_k\right] \equiv 1\,. \tag{2.1.11}$$

For this equation to hold, the respective powers of each of the fundamental dimensions χ_i must vanish independently, so that

$$\sum_{j=1}^{N} b^i_j\, a^j_k \equiv 0 \quad (i = 1\ldots 4, \quad k \text{ arbitrary})\,. \tag{2.1.12}$$

These are four linear constraints on the N-tuples $\mathbf{a}_k = (a^1_k, \ldots, a^N_k)$, which therefore span a total space of dimension $N - 4$. This, in turn, is equivalent to the existence of a set of $N-4$ independent characteristic numbers $\{\Pi_k\}_{k=1}^{N-4}$, and we arrive at the famous *Buckingham's π-theorem*.

The existence of these non-dimensional numbers has very deep and important consequences for the set of all possible solutions of the governing equations. To be more specific we introduce the reference quantities (ρ_{ref}, p_{ref}, v_{ref}) for density, pressure and velocity, (t_{ref}, ℓ_{ref}) for the time and space coordinates, (ω_{ref}) for chemical reaction rates and (μ_{ref}, κ_{ref}, D_{ref}, R_{ref}, $(\Delta H)_{\mathrm{ref}}$) for the various parameters in the constitutive equations. Next we define new dependent and independent variables,

$$\rho' = \frac{\rho}{\rho_{\mathrm{ref}}}, \quad p' = \frac{p}{p_{\mathrm{ref}}}, \quad \boldsymbol{v}' = \frac{\boldsymbol{v}}{v_{\mathrm{ref}}}, \quad T' = \frac{T}{p_{\mathrm{ref}}/(\rho_{\mathrm{ref}} R_{\mathrm{ref}})}, \quad e' = \frac{e}{p_{\mathrm{ref}}/\rho_{\mathrm{ref}}} \tag{2.1.13}$$

and

$$\boldsymbol{x}' = \frac{\boldsymbol{x}}{\ell_{\mathrm{ref}}}, \quad t' = \frac{t}{t_{\mathrm{ref}}}. \tag{2.1.14}$$

The governing equations are now transformed into their scaled analogues (with the prime superscript dropped for convenience of notation):

Conservation Laws:

$$\begin{aligned}
&\mathrm{Sr}(\rho)_t \quad + \nabla\cdot(\rho\boldsymbol{v}) = 0,\\
&\mathrm{Sr}(\rho\boldsymbol{v})_t \quad + \nabla\cdot\left(\rho\boldsymbol{v}\circ\boldsymbol{v} + \frac{1}{\mathrm{M}^2}\nabla p\right) + \frac{1}{\mathrm{Re}}\nabla\cdot\boldsymbol{\tau} = 0,\\
&\mathrm{Sr}(\rho e)_t \quad + \nabla\cdot(\boldsymbol{v}[\rho e + p]) + \nabla\cdot\left(\frac{1}{\mathrm{Pe}}\boldsymbol{j}_T + \frac{\mathrm{M}^2}{\mathrm{Re}}\boldsymbol{\tau}\cdot\boldsymbol{v} + \frac{\mathrm{Q}}{\mathrm{Sc}}\sum_{i=1}^{n_{\mathrm{spec}}}\delta h_i\,\boldsymbol{j}_i\right) = 0;
\end{aligned} \tag{2.1.15}$$

Species Balances:

$$\mathrm{Sr}(\rho Y_i)_t + \nabla \cdot (\rho Y_i \boldsymbol{v}) = -\frac{1}{\mathrm{Sc}} \nabla \cdot \boldsymbol{j}_i + \mathrm{Da}\rho\omega_i \qquad (i = 1 \ldots n_{\mathrm{spec}}); \tag{2.1.16}$$

Caloric Equation of State:

$$\rho e = \frac{p}{\gamma - 1} + \mathrm{M}^2 \frac{1}{2} \rho \boldsymbol{v}^2 + \mathrm{Q} \sum_{i=1}^{n_{\mathrm{spec}}} \delta h_i \, \rho Y_i; \tag{2.1.17}$$

Thermal Equation of State:

$$T = \frac{p}{\rho}; \tag{2.1.18}$$

Transport Models:

$$\begin{aligned} \boldsymbol{\tau} &= -\mu' \left(\nabla \boldsymbol{v} + (\nabla \boldsymbol{v})^T \right) - \eta' (\nabla \cdot \boldsymbol{v}) 1, \\ \boldsymbol{j}_T &= -\kappa' \nabla T, \\ \boldsymbol{j}_i &= -D_i' \nabla Y_i. \end{aligned} \tag{2.1.19}$$

Notice that in (2.1.15), (2.1.17) we have introduced the scaled reaction enthalpies

$$\delta h_i = \frac{(\Delta H)_i}{(\Delta H)_{\mathrm{ref}}}, \tag{2.1.20}$$

and that $\mu' = \mu/\mu_{\mathrm{ref}}, \kappa' = \kappa/\kappa_{\mathrm{ref}}$ etc. in (2.1.19) could all be set to unity in case of constant molecular transport coefficients.

The procedure of scaling the equations has led to a set of seven characteristic numbers:

Abbreviation	Definition	Name
Sr	$\ell_{\mathrm{ref}}/(t_{\mathrm{ref}} v_{\mathrm{ref}})$	Strouhal number
M	$v_{\mathrm{ref}}/\sqrt{p_{\mathrm{ref}}/\rho_{\mathrm{ref}}}$	Mach number
Re	$\rho_{\mathrm{ref}} v_{\mathrm{ref}} \ell_{\mathrm{ref}}/\mu_{\mathrm{ref}}$	Reynolds number
Pe	$\rho_{\mathrm{ref}} v_{\mathrm{ref}} \ell_{\mathrm{ref}}/(\kappa_{\mathrm{ref}}/R_{\mathrm{ref}})$	Peclet number
Sc	$\rho_{\mathrm{ref}} v_{\mathrm{ref}} \ell_{\mathrm{ref}}/D_{\mathrm{ref}}$	Schmidt number
Da	$\omega_{\mathrm{ref}} \ell_{\mathrm{ref}}/v_{\mathrm{ref}}$	Damköhler number
Q	$(\Delta H)_{\mathrm{ref}}/(p_{\mathrm{ref}}/\rho_{\mathrm{ref}})$	Heat Release Parameter

(2.1.21)

Notice that this number was to be expected following the earlier discussion in conjunction with (2.1.11), (2.1.12). We have introduced $N = 11$ reference quantities to characterize the magnitude of all terms and physical variables in the unscaled equations and ended up with $N - 4 = 11 - 4 = 7$ non-dimensional numbers.

Here are the key observations regarding the structure of solutions of the full governing equations to be derived from the exercise of non-dimensionalization and scaling:

1. Given:

- Initial and boundary conditions in terms of the scaled variables,
- A set of non-dimensional parameters (Sr, M, Re, Pe, Sc, Da, Q),
- The solution to the scaled governing equations (2.1.15) – (2.1.19),

Then:

- For any set of reference quantities (ρ_{ref}, p_{ref}, v_{ref}, t_{ref}, ℓ_{ref}) and fluid specific parameters (μ_{ref}, κ_{ref}, D_{ref}, R_{ref}, $(\Delta H)_{\mathrm{ref}}$, ω_{ref}) that are compatible with the given values for (Sr,M,Re,Pe,Sc,Da,Q), the fields obtained by reversing the scaling from (2.1.13), (2.1.14) represent a valid solution to the original unscaled equations!

Thus:

- Each set (Sr,M,Re,Pe,Sc,Da,Q) defines a class of equivalent solutions, which differ from each other merely by a scale transformation.

2. Close inspection of the scaled governing equations reveals that singularities arise when one or more of the non-dimensional characteristic numbers approach zero or infinity. Numerical flow simulation is a particular challenge in these regimes, as will be elucidated by a number of examples throughout this text.

Remark: The set of non-dimensional characteristic numbers chosen above is not unique. In the combustion and heat-transfer literature the Peclet and Schmidt numbers Pe and Sc are often replaced with the Prandtl and Lewis numbers $\mathrm{Pr} = \mathrm{Pe}/\mathrm{Re}$ and $\mathrm{Le} = \mathrm{Sc}/\mathrm{Pe}$, respectively.

Remark: The Strouhal number Sr is often set to unity when a set of scaled governing equations is formulated. Considering its definition in (2.1.21), we observe that this choice implies the characteristic time scale of flow field evolution to be the convection time scale $\ell_{\mathrm{ref}}/v_{\mathrm{ref}}$. Even though we will also adopt this choice below, this is neither necessary, nor is it meaningful in all cases. Taking, *e.g.*, the limit $\mathrm{Sr} \to 0$ allows one to formulate the governing equations for stationary flows.

2.1.2. *Single-length, single-time-scale asymptotics*

In most real-life applications, such as atmosphere-ocean flows, fluid flows in engineering devices, etc., velocities are small compared with the speed of sound. This fact has profound consequences for both the mathematical behavior of solutions to the governing equations from Section 2.1.1 and their numerical approximate solutions. Physically, in the limit of arbitrarily slow flow (or infinitely fast sound propagation) the elasticity of the gas with respect to bulk compression becomes negligible and sound-wave propagation becomes unnoticeable. Mathematically, as the Mach number M from (2.1.10) tends to zero, the pressure gradient contribution in the momentum equations $(2.1.15)_2$ becomes singular. In order to explore the consequences of this singularity, we consider a formal asymptotic analysis, closely following [9, 6].

A systematic derivation of the governing equations for zero-Mach-number combustion has been given by Majda and Sethian [9]. The formulation adopted below, which explicitly focuses on the conservation equations for mass, momentum and energy, has been introduced in [6] in conjunction with a multiple-length-scale, single-time-scale analysis. In [6, 7] the authors exploit the asymptotics to derive fully conservative numerical methods for low- and zero-Mach-number flows. In Section 3 below, one of the authors describes a rigorous framework for the formal asymptotics presented here with an emphasis on the physical background (see also [10]).

In recounting these earlier results we restrict ourselves to the case of an ideal gas mixture with a simple one-step reaction $F \to P$, where the fuel F is turned into the product species P. The chemical-energy conversion rate then is $\mathrm{Q}\,\rho\omega_F$, where Q quantifies the specific reaction enthalpy of the fuel species and $\rho\omega_F$ its production density. Under these conditions we need to describe the time evolution of only the fuel mass fraction Y_F, using a single transport equation of the type described in (2.1.16).

The asymptotic solution *Ansatz*

$$\begin{aligned} p &= p^{(0)}(\boldsymbol{x},t) + \mathrm{M}p^{(1)}(\boldsymbol{x},t) + \mathrm{M}^2 p^{(2)}(\boldsymbol{x},t) + o(\mathrm{M}^2),\\ \boldsymbol{v} &= \boldsymbol{v}^{(0)}(\boldsymbol{x},t) + \mathrm{M}\boldsymbol{v}^{(1)}(\boldsymbol{x},t) + o(\mathrm{M}),\\ \rho &= \rho^{(0)}(\boldsymbol{x},t) + \mathrm{M}\rho^{(1)}(\boldsymbol{x},t) + o(\mathrm{M}),\\ Y_F &= Y_F^{(0)}(\boldsymbol{x},t) + \mathrm{M}Y_F^{(1)}(\boldsymbol{x},t) + o(\mathrm{M}) \end{aligned} \tag{2.1.22}$$

is introduced into the dimensionless governing equations (2.1.15)–(2.1.16). Following standard procedures of asymptotic analysis one obtains a hierarchy of equations for the various expansion functions $p^{(i)}$, $\boldsymbol{v}^{(i)}$, $\rho^{(i)}$, $Y_F^{(i)}$ by collecting all terms multiplied by equal powers of the Mach number M and separately equating these to zero. The momentum equations to orders M^{-2} and M^{-1} become

$$\nabla p^{(0)}(\boldsymbol{x},t) = 0, \quad \nabla p^{(1)}(\boldsymbol{x},t) = 0. \tag{2.1.23}$$

One concludes that $p^{(0)}$ and $p^{(1)}$ depend on time only in this regime of length and time scales, so that

$$p^{(0)} \equiv P^{(0)}(t) \qquad \text{and} \qquad p^{(1)} \equiv P^{(1)}(t). \tag{2.1.24}$$

The continuity and energy equations at leading order are then

$$\left(\rho^{(0)}\right)_t + \nabla\cdot\left(\rho^{(0)}\boldsymbol{v}^{(0)}\right) = 0, \tag{2.1.25}$$

$$\frac{1}{\gamma-1}\frac{\mathrm{d}P^{(0)}}{\mathrm{d}t} + \nabla\cdot\left(H^{(0)}\boldsymbol{v}^{(0)}\right) = \left(\frac{1}{\mathrm{Pe}}\nabla\cdot\left(\lambda\nabla T^{(0)}\right) + \mathrm{Da}\,\mathrm{Q}(\rho\omega_F)^{(0)}\right). \tag{2.1.26}$$

where

$$H^{(0)}(t) = \frac{\gamma}{\gamma-1}\,P^{(0)}(t). \tag{2.1.27}$$

To arrive at (2.1.26), insert the expansion (2.1.22) into the energy conservation law $(2.1.15)_3$ and take into account that, according to (2.1.17), the kinetic energy is smaller than the thermal energy for $\mathrm{M} \ll 1$ by a factor of M^2. The contribution of the viscous forces to the energy budget, represented by the term $\nabla\cdot(\frac{\mathrm{M}^2}{\mathrm{Re}}\,\boldsymbol{\tau}\cdot\boldsymbol{v})$, will appear for the first time in the energy equation at order $O(\mathrm{M}^2)$.

The momentum equation at order M^0 reads

$$\left(\rho^{(0)}\boldsymbol{v}^{(0)}\right)_t + \nabla\cdot\left(\rho^{(0)}\boldsymbol{v}^{(0)}\circ\boldsymbol{v}^{(0)}\right) + \nabla p^{(2)} = -\frac{1}{\mathrm{Re}}\nabla\cdot\boldsymbol{\tau}^{(0)}. \tag{2.1.28}$$

Notice the change in structure of these equations: the pressure-evolution equation does *not* determine the pressure variable $p^{(2)}$ appearing in the momentum equation! The appropriate interpretation, corresponding directly to the theory of incompressible flows, is that the equation for $P^{(0)}$ from (2.1.26) is a divergence constraint for the leading-order energy flux, *i.e.*,

$$\nabla\cdot\left(H^{(0)}(t)\,\boldsymbol{v}^{(0)}\right) = -\left[\frac{1}{\gamma-1}\frac{\mathrm{d}P^{(0)}}{\mathrm{d}t} - \left(\frac{1}{\mathrm{Pe}}\nabla\cdot\left(\lambda\nabla T^{(0)}\right) + \mathrm{DaQ}(\rho\omega_F)^{(0)}\right)\right] \tag{2.1.29}$$

and that the second-order pressure $p^{(2)}$ is responsible for guaranteeing that constraint to be fulfilled. A useful and more familiar interpretation of this equation results from using explicitly that $H^{(0)}(t) = \gamma P^{(0)}(t)/(\gamma-1)$ is a function of time only for the present equation of state and deriving a

velocity divergence constraint

$$\nabla\cdot\boldsymbol{v}^{(0)} = -\frac{1}{\gamma P^{(0)}}\left[\frac{\mathrm{d}P^{(0)}}{\mathrm{d}t} - (\gamma-1)\left(\frac{1}{\mathrm{Pe}}\nabla\cdot\left(\lambda\nabla T^{(0)}\right) + \mathrm{DaQ}\rho\omega_F\right)\right]. \tag{2.1.30}$$

We observe that the velocity divergence is driven by chemical-energy conversion and energy-transport effects: Chemical-heat release, heat conduction and global pressure changes conspire to induce a divergence field for the velocity. As a direct consequence we derive from the mass-continuity equation (2.1.25) an equation that describes the temporal evolution of the density along particle paths

$$\frac{\mathrm{D}\rho}{\mathrm{D}t} := \frac{\partial\rho}{\partial t} + \boldsymbol{v}\cdot\nabla\rho = -\rho\nabla\cdot\boldsymbol{v}. \tag{2.1.31}$$

To summarize, the energy conversion and transport processes drive the divergence of the energy flux, which is related to the velocity divergence. The latter, in turn, leads to compression or expansion of individual mass elements and thus to density variations of individual particles. The original interpretation of (2.1.29) as an energy-flux divergence constraint proves to be useful in the construction of energy conserving finite-volume methods, (see [7, 11]).

Equations (2.1.25)–(2.1.28) form a closed system, provided the temporal evolution of the leading-order pressure $P^{(0)}$ is known and the state dependence of the reaction rate $\rho\omega_F$ is given. For combustion under atmospheric conditions $P^{(0)}$ equals the atmospheric ambient pressure and is constant in time. For combustion in a closed chamber we explore the fact that $P^{(0)}$ is homogeneous in space, integrate (2.1.30) over the total flow domain, use Gauß' theorem to replace the divergence integrals with boundary integrals and obtain a global pressure evolution equation:

$$\frac{\mathrm{d}P^{(0)}}{\mathrm{d}t} = \frac{1}{\Omega}\left[-\oint_{\partial V}\left(\gamma P^{(0)}\boldsymbol{v} - \frac{\gamma-1}{\mathrm{Pe}}\lambda\nabla T^{(0)}\right)\cdot\boldsymbol{n}\,\mathrm{d}\sigma + \mathrm{Da}\int_V(\gamma-1)\mathrm{Q}(\rho\omega_F)^{(0)}\mathrm{d}V\right], \tag{2.1.32}$$

where $\boldsymbol{n}$ is the outward-pointing unit normal at the boundary and $\Omega = \int_V \mathrm{d}V$ is the total volume of the domain of integration V. Given appropriate velocity and thermal boundary conditions, all changes of the background pressure are thus related to the overall chemical-energy conversion within the domain.

The structure of the above equations is similar to that of incompressible, non-reactive flow, in that there is convection, diffusion, and an explicit velocity-divergence constraint. Thus, appropriate extensions of incompressible flow solvers should, in principle, be able to handle zero-Mach-number reactive flows as well. See [12, 13, 14, 15] for reviews of typical developments based on this *ansatz*.

2.1.3. *Multiple-length, single-time-scale analysis*

A number of interesting engineering applications are characterized by the presence of low-frequency flow-acoustic interactions. A prominent example is the 'rumbling noise' generated in the exhaust systems of large burners. These oscillations can become quite severe when eigenfrequencies of the exhaust system are excited. The origin of these resonances are interactions of a small scale, quasi-incompressible (turbulent) inflow with low-frequency sound waves that have the same time scale as the influx, but much longer wave lengths. A formal asymptotic analysis of this situation using multiple-scales techniques has been presented in [6] and shall be reviewed briefly in this section. For simplicity of exposition we restrict ourselves here to the non-reactive Euler equations for an ideal gas with constant specific-heat capacities.

We consider acoustic oscillations having the same time scale as the underlying small scale, quasi-incompressible flow. Due to the fast propagation of sound waves, their characteristic wavelength must then be larger by a factor of order 1/M, which is the ratio of a typical sound speed over a characteristic flow velocity. A suitable asymptotic solution *ansatz* reads

$$\begin{aligned} p &= p^{(0)}(\boldsymbol{x}, \mathrm{M}\boldsymbol{x}, t) + \mathrm{M}p^{(1)}(\boldsymbol{x}, \mathrm{M}\boldsymbol{x}, t) + \mathrm{M}^2 p^{(2)}(\boldsymbol{x}, \mathrm{M}\boldsymbol{x}, t) + o(\mathrm{M}^2), \\ \boldsymbol{v} &= \boldsymbol{v}^{(0)}(\boldsymbol{x}, \mathrm{M}\boldsymbol{x}, t) + \mathrm{M}\boldsymbol{v}^{(1)}(\boldsymbol{x}, \mathrm{M}\boldsymbol{x}, t) + o(\mathrm{M}), \\ \rho &= \rho^{(0)}(\boldsymbol{x}, \mathrm{M}\boldsymbol{x}, t) + \mathrm{M}\rho^{(1)}(\boldsymbol{x}, \mathrm{M}\boldsymbol{x}, t) + o(\mathrm{M}). \end{aligned} \tag{2.1.33}$$

The *ansatz* is introduced into the dimensionless governing equations (2.1.15)–(2.1.16). In doing so, the following generalized differentiation rule must be used in order to account for the multiple-scale expansion in the spatial coordinate

$$\nabla = \nabla_x + \mathrm{M}\nabla_\xi, \qquad \boldsymbol{\xi} := \mathrm{M}\boldsymbol{x}. \tag{2.1.34}$$

Here ∇_x, ∇_ξ denote gradients including the partial derivatives w.r.t. $\boldsymbol{x}, \boldsymbol{\xi}$ at fixed $(t, \boldsymbol{\xi})$ and $(t, \boldsymbol{x})$, respectively.

Following standard procedures of multiple-scales asymptotics, we require that the sums of all terms in the expanded governing equations that multiply the same powers of the Mach number add up to zero. (Notice that this is not a trivial step, as these terms themselves depend implicitly on the Mach number through their argument $\boldsymbol{\xi} = \mathrm{M}\boldsymbol{x}$. Consult Section 3 for a detailed discussion and mathematical justification of this subtle but important point.) The result for the momentum balances at orders M^{-2} and M^{-1} is

$$\nabla_x p^{(0)}(\boldsymbol{x}, \boldsymbol{\xi}, t) = 0, \quad \nabla_x p^{(1)}(\boldsymbol{x}, \boldsymbol{\xi}, t) = -\nabla_\xi p^{(0)}(\boldsymbol{x}, \boldsymbol{\xi}, t). \tag{2.1.35}$$

One first concludes that $p^{(0)} \equiv \widetilde{P}^{(0)}(\boldsymbol{\xi}, t)$. Next one integrates the second equation in $\boldsymbol{x}$ and, following standard sub-linear growth arguments (see Section 3), concludes that

$$p^{(0)} \equiv P^{(0)}(t) \qquad \text{and} \qquad p^{(1)} \equiv P^{(1)}(\boldsymbol{\xi}, t). \tag{2.1.36}$$

The continuity and energy equations at leading order are unchanged from (2.1.25) and (2.1.26), except that the ∇-operator is to be replaced with ∇_x and that all terms in (2.1.26) due to chemistry and heat conduction may be dropped here for simplicity.

The first major change appears in the momentum equation at order M^0, which now reads

$$\left(\rho^{(0)}\boldsymbol{v}^{(0)}\right)_t + \nabla_x \cdot \left(\rho^{(0)}\boldsymbol{v}^{(0)} \circ \boldsymbol{v}^{(0)}\right) + \nabla_x p^{(2)} = -\nabla_\xi P^{(1)}. \tag{2.1.37}$$

The second-order pressure $p^{(2)}$ still is responsible for guaranteeing compliance with an $\boldsymbol{x}$-scale divergence constraint from the leading-order energy equation (2.1.26), (2.1.30), but there is now a large scale driving force due to $P^{(1)}$. We will see below that this term represents the effects on the momentum balance of long wavelength acoustics.

As before we explore next the fact that $P^{(0)}$ is homogeneous in order to derive an equation for its time dependence. First we integrate (2.1.30) over a finite sub-domain in $\boldsymbol{x}$ at fixed time and fixed $\boldsymbol{\xi}$, use Gauß' theorem to replace the divergence integrals with boundary integrals and obtain

$$\frac{\mathrm{d}P^{(0)}}{\mathrm{d}t} = -\frac{1}{\Omega}\oint_{\partial V} \gamma P^{(0)}\boldsymbol{v}\cdot\boldsymbol{n}\,\mathrm{d}\sigma, \tag{2.1.38}$$

where, as before, $\boldsymbol{n}$ is the outward-pointing unit normal at the boundary and $\Omega = \int_V \mathrm{d}V$ is the total volume of the domain of integration V. The argument now differs from the previous one for the single scale case as follows: Since the total flow domain is large enough to cover long-wavelength acoustics represented by order $O(1)$ values of $\boldsymbol{\xi}$, for every fixed $\boldsymbol{\xi}$ the relevant domain of definition in $\boldsymbol{x}$ is infinite (*i.e.*, of order $O(1/\mathrm{M})$ as $\mathrm{M}\to 0$). Thus, we may let the boundary ∂V of V tend to infinity. Requiring that the flow velocities on the boundary remain bounded or, at least, grow sub-linearly with $|\boldsymbol{x}|$ as $|\boldsymbol{x}|\to\infty$, we conclude that

$$\lim_{\Omega\to\infty}\left[\frac{1}{\Omega}\oint_{\partial V}\gamma P^{(0)}\boldsymbol{v}\cdot\boldsymbol{n}\mathrm{d}\sigma\right] = 0, \tag{2.1.39}$$

due to the vanishing surface-to-volume ratio of the domain V. (A precise formulation would have to specify in more detail how the domain boundary is spread to infinity, so that a vanishing surface-to-volume ratio is actually guaranteed. We skip these details here as they are part of the standard procedures of multiple-scales asymptotics. See, however, also Section 3.) Obviously, (2.1.39) implies that

$$P^{(0)} = P_\infty \equiv \text{constant} \tag{2.1.40}$$

on the time scales considered here. To close the obtained equations, it is necessary to derive additional equations that determine the time evolution of the first-order long-wavelength pressure contribution $P^{(1)}(\boldsymbol{\xi}, t)$. To this end we integrate the momentum equation from (2.1.37) in $\boldsymbol{x}$ over a domain V as done before for the energy equation and again use the sub-linear growth condition. Similarly, we proceed for the first-order energy equation, [6], and find

$$\begin{aligned}\left(\overline{\rho^{(0)}\boldsymbol{v}^{(0)}}\right)_t + \quad & \nabla_\xi P^{(1)} \quad = 0,\\ \left(P^{(1)}\right)_t + \quad & \nabla_\xi\cdot\left(\gamma P_\infty\overline{\boldsymbol{v}^{(0)}}\right) = 0,\end{aligned} \tag{2.1.41}$$

where $\overline{\rho^{(0)}\boldsymbol{v}^{(0)}}(\boldsymbol{\xi}, t)$, $\overline{\boldsymbol{v}^{(0)}}(\boldsymbol{\xi}, t)$ denote the small-scale averaged momentum and velocity fields, respectively.

The most striking conclusion from this analysis is that there is a mutual and non-trivial feed-back between the large and small scale flow features in the presence of small-scale, large amplitude density fluctuations, *i.e.*, in the general case of $\rho^{(0)} = \rho^{(0)}(\boldsymbol{x}, \boldsymbol{\xi}, t)$, $\nabla_x \rho^{(0)} \neq 0$. In this case, the change of momentum induced by $\nabla_\xi P^{(1)}$ in (2.1.37) will lead to large velocity changes for low density mass elements and small velocity changes for heavy ones. The result is the so-called baroclinic vorticity generation. This is a manifestation of the generation of small-scale structures by long-wave acoustic pressure gradients in the presence of small-scale density fluctuations.

We consider, on the other hand, (2.1.41) and notice that the momentum equation involves the time derivative of the small-scale average *momentum*, while the energy-flux term in the second equation contains the $\boldsymbol{\xi}$-divergence of the small-scale averaged *velocity* field. As a consequence, in presence of non-trivial small-scale fluctuations of the density $\rho^{(0)}$, these equations are not closed, as they involve the unknowns $P^{(1)}$, $\overline{\rho^{(0)}\boldsymbol{v}^{(0)}}$ and $\overline{\boldsymbol{v}^{(0)}}$. We can reveal the consequences by decomposing the velocity and density fields into mean and fluctuation according to

$$\boldsymbol{v}^{(0)} = \overline{\boldsymbol{v}^{(0)}} + \widetilde{\boldsymbol{v}^{(0)}}, \qquad \rho^{(0)} = \overline{\rho^{(0)}} + \widetilde{\rho^{(0)}} \tag{2.1.42}$$

and rewriting the averaged momentum as

$$\overline{\rho^{(0)}\boldsymbol{v}^{(0)}} = \overline{\rho^{(0)}}\,\overline{\boldsymbol{v}^{(0)}} + \overline{\widetilde{\rho^{(0)}}\widetilde{\boldsymbol{v}^{(0)}}}. \tag{2.1.43}$$

This leads to the revised formulation of the long-wave dynamics

$$\begin{aligned} \left(\overline{\boldsymbol{v}^{(0)}}\right)_t \; &+\frac{1}{\overline{\rho^{(0)}}}\nabla_\xi P^{(1)} \qquad = -\frac{1}{\overline{\rho^{(0)}}}\left(\overline{\widetilde{\rho^{(0)}}\widetilde{\boldsymbol{v}^{(0)}}}\right)_t, \\ \left(P^{(1)}\right)_t \; &+\gamma P_\infty \nabla_\xi \cdot \overline{\boldsymbol{v}^{(0)}} = \qquad 0. \end{aligned} \tag{2.1.44}$$

In the derivation we have anticipated that $(\rho^{(0)})_t = 0$, which is an immediate consequence of the small-scale averaged leading-order continuity equation (2.1.25). We observe that the left-hand side of this system represents long-wavelength linear acoustics with variable sound speed, the latter being due to the $\boldsymbol{\xi}$-dependence of $\overline{\rho^{(0)}}(\boldsymbol{\xi})$. The right-hand side of the first equation in (2.1.44) is present only if there are long-wave correlations of the small-scale fluctuations of velocity and density. In this case there is a non-negligible effect of the small scales onto the long-wave acoustics. Together with the previous observations regarding baroclinic vorticity generation this is part of a mutual interaction of small and large scales.

For a more detailed description of the mathematical framework of the multiple-scales techniques used here see Section 3. For developments of new numerical techniques on the basis of this analysis, see Sections 4.2, 4.3.

2.2. The magneto-hydrodynamic-equations (MHD-equations)

The equations of ideal MHD are

$$\frac{\partial}{\partial t}\begin{pmatrix} \rho \\ \rho\boldsymbol{v} \\ \boldsymbol{B} \\ \rho e \end{pmatrix} + \nabla \cdot \begin{pmatrix} \rho\boldsymbol{v} \\ \rho\boldsymbol{v}\circ\boldsymbol{v} + (p + \frac{1}{2}\boldsymbol{B}\cdot\boldsymbol{B})I - \boldsymbol{B}\circ\boldsymbol{B} \\ \boldsymbol{v}\circ\boldsymbol{B} - \boldsymbol{B}\circ\boldsymbol{v} \\ (\rho e + p + \frac{1}{2}\boldsymbol{B}\cdot\boldsymbol{B})\boldsymbol{v} \cdot \boldsymbol{B})\boldsymbol{B} \end{pmatrix} = 0 \tag{2.2.1}$$

with the additional constraint $\nabla \cdot \boldsymbol{B} = 0$. As in the equations governing compressible gas dynamics, ρ, $\boldsymbol{v}$, e and p are the density, the velocity, the total energy and the pressure, respectively. $\boldsymbol{B}$ is the magnetic field. If the plasma behaves like an ideal gas, pressure and total energy are related via a state equation

$$\rho e = \frac{p}{\gamma - 1} + \frac{1}{2}\rho \boldsymbol{v} \cdot \boldsymbol{v} + \frac{1}{2}\boldsymbol{B} \cdot \boldsymbol{B}.$$

Like the equations of gas dynamics, the MHD equations can be written as evolution equations for the primitive variables ρ, $\boldsymbol{v}$, $\boldsymbol{B}$, p. Let us consider, for simplicity, one-dimensional solutions in a three-dimensional space. In a Cartesian frame of reference with $\boldsymbol{x} = (x, y, z)$, $\boldsymbol{u} = (u, v, w)$, $\boldsymbol{B} = (B_1, B_2, B_3)$ and $\partial/\partial y = \partial/\partial z = 0$ the primitive equations read

$$\begin{aligned}
&\rho_t + u\rho_x + \rho u_x && = 0\,,\\
&u_t + uu_x + \frac{1}{\mathrm{M}^2}\frac{p_x}{\rho} + \frac{1}{2\mathrm{Av}^2\rho}(\boldsymbol{B}\cdot\boldsymbol{B})_x && = 0\,,\\
&v_t + uv_x - \frac{B_1}{\mathrm{Av}^2\rho}B_{2x} && = 0\,,\\
&w_t + uw_x - \frac{B_1}{\mathrm{Av}^2\rho}B_{3x} && = 0\,,\\
&B_{2t} + uB_{2x} + B_2u_x - B_1v_x && = 0\,,\\
&B_{3t} + uB_{3x} + B_3u_x - B_1w_x && = 0\,,\\
&p_t + up_x + \gamma p u_x && = 0\,.
\end{aligned} \tag{2.2.2}$$

Here we have introduced the scaling described in Section 2.1 and an additional reference value B_{ref} for the magnetic field. Since there is an additional equation for the magnetic field, a new characteristic number appears. This is the Alfvén number Av, the ratio between flow velocity and speed of the magneto-sonic waves, $c_{A,\mathrm{ref}}$:

$$\mathrm{Av} := \frac{|v_{\mathrm{ref}}|}{c_{A,\mathrm{ref}}} = \frac{|v_{\mathrm{ref}}|}{\sqrt{\frac{B_{\mathrm{ref}}^2}{\rho_{\mathrm{ref}}}}}.$$

2.2.1. *The case of small Mach number*

For the case of small Mach number but finite Av, the asymptotic expansion described in Section 2.1 can be extended to the MHD equations. The asymptotic multi-scale *ansatz* (2.1.33), completed by

$$\boldsymbol{B}(x, t; \mathrm{M}) = \boldsymbol{B}^{(0)}(x, \mathrm{M}x, t) + \mathrm{M}\boldsymbol{B}^{(1)}(x, \mathrm{M}x, t) + o(\mathrm{M}), \tag{2.2.3}$$

leads to the following zero-Mach-number limit equations:

$$
\begin{aligned}
&\rho_t + \rho u_x + \rho_x u && = 0\,,\\
&u_t + uu_x + \frac{1}{\rho}p_x^{(2)} + \frac{1}{2\mathrm{Av}^2\rho}(\boldsymbol{B}\cdot\boldsymbol{B})_x && = -\frac{1}{\rho}p_\xi^{(1)},\\
&v_t + uv_x - \frac{1}{\mathrm{Av}^2\rho}B_1B_{2x} && = 0\,,\\
&w_t + uw_x - \frac{1}{\mathrm{Av}^2\rho}B_1B_{3x} && = 0\,,\\
&B_{2t} + B_2u_x - B_1v_x + uB_{2x} && = 0\,,\\
&B_{3t} + B_3u_x - B_1w_x + uB_{3x} && = 0\,,\\
&p_t^{(0)} + \gamma p^{(0)}u_x && = 0\,.
\end{aligned}
\tag{2.2.4}
$$

As in Section 2.1, it turns out that the first three terms of the pressure expansion

$$p = p^{(0)} + \mathrm{M}p^{(1)} + \mathrm{M}^2p^{(2)} + o(\mathrm{M}^2) \tag{2.2.5}$$

carry different physical meanings; $p^{(0)}$ and $p^{(1)}$ represent the thermodynamic pressure and the amplitude of acoustic perturbations, respectively. Their evolution equations are analogous to (2.1.36) and (2.1.38)–(2.1.41). The second-order pressure $p^{(2)}$ is implicitly defined by (2.2.4). The main difference with respect to the case of pure gas dynamics is that, here, magnetic field and velocity field are coupled. Therefore, the magnetic field appears in the elliptic equation for $p^{(2)}$. The one-dimensional analysis can be extended to the multidimensional case in a straightforward way.

The main result of the analysis is that the presence of the magnetic field does not break the structure of the zero-Mach-number limit equations. Therefore, numerical methods for low-Mach-number finite-Alfvén-number inviscid MHD can be developed on the same basis as numerical methods for the low- Mach-numbers Euler equations. One such method is discussed in Section 4.5.

2.2.2. *The case of small Alfvén number*

We consider now the distinguished limit in which the magneto-sonic waves are much faster than the flow, $\mathrm{Av} \to 0$, but the Mach number is finite. The asymptotic *ansatz* now reads

$$U(x,t;\mathrm{Av}) = U^{(0)}(x,\mathrm{Av}x,t) + \mathrm{Av}U^{(1)}(x,\mathrm{Av}x,t) + \mathrm{Av}^2U^{(2)}(x,\mathrm{Av}x,t) + o(\mathrm{Av}^2) \tag{2.2.6}$$

with $U = \{\rho, \boldsymbol{v}, p, \boldsymbol{B}\}$. Introducing this *ansatz* into the one-dimensional MHD equations (2.2.2) and collecting the terms which multiply the same powers of the Alfvén number leads to the basic equations of MHD for zero Alfvén number and to a set of perturbation equations. Using the same techniques described in the analysis of the hydrodynamic equations, small-scales averaging and standard sub-linear growth constraints, one obtains the following results:

Due to the singular terms in the Alfvén number appearing in the MHD equations, the leading-order magnetic field becomes spatially homogeneous. The first-order magnetic field is homogeneous in x but supports non-trivial structures on the large scale ξ:

$$B_2^{(0)} = B_2^{(0)}(t), \qquad B_2^{(1)} = B_2^{(1)}(\xi,t)\,, \tag{2.2.7}$$

$$B_3^{(0)} = B_3^{(0)}(t), \qquad B_3^{(1)} = B_3^{(1)}(\xi, t) \; . \tag{2.2.8}$$

The MHD equations for zero-Alfvén-number limit read

$$\begin{aligned}
&\rho_t + \rho u_x + \rho_x u && = 0 \; , \\
&u_t + u u_x + \frac{1}{\mathrm{M}^2}\frac{1}{\rho} p_x + \frac{1}{\rho}(B_2^{(0)} B_{2,x}^{(2)} + B_3^{(0)} B_{3,x}^{(2)}) && = -\frac{1}{\rho}(B_2^{(0)} B_{2,\xi}^{(1)} - B_3^{(0)} B_{3,\xi}^{(1)}) \; , \\
&v_t + u v_x - \frac{1}{\rho} B_1 B_{2,x}^{(2)} && = \frac{1}{\rho} B_1 B_{2,\xi}^{(1)} \; , \\
&w_t + u w_x - \frac{1}{\rho} B_1 B_{3,x}^{(2)} && = \frac{1}{\rho} B_1 B_{3,\xi}^{(1)} \; , \\
&p_t + \gamma p u_x + p_x u && = 0 \; .
\end{aligned}$$

and one finds the following additional coupling constraints between velocity and magnetic field

$$\begin{aligned}
&B_{2,t}^{(0)} + B_2^{(0)} u_x - B_1 v_x \; &= 0 \; , \\
&B_{3,t}^{(0)} + B_3^{(0)} u_x - B_1 w_x \; &= 0 \; ,
\end{aligned} \tag{2.2.9}$$

We remark that, according to (2.2.7) and (2.2.8), $B_2^{(i)}, B_3^{(i)}, i = 0, 1$, are constant in x. Hence (2.2.9) may be interpreted as constraints for the velocity components. The structure here is much more complicated than in the zero-Mach-number limit. It becomes even more complicated in the multidimensional case. Evolution equations for long-wavelength magneto-acoustics are obtained by averaging the velocity and magnetic-field perturbation equations. A further interesting regime would be described by the limit $\mathrm{M} = c\,\mathrm{Av}$ with $c = O(1)$ as $\mathrm{M} \to 0$. As we will see in the next section, such a distinguished limit leads to new interactions between the fast waves that are not captured by any sequential limit or by any two-parameter expansion!

2.3. Slow atmospheric motion

Understanding and computing motions in the atmosphere is particularly challenging because of the multitude of physical processes and of the different space and time scales involved. In spite of its physical complexity and variety, however, atmospheric motion is confined to a very special regime. The Mach number M varies from zero at rest to about 0·3 in fast jet streams, hurricanes and tornadoes.

As seen in Section 2.1, in the $\mathrm{M} \to 0$ limit the governing equations for compressible (air) flow become singular. Due to this singularity pressure differences as small as M^2 can generate $O(1)$ accelerations of the horizontal winds, while the pressure forces are in an almost exact balance (see Equation (2.1.28)). In fact, the problem of extracting the 'correct' net effect that modifies an almost perfect balance is a very common one in weather forecasting, see, *e.g.*, [16 p. 187], and both theoretical and numerical investigations of atmospheric motion make use of related approximate *models*. These models achieve a simplification of the governing equations by assuming some kind of balance, *e.g.*, *hydrostatic*, *geostrophic*, *Boussinesq*, *anelastic*, *pseudo-incompressible*. For comprehensive accounts of the matter the reader may want to consult the classical textbooks by Gill [17] and Pedlosky [18], or the monographs by

Zeytounian [19, 20]. Note that Zeytounian uses techniques of asymptotic analysis that are very close to those employed in the present work, albeit with the aim of *asymptotic modelling* (deriving simplified asymptotic equations), instead of guiding the construction of new numerical techniques.

In spite of the outstanding role of approximate models, modern computational approaches in numerical weather forecasting turn back to the full governing equations, see [21]. The reasons are:

1. The full equations are believed to allow a better description of real motions than approximate models do.

2. In contrast to approximate models, the full equations are valid on a wide range of scales. Therefore, numerical methods based on the full equations can be naturally coupled with local-mesh-refinement techniques for, *e.g.*, regional weather forecasting.

3. Both numerical weather forecasting and climate research need fast algorithms. If one knows how to avoid time-step restrictions due to fast modes, the computational cost of integrating the full equations can be significantly lower than the cost of solving the equation of, *e.g.*, an anelastic model.

When attempting to compute numerical solutions of the full compressible equations at different resolutions one has to face two major problems. 1) Standard methods exhibit a breakdown of both accuracy and efficiency in the low-Mach-number regime, see [22], [23], [6], [24], [25]. 2) As the grid size changes, one has to adjust the *parameterizations* of the subcell processes. Such parameterizations have been designed (and are considered to be valid) for a given scaling or a well defined grid size. Tautologically, there is very little knowledge on how parameterizations depend on the grid size. It has been observed in climate research and weather forecasting that, for a given model, a simple grid refinement by a factor of two may have drastic impacts on the computed solution and may thus require a complete new adjustment of parameters in the sub-grid scale models.

We propose multiple-scale low-Mach-number low-Froude-number asymptotic analysis as a general framework for understanding the motion in the atmosphere on space scales ranging from a few meters to thousands of kilometers. The theory, detailed in [26], provides a consistent picture of slow atmospheric flows and turns out to be the natural framework in which approximations, traditionally obtained on the basis of simplifying assumptions or *ad hoc* scaling arguments, can be derived. The analysis yields interesting implications for discrete methods aiming at the numerical computation of atmospheric motions as, *e.g.*, in numerical weather prediction or climate modeling. There are two kinds of implications. On one hand one finds side constraints on parameterizations of unresolved physical processes such as turbulent heat transport or velocity boundary conditions. On the other hand, the asymptotic analysis provides guidelines for consistently 'filtering' the equations and suggests that 'singular dynamic-range problems', such as the multiple-pressure problem for low-Mach-number flows from Section 2.1, can be overcome by the introduction of suitable multiple variables that mimic the asymptotic decomposition of the field quantities.

The analyses presented below are designed to support the construction of numerical integration techniques. Thus, we use asymptotics in order to reveal singular behaviour *on the numerically resolved length and time scales*. Importantly, these scales do not necessarily

match the length and time scales that a meteorologist or oceanographer would ultimately be interested in. For example, in the near future one may expect horizontal numerical grid resolutions of 5 km or less and numerical time steps on the order of minutes or less. In contrast, the synoptic scales of weather dynamics in the mid-latitudes involve hundreds to thousands of kilometres and time scales up to several hours or days. Our primary interest here is in the much shorter, numerically resolved scales, and this is why some of our results may appear not to be in line with classical results of theoretical meteorology [17, 18] or asymptotic modelling [19, 20] at a first glance. We emphasize, however, that those results can be recovered by systematically employing multiple-scales asymptotics. With the present multiple-*space*-scale analyses we do already recover some of the classical results, while we hope to provide a completely consistent picture based on both multiple-*time* and multiple-*space* scale analyses elsewhere in the near future.

2.3.1. *Scaling, equations of motion*

An atmosphere is said to be in hydrostatic balance when the vertical pressure gradient balances the force of gravity: $\partial p/\partial z = -\rho g$. Let p_{ref} be a reference pressure (*e.g.* some mean sea-level pressure). The scale height $h_{\mathrm{scale}} := p_{\mathrm{ref}}/(\rho_{\mathrm{ref}} g)$ represents the height over which pressure changes of magnitude p_{ref} would occur in a constant density atmosphere in hydrostatic balance. It is a rough measure of the thickness of the atmosphere: $h_{\mathrm{scale}} = O(10)$ km. We consider h_{scale} as our basic scale and use two-scale asymptotics to resolve much smaller horizontal 'micro scales' in one *ansatz* and to cover the much larger synoptic scales in another. The first *ansatz* is designed to assess deep convective motions that may occur in cumulus clouds, while the second analyses short-time dynamics on the large scales of weather patterns.

If p_{ref}, ρ_{ref}, v_{ref} and $l_{\mathrm{ref}} := h_{\mathrm{scale}}$ are taken as reference variables, the conservation laws for mass, momentum and energy in a dry rotating atmosphere ([16], [17], [27]) read

$$\begin{aligned}
&\rho_t + \nabla_\parallel \cdot (\rho \boldsymbol{u}) + (\rho w)_z && = 0,\\
&(\rho \boldsymbol{u})_t + \nabla_\parallel \cdot (\rho \boldsymbol{u} \circ \boldsymbol{u}) + (\rho \boldsymbol{u} w)_z + \frac{1}{\mathrm{M}^2}\nabla_\parallel p + \frac{1}{\mathrm{Ro}}\rho\left(\boldsymbol{u}^\perp \mathcal{S} + \boldsymbol{i} w \mathcal{C}\right) && = \boldsymbol{D}_{\rho \boldsymbol{u}},\\
&(\rho w)_t + \nabla_\parallel \cdot (\rho \boldsymbol{u} w) + (\rho w^2)_z + \frac{1}{\mathrm{M}^2} p_z + \frac{1}{\mathrm{Fr}^2}\rho g - \frac{1}{\mathrm{Ro}}\rho u \mathcal{C} && = D_{\rho w},\\
&(\rho e)_t + \nabla_\parallel \cdot ((\rho e + p)\boldsymbol{u}) + ((\rho e + p) w)_z && = D_{\rho e},
\end{aligned} \tag{2.3.1}$$

with the equation of state

$$p = (\gamma - 1)\left(\rho e - \frac{1}{2}\mathrm{M}^2 \rho \boldsymbol{v}\cdot\boldsymbol{v} - \frac{\mathrm{M}^2}{\mathrm{Fr}^2}\rho g z\right). \tag{2.3.2}$$

We are considering a simplified geometrical setup in which the acceleration of gravity acts in the vertical direction $\boldsymbol{k}$ of a Cartesian frame of reference of coordinates x, y, z, unit vectors $\boldsymbol{i}$, $\boldsymbol{j}$ and $\boldsymbol{k}$ and velocity components u, v and w; $\boldsymbol{u} := \boldsymbol{i}u + \boldsymbol{j}v$ is called the horizontal wind and $\boldsymbol{u}^\perp := -\boldsymbol{i}v + \boldsymbol{j}u$. This frame of reference rotates with constant angular velocity Ω around the axis defined by the unit vector $\boldsymbol{\Omega} := \boldsymbol{j}\mathcal{C} + \boldsymbol{k}\mathcal{S}$, where $\mathcal{C}$ and $\mathcal{S}$ are the sinus and the cosine of the latitude. They depend on the space coordinate but not on time. The operator $\nabla_\parallel$ indicates differentiation in the horizontal directions and $f_z := \partial f/\partial z$. $\mathrm{M} := v_{\mathrm{ref}}/\sqrt{p_{\mathrm{ref}}/\rho_{\mathrm{ref}}}$, $\mathrm{Fr} := v_{\mathrm{ref}}/\sqrt{g_{\mathrm{ref}} l_{\mathrm{ref}}}$ and $\mathrm{Ro} := v_{\mathrm{ref}}/(2\Omega l_{\mathrm{ref}})$ are the Mach number, the Froude number and the Rossby number, respectively. The terms $\boldsymbol{D}_{\rho \boldsymbol{u}}$, $D_{\rho w}$ on the right-hand side represent the

effects of microscopical (molecular and/or turbulent) transport of momentum. $D_{\rho e}$ accounts for both microscopical transport of energy and for diabatic heating (latent heat and radiation). These processes are usually parameterized by means of empirical relationships or models. The above system of conservation laws implies the following evolution equation for the entropy $s = p/\rho^\gamma$:

$$s_t + \boldsymbol{u} \cdot \nabla_\parallel s + w s_z = \frac{\gamma - 1}{\rho^\gamma} \left(D_{\rho e} - \mathrm{M}^2 (\boldsymbol{u} \cdot \boldsymbol{D}_{\rho \boldsymbol{u}} + w D_{\rho w}) \right). \tag{2.3.3}$$

2.3.2. *Asymptotic ansatz*

Let U be a shortcut for a solution component or a function of a solution of the governing equations (2.3.1), such as the pressure p, density ρ or the velocity field $\boldsymbol{v} = \boldsymbol{u} + w\boldsymbol{k}$. In general, U depends on the horizontal coordinate $\boldsymbol{x} := \boldsymbol{i}x + \boldsymbol{j}y$, the vertical coordinate z, the time t, the singular perturbation parameter M and on other dimensionless parameters like the Rossby and Reynolds numbers, Ro, Re, etc. We focus the attention on the behavior of U as $\mathrm{M} \to 0$, noticing that our choice of a reference length implies

$$\mathrm{Fr} \equiv \mathrm{M} \qquad \text{for} \qquad l_{\mathrm{ref}} := h_{\mathrm{scale}}. \tag{2.3.4}$$

Assuming that all dimensionless parameters other than the Froude and Mach numbers are fixed as $\mathrm{M} \to 0$, we write $U = U(\boldsymbol{x}, z, t; \mathrm{M})$ and consider an asymptotic expansion of the solution in terms of the Mach/Froude number:

$$U(\boldsymbol{x}, z, t; \mathrm{M}) := \sum_{i=0} \mathrm{M}^i U^{(i)}(\boldsymbol{\eta}, \boldsymbol{x}, \boldsymbol{\xi}, z, \tau, t). \tag{2.3.5}$$

Here

$$\boldsymbol{\eta} = \frac{1}{\mathrm{M}} \boldsymbol{x}, \qquad \tau = \frac{1}{\mathrm{M}} t \tag{2.3.6}$$

are new small-scale horizontal and time coordinates, while

$$\boldsymbol{\xi} = \mathrm{M}\boldsymbol{x} \tag{2.3.7}$$

represents a new large-scale horizontal coordinate in analogy with the multiple-scales *ansatz* pursued in Section 2.1.3.

In particular, we will consider $U^{(i)} = U^{(i)}(\boldsymbol{\eta}, z, \tau)$ for the analysis of deep convection on very small horizontal scales and $U^{(i)} = U^{(i)}(\boldsymbol{x}, z, t)$, $U^{(i)} = U^{(i)}(\boldsymbol{x}, \boldsymbol{\xi}, z, t)$ for the analysis on the meso and synoptic scales. In this paper we will not consider any multi-scale *ansatz* in the vertical direction.

2.3.3. *Results*

Leading-order pressure and density. Leading-order pressure and density are found to be in hydrostatic balance both at micro scale and at meso and synoptic scales:

$$p^{(0)} = p^{(0)}(z), \qquad \rho^{(0)} = \rho^{(0)}(z). \tag{2.3.8}$$

This result is not surprising. Indeed, it is common practice in numerical methods for atmospheric flows to solve for $p - p^{(0)}$, $\rho - \rho^{(0)}$ where the hydrostatic basic state $p^{(0)}, \rho^{(0)}$ is more or less arbitrarily assigned. (see [21, pp. 39–41].)

Meso and synoptic scales: Vertical velocity constraint. A less trivial result is obtained by averaging the continuity equation and the entropy equation (2.3.3) on the meso scales and taking into account (2.3.8). One gets

$$\begin{aligned} \partial_z(\rho^{(0)}\overline{w^{(0)}}^{\boldsymbol{x}}) &= \rho^{(0)}\frac{1}{|\mathcal{D}_{\boldsymbol{x}}|}\int\limits_{\partial\mathcal{D}_{\boldsymbol{x}}} \boldsymbol{u}^{(0)}\cdot\boldsymbol{n}\,\mathrm{d}L, \\ \overline{w^{(0)}}^{\boldsymbol{x}}\partial_z s^{(0)} &= \rho^{(0)-\gamma}(\gamma-1)\overline{D_{\rho e}^{(0)}}^{\boldsymbol{x}}. \end{aligned} \tag{2.3.9}$$

In the above system $\overline{w^{(0)}}^{\boldsymbol{x}}$ represents the average of $w^{(0)}$ on the $\boldsymbol{x}$-scales. The system shows that, if $\partial_z s^{(0)} \neq 0$, the leading-order mass flux through $\partial\mathcal{D}_{\boldsymbol{x}}$ and the vertical rate of change of the leading-order average heating $\overline{D_{\rho e}^{(0)}}^{\boldsymbol{x}}$ are coupled by a simple relationship. In the special case of zero mass flux the first equation requires $\partial_z(\rho^{(0)}\overline{w^{(0)}}^{\boldsymbol{x}})$ to be zero. Since $\rho^{(0)} \to 0$ for $z \to \infty$ and $\overline{w}^{\boldsymbol{x}}$ is bounded, $\overline{w^{(0)}}^{\boldsymbol{x}}$ must be zero. In this case the source term of the energy equation, $D_{\rho e}^{(0)}$ must have a zero small-scale average. Thus we have found a constraint that parameterizations of turbulent and radiative heating must fulfill in the limit of vanishing Mach and Froude numbers.

For a stable stratification, $\partial_z s^{(0)} \neq 0$, the entropy evolution equation yields the leading-order (non-averaged) vertical velocity $w^{(0)}$ as a function of the heating term $D_{\rho e}^{(0)}$:

$$w^{(0)} = \frac{\rho^{(0)-\gamma}(\gamma-1)D_{\rho e}^{(0)}}{\partial_z s^{(0)}}. \tag{2.3.10}$$

Note that this is *not* a form or consequence of the continuity equation. In fact, insertion of (2.3.10) in the continuity equation yields a sequence of two-dimensional Poisson problems for the second-order pressure $p^{(2)}$, one for each constant z-level. This pressure, in turn, is needed to determine the leading-order horizontal wind.

Thus, the leading-order analysis yields the following picture of slow atmospheric motion on meso and synoptic scales: Pressure and density are in hydrostatic balance to leading order; the vertical wind has zero small-scale average or has an average that is coupled to the boundary conditions for the horizontal wind; for stable stratifications the vertical wind is a function of the source term of the energy equation and of the stability parameter represented by $\partial s^{(0)}/\partial z$. This functional dependence defines a divergence constraint for the horizontal wind and allows its computation by layer-wise numerical integration of a set of quasi-two-dimensional Navier-Stokes equations. This picture and, in particular, Equation (2.3.10) are consistent with the results obtained on the micro scales where the interest is focused on deep convection. On such scales the dynamics of vertical velocity and density perturbation are described by the following system of partial differential equations (see [26]):

$$\begin{aligned} \frac{c^{(0)^2}}{\rho^{(0)^\gamma}}\frac{\mathrm{D}\widetilde{\rho^{(1)}}^{\eta}}{\mathrm{D}\tau} - \partial_z s^{(0)}\widetilde{w^{(0)}}^{\eta} &= -\frac{\gamma-1}{\rho^{(0)^\gamma}}\widetilde{D_{\rho e}^{(0)}}^{\eta}, \\ \frac{\mathrm{D}\widetilde{w^{(0)}}^{\eta}}{\mathrm{D}\tau} + \frac{\widetilde{\rho^{(1)}}^{\eta}}{\rho^{(0)}}g &= \frac{1}{\rho^{(0)}}\widetilde{D_{\rho w}^{(-1)}}^{\eta}. \end{aligned} \tag{2.3.11}$$

In this system $\widetilde{w^{(0)}}^{\eta}$ represents the difference between the leading-order vertical velocity and its small-scale average (*i.e.* the average over scales of order $O(\mathrm{M}h_{\mathrm{scale}})$). These equations describe the well known oscillations of density perturbations in a stably stratified atmosphere that are associated with the Brunt-Väisälä frequency and the additional driving of vertical motions due to net heat sources. Notice that stationary solutions of this system on the (very short) τ-time scale, with $\mathrm{D}/\mathrm{D}\tau \equiv 0$, reproduce the diagnostic vertical velocity equation from (2.3.10) which was obtained in the single space, single time scale regime.

Anelastic and Boussinesq approximation. A popular approximation to the full continuity equation $(2.3.1)_1$ is the *anelastic* approximation ([28], [29]): $\nabla \cdot (\overline{\rho}\boldsymbol{v}) = 0$. Citing [27], we observe that $\overline{\rho}$ is 'a steady reference-state density that varies only along the coordinate axis parallel to the gravitational restoring force' *i.e.* $\overline{\rho}$ is equal to $\rho^{(0)}$. In this case

$$\nabla \cdot (\overline{\rho}\boldsymbol{v}) = \nabla \cdot (\rho^{(0)}\boldsymbol{v}) = \nabla_x \cdot (\rho^{(0)}\boldsymbol{u}^{(0)}) + \partial_z(\rho^{(0)}w^{(0)}) + O(\mathrm{M}) = O(\mathrm{M}). \tag{2.3.12}$$

The last equality follows from (2.3.8) and shows that the anelastic equation approximates the full continuity equation up to terms of order $O(\mathrm{M})$ as $\mathrm{M} \to 0$. Notice also that the Boussinesq approximation, $\nabla \cdot \boldsymbol{v} = 0$, will generally introduce unacceptable leading-order errors, unless the vertical velocity w is very small everywhere.

Meso and synoptic scales: first order perturbation. Let $\zeta^{(0)}$ be the synoptic density-weighted vorticity of the average leading-order horizontal velocity

$$\zeta^{(0)} := \rho^{(0)}\boldsymbol{k} \cdot \nabla_{\boldsymbol{\xi}} \overline{\boldsymbol{u}^{(0)}}^{\boldsymbol{x}} = -\rho^{(0)} \nabla_{\boldsymbol{\xi}} \cdot \overline{\boldsymbol{u}^{(0)\perp}}^{\boldsymbol{x}}. \tag{2.3.13}$$

Remember that $\boldsymbol{\xi} := \mathrm{M}\boldsymbol{x}$. As pointed out in the previous paragraphs, pressure and density are in hydrostatic balance as $\mathrm{M} \to 0$. They only depend on the vertical coordinate z. Thus, pressure tendencies $\partial p/\partial t$ are small of order $O(\mathrm{M})$. These tendencies do not vary on the meso scales: they are functions of t, $\boldsymbol{\xi}$ and of the vertical coordinate but *not* of $\boldsymbol{x}$. They are coupled with $\zeta^{(0)}$ through the following system

$$\begin{aligned} \partial_{tt} p^{(1)} - c^{(0)^2} \Delta_{\boldsymbol{\xi}} p^{(1)} &= -c^{(0)^2} \overline{f}^{\boldsymbol{x}} \zeta^{(0)} + P, \\ \partial_t \zeta^{(0)} &= \frac{\overline{f}^{\boldsymbol{x}}}{c^{(0)^2}} \partial_t p^{(1)} + Q. \end{aligned} \tag{2.3.14}$$

This system describes the interaction between long-wave acoustics and large-scale vorticity. The terms P and Q on the right-hand side depend on the $\boldsymbol{x}$-average of the first-order perturbation vertical velocity $\overline{w^{(1)}}^{\boldsymbol{x}}$, on variations of the Coriolis parameters $\mathcal{f}$ and $\mathcal{C}$ on the large scales, on correlations between fluctuations of the leading-order velocity, on large-scale turbulent stresses and on the heating. In the special case $P = Q = 0$ the system (2.3.14) supports traveling waves of the form

$$(p^{(1)}, \zeta^{(0)}) = (p_0^{(1)}, \zeta_0^{(0)}) e^{\mathrm{i}(kx+ly-\omega t)} \tag{2.3.15}$$

provided that $\kappa^2 := k^2 + l^2$ satisfies the dispersion relation

$$\omega^2 = c^{(0)^2}\kappa^2 + \overline{f}^{\boldsymbol{x}^2}. \tag{2.3.16}$$

This is the dispersion relation for perturbations of the *shallow water* approximation linearized about a *geostrophic* basic state, see [27] page 15.

The closure of system (2.3.14) for the first-order perturbation pressure $p^{(1)}$ and for the large-scale vorticity $\zeta^{(0)}$ requires an equation for the vertical velocity $\overline{w^{(1)}}^{\boldsymbol{x}}$. For a stable stratification, $\partial_z s^{(0)} \neq 0$, one obtains:

$$
\begin{aligned}
\partial_{tt} p^{(1)} - c^{(0)^2} \Delta_{\boldsymbol{\xi}} p^{(1)} = \; & -c^{(0)^2} \overline{f}^{\boldsymbol{x}} \zeta^{(0)} + \rho^{(0)} \partial_t \left(g \overline{w^{(1)}}^{\boldsymbol{x}} - c^{(0)^2} \partial_z \overline{w^{(1)}}^{\boldsymbol{x}} \right) \\
& + \frac{1}{\mathrm{Ro}} c^{(0)^2} \rho^{(0)} \nabla_{\boldsymbol{\xi}} \cdot \left(\overline{\widetilde{\boldsymbol{u}^{(0)\perp}}^{\boldsymbol{x}} \widetilde{\mathcal{J}}}^{\boldsymbol{x}} + \boldsymbol{i} \overline{\widetilde{w^{(0)}}^{\boldsymbol{x}} \widetilde{\mathcal{C}}}^{\boldsymbol{x}} \right) \\
& + c^{(0)^2} \partial_z (\rho^{(0)} \overline{\widetilde{\boldsymbol{u}^{(0)}}^{\boldsymbol{x}} \widetilde{w^{(0)}}^{\boldsymbol{x}}}^{\boldsymbol{x}}) \\
& + (\gamma - 1) \partial_t \overline{D_{\rho e}^{(1)}}^{\boldsymbol{x}} - c^{(0)^2} \nabla_{\boldsymbol{\xi}} \cdot \overline{\boldsymbol{D}_{\rho \boldsymbol{u}}^{(0)}}^{\boldsymbol{x}}, \\
\partial_t \zeta^{(0)} = \; & \frac{\overline{f}^{\boldsymbol{x}}}{c^{(0)^2}} \partial_t p^{(1)} + \overline{f}^{\boldsymbol{x}} \partial_z (\rho^{(0)} \overline{w^{(1)}}^{\boldsymbol{x}}) \\
& - \frac{1}{\mathrm{Ro}} \rho^{(0)} \boldsymbol{k} \cdot \nabla_{\boldsymbol{\xi}} \times \left(\overline{\widetilde{\boldsymbol{u}^{(0)\perp}}^{\boldsymbol{x}} \widetilde{\mathcal{J}}}^{\boldsymbol{x}} + \boldsymbol{i} \overline{\widetilde{w^{(0)}}^{\boldsymbol{x}} \widetilde{\mathcal{C}}}^{\boldsymbol{x}} \right) \\
& - \boldsymbol{k} \cdot \nabla_{\boldsymbol{\xi}} \times \partial_z \left(\rho^{(0)} \overline{\widetilde{\boldsymbol{u}^{(0)}}^{\boldsymbol{x}} \widetilde{w^{(0)}}^{\boldsymbol{x}}}^{\boldsymbol{x}} \right) \\
& - \frac{\overline{f}^{\boldsymbol{x}}}{c^{(0)^2}} (\gamma - 1) \overline{D_{\rho e}^{(1)}}^{\boldsymbol{x}} + \boldsymbol{k} \cdot \nabla_{\boldsymbol{\xi}} \times \overline{\boldsymbol{D}_{\rho \boldsymbol{u}}^{(0)}}^{\boldsymbol{x}}, \\
N^{(0)^2} c^{(0)^2} \overline{w^{(1)}}^{\boldsymbol{x}} = \; & -\frac{1}{\rho^{(0)}} \partial_t \left(g p^{(1)} + c^{(0)^2} \partial_z p^{(1)} \right) \\
& + \frac{g}{\rho^{(0)}} (\gamma - 1) \overline{D_{\rho e}^{(1)}}^{\boldsymbol{x}}.
\end{aligned}
\tag{2.3.17}
$$

where $N^{(0)}$ is the buoyancy frequency

$$
N^{(0)^2} := -g \left(\frac{\partial_z \rho^{(0)}}{\rho^{(0)}} + g \frac{\rho^{(0)}}{\gamma p^{(0)}} \right). \tag{2.3.18}
$$

System (2.3.17) supports internal gravity waves, acoustic waves and the Lamb wave and represents the link between our asymptotic framework and the classical theory of small perturbations of the state of rest for compressible stratified fluids (see [17, p. 171]). There are two major differences between the classical theory and the present case. The first one is in the equation for the vertical velocity $\overline{w^{(1)}}^{\boldsymbol{x}}$. In the classical theory such an equation is obtained through combination of vertical momentum and continuity and contains a second-order term $\partial_{tt} \overline{w^{(1)}}^{\boldsymbol{x}}$ on the left-hand side. The second difference lies in the right-hand side of (2.3.17) where $\boldsymbol{x}$-scale correlations of fluctuations of the leading-order solution, microscopical transport and radiative heating appear as forcing terms in the equations. In the classical theory these terms are absent due to linearization and the particular choice of the basic state (of rest).

The results outlined above have interesting implications for the issues of modeling and computing slow atmospheric flows. So far, we can draw the following conclusions:

1. Pressure perturbations of order $O(\mathrm{M}^2)$ affect the velocity field at leading order. Therefore, single-variable representations of the pressure field do not allow a meaningful computation of pressure gradients.

2. For stable or moderately stable stratifications, the vertical velocity w must satisfy a diagnostic constraint. This constraint takes the form of a simple relationship between vertical velocity, stratification and heating and is *not* a form of the continuity equation. This result has three implications:

   (a) Parameterizations of sub-scale physical processes involved in the energy budget (*e.g.* turbulent heat transfer) are not completely free and must satisfy an integral constraint.

   (b) The second-order perturbation pressure can be computed by solving, at each $z =$ const. level, a two-dimensional elliptic problem. The numerical solution of this problem involves a plain Laplace operator and can be computed efficiently with standard methods.

   (c) There is no truly three-dimensional motion at meso and synoptic scales. Whether numerical methods based on the unconstrained-constraint integration of the full three-dimensional equation of motion can predict vertical winds which are consistent with the asymptotic behavior of the true solution is an open question.

3. The analysis of deep convection on the micro scales reveals a vertical velocity-density perturbation dynamics which is perfectly consistent with the above-mentioned diagnostic constraint for w: in the quasi-steady limit Equation (2.3.11) simply reduces to Equation (2.3.10).

4. On meso and synoptic scales pressure tendencies can be computed by integration of a system of second-order partial differential equations which supports internal and barotropic gravity waves, acoustic waves and Lamb wave. This system is a generalization of the set of equations obtained in the classical theory of perturbations from the state of rest for compressible stratified flows.

3. Mathematical issues

In this section we review a rigorous mathematical framework for deriving the relationships commonly used in multi-scale asymptotics. For a detailed analysis we refer to [10]. For concreteness, attention is focused on the low-Mach-number limit of the Euler equations. The results, *e.g.* Lemma 3.1 and Lemma 3.2, however, are generally valid.

Motivated by observations of many systems of practical relevance, we require that each quantity, say $U(\boldsymbol{x}, t)$, is bounded in the sense that for all $\boldsymbol{x} \in \mathcal{G} \subset \mathbf{R}^d$ and for each $t \in \mathbf{R}_0^+$ there exists a time-dependent upper bound $c_U(t)$ such that

$$|U(\boldsymbol{x}, t)| \leq c_U(t). \tag{3.0.1}$$

3.1. Asymptotic expansions

The success of an asymptotic analysis depends crucially on the choice of an asymptotic sequence – the functions $\mathrm{M}^0, \mathrm{M}^1, \mathrm{M}^2 \ldots$ in, *e.g.*, Equation (2.1.22) – as well as on the choice of suitable time and space scales. These choices depend on both the governing equations and on the regime being considered. Throughout this paper, the following asymptotic sequence has been used in the analysis of low-Mach-number flows ($\epsilon = \mathrm{M}$):

$$\phi_n(\epsilon) = \epsilon^n, \ n \in \mathbf{N}_0. \tag{3.1.1}$$

The sequence satisfies

$$\phi_n(\epsilon) = o\left(\phi_{n-1}(\epsilon)\right), \ \epsilon \to 0. \tag{3.1.2}$$

The choice of this asymptotic sequence is not obvious! In the governing equation, *e.g.* in (2.1.15)–(2.1.20), the perturbation parameter is the square of the Mach number ϵ^2. In fact, in the literature one can find many asymptotic analyses which are based on the sequence $\phi_n(\epsilon) = \epsilon^{2n}$.

Using the decay property (3.1.2) one can prove the following Lemma:

Lemma 3.1 *Let $\{\phi_n(\epsilon)\}_{n\in\mathbf{N}_0}$ be an asymptotic sequence and L_n, $n = 0, \ldots, N$ arbitrary terms which are independent of ϵ. Then*

$$\sum_{n=0}^{N} \phi_n(\epsilon) L_n = o\left(\phi_N(\epsilon)\right), \ \epsilon \to 0 \tag{3.1.3}$$

holds if and only if $L_n = 0$, $n = 0, \ldots, N$.

Proof: Let us assume the existence of terms $L_0, \ldots, L_N$ with $\max_{n=0,\ldots,N} |L_n| > 0$ for which Equation (3.1.3) holds and let $m = \min_{n=0,\ldots,N, L_n \neq 0} n$. Using (3.1.2), which is supposed to hold, we obtain, for $m \leq N$:

$$\sum_{n=0}^{m} \phi_n(\epsilon) L_n = o\left(\phi_N(\epsilon)\right) - \sum_{n=m+1}^{N} \phi_n(\epsilon) L_n = o\left(\phi_m(\epsilon)\right) .$$

The last equality is a consequence of (3.1.3). Dividing by $\phi_m(\epsilon)$ and taking the limit $\epsilon \to 0$ one gets

$$\lim_{\epsilon\to 0} \frac{\sum_{n=0}^{m} \phi_n(\epsilon) L_n}{\phi_m(\epsilon)} \equiv L_m = \lim_{\epsilon\to 0} \frac{o\left(\phi_m(\epsilon)\right)}{\phi_m(\epsilon)}$$

in contradiction to the definition of m. The opposite direction is trivial.

For further detailed discussions of asymptotic sequences, asymptotic series, order symbols, etc., one may consult the classical textbooks by van Dyke [30], Schneider [1], or Kevorkian and Cole [31, 32].

Simple examples show that, in general, an asymptotic single-scale expansion can not be successfully employed in the context of problems that contain phenomena on different scales [32, 33]. The following sections provide results for single as well as multiple-scales expansions in space. The exact definitions of the asymptotic expansions are given in each section separately.

3.1.1. *Single-scale asymptotic analysis for confined domains*

In this section the Euler equations are considered in a domain $\mathcal{G} \times \mathbf{R}_0^+$ with a bounded spatial part $\mathcal{G} \subset \mathbf{R}^d$. Due to the boundedness of $\mathcal{G}$ there is always a bound $\mathrm{M}_l > 0$ such that for each $\mathrm{M} \in (0, \mathrm{M}_l)$ no phenomena on a scale $\boldsymbol{\xi} = \mathrm{M}\boldsymbol{x}$ are present in the distribution of the solution vector $\boldsymbol{u} = (\rho, m_1, \ldots, m_d, \rho e)^T$, provided we assume that $\boldsymbol{u}_{\mathrm{ref}}$ is fixed as $\mathrm{M} \to 0$. Hence, we define the asymptotic solution space $\mathcal{U}_s$ as the set of all functions $\boldsymbol{u} : \mathcal{G} \times \mathbf{R}_0^+ \times (0, \widetilde{\mathrm{M}}) \to \mathbf{R}^{d+2}$, $\widetilde{\mathrm{M}} > 0$ which satisfy the governing equations and for which each physical quantity U can be expressed by an asymptotic expansion

$$U(\boldsymbol{x}, t; \mathrm{M}) = \sum_{i=0}^{2} \mathrm{M}^i U^{(i)}(\boldsymbol{x}, t) + o(\mathrm{M}^2), \ \mathrm{M} \to 0,$$

which is valid in $\mathcal{G} \times \mathbf{R}_0^+$. To study the properties of the functions $U^{(i)}$, $i = 0, 1, 2$ we introduce the asymptotic expansion into the Euler equations and collect the terms which are multiplied by the same power of the Mach number M. These terms are functions which do not depend on M and, according to Lemma 3.1, must vanish in the limit $\mathrm{M} \to 0$. This leads to the following asymptotic system

$$\partial_t \rho^{(i)} + \nabla_{\boldsymbol{x}} \cdot \boldsymbol{m}^{(i)} = 0, \quad i = 0, 1, 2, \tag{3.1.4}$$

$$\nabla_{\boldsymbol{x}} p^{(0)} = \mathbf{0}, \tag{3.1.5}$$

$$\nabla_{\boldsymbol{x}} p^{(1)} = \mathbf{0}, \tag{3.1.6}$$

$$\partial_t \boldsymbol{m}^{(0)} + \nabla_{\boldsymbol{x}} \cdot \left(\boldsymbol{m}^{(0)} \circ \boldsymbol{v}^{(0)}\right) + \nabla_{\boldsymbol{x}} p^{(2)} = \mathbf{0}, \tag{3.1.7}$$

$$\partial_t (\rho e)^{(i)} + \nabla_{\boldsymbol{x}} \cdot ((\rho e + p)\boldsymbol{v})^{(i)} = 0, \quad i = 0, 1, 2 \tag{3.1.8}$$

in $\mathcal{G} \times \mathbf{R}_0^+$. Here we have introduced $\boldsymbol{m} := \rho \boldsymbol{v}$. The above hierarchy of equations is the starting point of the analysis presented in Section 2.1.2.

3.1.2. *Multiple-scale asymptotic analysis for unbounded domains*

In contrast to the previous section we consider a spatial domain $\mathcal{G} \subset \mathbf{R}^d$ which satisfies

$$\left(d_{\min}(\mathcal{G})\right)^{-1} = O\left(\frac{\mathrm{M}}{\ell_{\mathrm{ref}}}\right), \qquad \mathrm{M} \to 0 \tag{3.1.9}$$

with

$$d_{\min}(\mathcal{G}) := \min_{k=1,\ldots,d} |x_k|.$$

This means that, for each M, the domain $\mathcal{G}$ is large enough to accommodate perturbations of wavelength $\ell_{\mathrm{ref}}/\mathrm{M}$, *i.e.*, in dimensionless coordinates, perturbations on the large scale $\boldsymbol{\xi} = \mathrm{M}\boldsymbol{x}$. Note that this assumption implies that either $\mathcal{G} = \mathbf{R}^d$ or that $\mathcal{G}$ depends on M or that the physical dimensions of $\mathcal{G}$ are fixed, but the reference length ℓ_{ref} is proportional to M. Furthermore, without loss of generality we can require that there always exists a positive real number M' such that

$$\mathbf{B}_{\boldsymbol{x}}\left(\frac{1}{\mathrm{M}}\right) := \left\{\boldsymbol{x} \in \mathbf{R}^d \,\middle|\, |\boldsymbol{x}| < \frac{1}{\mathrm{M}}\right\} \subset \mathcal{G}$$

for all $\mathrm{M} \leq \mathrm{M}'$. To take into account multiple space scales consider the mapping

$$\begin{aligned} \boldsymbol{g} : \mathbf{R}^d \times \mathbf{R}_0^+ \times (0, \widetilde{\mathrm{M}}) \quad &\to \mathbf{R}^{2d} \times \mathbf{R}_0^+, \\ (\boldsymbol{x}, t; \mathrm{M}) \quad &\overset{\boldsymbol{g}}{\longmapsto} (\boldsymbol{x}, \mathrm{M}\boldsymbol{x}, t)\,. \end{aligned} \tag{3.1.10}$$

This mapping allows us to define a particular space $\widetilde{\mathcal{U}}_m$ of functions which are solution of the Euler equations. These are those functions U that can be expressed in $\mathcal{G} \times \mathbf{R}_0^+$ by a multiple-scale asymptotic expansion

$$U(\boldsymbol{x}, t; \mathrm{M}) = \sum_{i=0}^{j} \mathrm{M}^i \; U^{(i)}(\boldsymbol{g}(\boldsymbol{x}, t; \mathrm{M})) + o\left(\mathrm{M}^j\right), \; \mathrm{M} \to 0, \; j = 0, 1, 2,$$

which is uniformly valid outside an arbitrary large ball $\mathbf{B}_{\boldsymbol{x}}(s)$, $s \in \mathbf{R}^+$. The asymptotic functions $U^{(i)}$ depend on two space coordinates, $\boldsymbol{\eta}$ and $\boldsymbol{\xi}$:

$$\begin{aligned} U^{(i)} : \mathbf{R}^d \times \mathbf{R}^d \times \mathbf{R}_0^+ \quad &\to \mathbf{R}, \; i = 0, 1, 2 \\ (\boldsymbol{\eta}, \boldsymbol{\xi}, t) \quad &\overset{U^{(i)}}{\longmapsto} U^{(i)}(\boldsymbol{\eta}, \boldsymbol{\xi}, t)\,, \end{aligned}$$

Note that one cannot derive the uniform validity of the asymptotic expansion for $j = 0, 1$ from the fact that the asymptotic expansion is uniformly valid for $j = 2$. Therefore, it is necessary to introduce this assumption in the multiple-scale case. First, let us consider the so-called sub-linear growth condition for asymptotic functions. This condition represents a basic tool throughout the analysis.

Lemma 3.2
Let $U : \mathbf{R}^d \times \mathbf{R}_0^+ \times (0, \widetilde{\mathrm{M}}) \to \mathbf{R}$ be uniformly bounded with respect to $\boldsymbol{x}$ and M*, let $s \in \mathbf{R}^+$, and let the asymptotic multiple-scale expansion*

$$U(\boldsymbol{x}, t; \mathrm{M}) = \sum_{i=0}^{j} \mathrm{M}^i \; U^{(i)}(\boldsymbol{g}(\boldsymbol{x}, t; \mathrm{M})) + o\left(\mathrm{M}^j\right), \; \mathrm{M} \to 0$$

be valid in $\mathbf{R}^d \times \mathbf{R}_0^+$ and uniformly valid in $\mathbf{R}^d \setminus \mathbf{B}_{\boldsymbol{x}}(s) \times \mathbf{R}_0^+$ for each $j = 0, 1, 2$. Then the leading-order asymptotic function $U^{(0)}$ satisfies

$$U^{(0)}(\boldsymbol{g}(\boldsymbol{x}, t; \mathrm{M})) = o\left(|\boldsymbol{x}|^{\alpha}\right), \; \boldsymbol{x} \in \partial\mathbf{B}_{\boldsymbol{x}}\left(\frac{1}{\mathrm{M}}\right), \; \mathrm{M} \to 0 \tag{3.1.11}$$

for all $\alpha > 0$. Furthermore, the first-order and second-order asymptotic functions satisfy

$$U^{(i)}(\boldsymbol{g}(\boldsymbol{x}, t; \mathrm{M})) = o\left(|\boldsymbol{x}|\right), \; \boldsymbol{x} \in \partial\mathbf{B}_{\boldsymbol{x}}\left(\frac{1}{\mathrm{M}}\right), \; \mathrm{M} \to 0, \; i = 1, 2, \tag{3.1.12}$$

respectively.

Proof: From the uniform validity of the asymptotic expansion we have

$$U^{(i)}(\boldsymbol{g}(\boldsymbol{x}, t; \mathrm{M})) = o\left(\mathrm{M}^{-1}\right), \; \mathrm{M} \to 0 \tag{3.1.13}$$

uniformly in $\mathbf{R}^d \setminus \mathbf{B}_{\boldsymbol{x}}(s) \times \mathbf{R}_0^+$ for $i = 1, 2$. Given a null sequence $\{\mathrm{M}_n\}_{n\in\mathbf{N}}$, we define an arbitrary vector sequence $\{\boldsymbol{x}_n\}_{n\in\mathbf{N}}$ with $\boldsymbol{x}_n \in \partial\mathbf{B}_{\boldsymbol{x}}\left(\frac{1}{\mathrm{M}_n}\right)$. Now, we define the null sequence $\{\widetilde{\mathrm{M}}_n\}_{n\in\mathbf{N}}$ as a subsequence of $\{\mathrm{M}_n\}_{n\in\mathbf{N}}$ by taking only those elements which satisfy $\widetilde{\mathrm{M}}_n < s^{-1}$. Furthermore, we define the vector sequence $\{\widetilde{\boldsymbol{x}}_n\}_{n\in\mathbf{N}}$ as a subsequence of $\{\boldsymbol{x}_n\}_{n\in\mathbf{N}}$ which is given by the elements satisfying $\widetilde{\boldsymbol{x}}_n \in \partial\mathbf{B}_{\boldsymbol{X}}\left(\frac{1}{\mathrm{M}_n}\right)$. Using the uniform validity of (3.1.13), we obtain

$$0 = \lim_{n\to\infty} \frac{U^{(i)}(\boldsymbol{g}(\widetilde{\boldsymbol{x}}_n, t; \widetilde{\mathrm{M}}_n))}{\widetilde{\mathrm{M}}_n^{-1}} = \lim_{n\to\infty} \frac{U^{(i)}(\boldsymbol{g}(\widetilde{\boldsymbol{x}}_n, t; \widetilde{\mathrm{M}}_n))}{|\widetilde{\boldsymbol{x}}_n|} = \lim_{n\to\infty} \frac{U^{(i)}(\boldsymbol{g}(\boldsymbol{x}_n, t; \mathrm{M}_n))}{|\boldsymbol{x}_n|},$$

which proves (3.1.12). In order to derive Equation (3.1.11), we use the uniform boundedness of U. This yields

$$U(\boldsymbol{x}, t; \mathrm{M}) = o(r^\alpha),\ \boldsymbol{x} \in \partial\mathbf{B}_{\boldsymbol{x}}(r),\ r \to \infty \tag{3.1.14}$$

for all $\alpha > 0$. Using the asymptotic expansion, we obtain

$$U(\boldsymbol{x}, t; \mathrm{M}) = U^{(0)}(\boldsymbol{g}(\boldsymbol{x}, t; \mathrm{M})) + o(1),\ \mathrm{M} \to 0 \tag{3.1.15}$$

uniformly in $\mathbf{R}^d \setminus \mathbf{B}_{\boldsymbol{x}}(s) \times \mathbf{R}_0^+$. A simple combination of the Equations (3.1.14) and (3.1.15) leads to

$$\begin{aligned} U^{(0)}(\boldsymbol{g}(\boldsymbol{x}, t; \mathrm{M})) &= U(\boldsymbol{x}, t; \mathrm{M}) + o(1) \\ &= o\left(\mathrm{M}^{-\alpha}\right) + o(1) = o\left(|\boldsymbol{x}|^\alpha\right), \end{aligned}$$

where $\boldsymbol{x} \in \partial\mathbf{B}_{\boldsymbol{x}}\left(\frac{1}{\mathrm{M}}\right)$ and $\mathrm{M} \to 0$.

Notice that the validity of Theorem 3.2 does not depend on the special form of the mapping $\boldsymbol{g}$ and therefore the sub-linear growth condition is also valid in the case of a single-scale expansion if an unbounded domain is considered. The assumption that the physical quantity U is uniformly bounded is motivated by (3.0.1) and guarantees that we have chosen the reference values in a proper manner. Using the derivatives

$$\partial_t(U^{(i)} \circ \boldsymbol{g})(\boldsymbol{x}, t; \mathrm{M}) = \partial_t U^{(i)}(\boldsymbol{g}(\boldsymbol{x}, t; \mathrm{M})), \tag{3.1.16}$$

$$\partial_{x_j}(U^{(i)} \circ \boldsymbol{g})(\boldsymbol{x}, t; \mathrm{M}) = \partial_{\eta_j} U^{(i)}(\boldsymbol{g}(\boldsymbol{x}, t; \mathrm{M})) + \mathrm{M}\partial_{\xi_j} U^{(i)}(\boldsymbol{g}(\boldsymbol{x}, t; \mathrm{M})),\ j = 1, \ldots, d \tag{3.1.17}$$

and introducing the asymptotic expansion into the Euler equations, one obtains

$$\begin{aligned} &\partial_t \rho^{(0)} + \nabla_{\boldsymbol{\eta}} \cdot \boldsymbol{m}^{(0)} \\ &\quad + \mathrm{M}\left(\partial_t \rho^{(1)} + \nabla_{\boldsymbol{\eta}} \cdot \boldsymbol{m}^{(1)} + \nabla_{\boldsymbol{\xi}} \cdot \boldsymbol{m}^{(0)}\right) + \mathrm{M}^2\left(\partial_t \rho^{(2)} + \nabla_{\boldsymbol{\eta}} \cdot \boldsymbol{m}^{(2)} + \nabla_{\boldsymbol{\xi}} \cdot \boldsymbol{m}^{(1)}\right) \\ &\quad = o\left(\mathrm{M}^2\right),\ \mathrm{M} \to 0 \text{ in } \widetilde{\mathcal{D}}(\mathrm{M}), \end{aligned} \tag{3.1.18}$$

$$\begin{aligned} &\mathrm{M}^{-2}\nabla_{\boldsymbol{\eta}} p^{(0)} + \mathrm{M}^{-1}\left(\nabla_{\boldsymbol{\eta}} p^{(1)} + \nabla_{\boldsymbol{\xi}} p^{(0)}\right) \\ &\quad + \left(\partial_t \boldsymbol{m}^{(0)} + \nabla_{\boldsymbol{\eta}} \cdot \left(\boldsymbol{m}^{(0)} \circ \boldsymbol{v}^{(0)}\right) + \nabla_{\boldsymbol{\eta}} p^{(2)} + \nabla_{\boldsymbol{\xi}} p^{(1)}\right) \\ &\quad = o(1),\ \mathrm{M} \to 0 \text{ in } \widetilde{\mathcal{D}}(\mathrm{M}), \end{aligned} \tag{3.1.19}$$

$$
\begin{aligned}
&\partial_t(\rho e)^{(0)} + \nabla_{\boldsymbol{\eta}} \cdot ((\rho e + p)\boldsymbol{v})^{(0)} \\
&\quad + \mathrm{M}\left(\partial_t(\rho e)^{(1)} + \nabla_{\boldsymbol{\eta}} \cdot ((\rho e + p)\boldsymbol{v})^{(1)} + \nabla_{\boldsymbol{\xi}} \cdot ((\rho e + p)\boldsymbol{v})^{(0)}\right) \\
&\quad + \mathrm{M}^2\left(\partial_t(\rho e)^{(2)} + \nabla_{\boldsymbol{\eta}} \cdot ((\rho e + p)\boldsymbol{v})^{(2)} + \nabla_{\boldsymbol{\xi}} \cdot ((\rho e + p)\boldsymbol{v})^{(1)}\right) \\
&\quad = o\left(\mathrm{M}^2\right),\ \mathrm{M} \to 0 \ \text{ in } \ \widetilde{\mathcal{D}}(\mathrm{M}),
\end{aligned}
\tag{3.1.20}
$$

where the manifold $\widetilde{\mathcal{D}}(\mathrm{M})$ is defined to be

$$
\widetilde{\mathcal{D}}(\mathrm{M}) := \left\{(\boldsymbol{\eta}, \boldsymbol{\xi}, t) \in \mathbf{R}^{2d} \times \mathbf{R}_0^+ \,\middle|\, (\boldsymbol{\eta}, \boldsymbol{\xi}, t) = \boldsymbol{g}(\boldsymbol{x}, t; \mathrm{M}),\ (\boldsymbol{x}, t) \in \mathcal{G} \times \mathbf{R}_0^+ \right\}.
$$

In contrast to the single-scale expansion, the manifold $\widetilde{\mathcal{D}}$ depends on the reference parameter M and therefore we are not able to decompose the above system (3.1.18)–(3.1.20) in the same manner as described in Section 3.1.1. In order to overcome this difficulty, it is convenient to introduce the space $\mathcal{U}_m \subset \widetilde{\mathcal{U}}_m$ of those asymptotic functions $U^{(0)}$, $U^{(1)}$, $U^{(2)}$ which satisfy the Equations (3.1.18)–(3.1.20) in

$$
\mathcal{D} := \left\{(\boldsymbol{\eta}, \boldsymbol{\xi}, t) \in \mathbf{R}^{2d} \times \mathbf{R}_0^+ \,\middle|\, \boldsymbol{\xi}_j < \widetilde{\mathrm{M}}\eta_j,\ j = 1, \ldots, d \right\}
$$

and fulfill the sub-linear growth condition in the sense that, for fixed $\boldsymbol{\xi}$, one has

$$
U^{(0)}(\boldsymbol{\eta}, \boldsymbol{\xi}, t) = o\left(|\boldsymbol{\eta}|^{\alpha}\right),\ \boldsymbol{\eta} \in \partial \mathbf{B}_{\boldsymbol{\eta}}\left(\frac{1}{\mathrm{M}}\right),\ \mathrm{M} \to 0
$$

for all $\alpha > 0$ and

$$
U^{(i)}(\boldsymbol{\eta}, \boldsymbol{\xi}, t) = o\left(|\boldsymbol{\eta}|\right),\ \boldsymbol{\eta} \in \partial \mathbf{B}_{\boldsymbol{\eta}}\left(\frac{1}{\mathrm{M}}\right),\ \mathrm{M} \to 0,\ i = 1, 2.
$$

Then, in analogy with the single-scale case, we can express Equations (3.1.18) – (3.1.20) in the equivalent form

$$
\partial_t \rho^{(0)} + \nabla_{\boldsymbol{\eta}} \cdot \boldsymbol{m}^{(0)} = 0, \tag{3.1.21}
$$

$$
\partial_t \rho^{(1)} + \nabla_{\boldsymbol{\eta}} \cdot \boldsymbol{m}^{(1)} = -\nabla_{\boldsymbol{\xi}} \cdot \boldsymbol{m}^{(0)}, \tag{3.1.22}
$$

$$
\partial_t \rho^{(2)} + \nabla_{\boldsymbol{\eta}} \cdot \boldsymbol{m}^{(2)} = -\nabla_{\boldsymbol{\xi}} \cdot \boldsymbol{m}^{(1)}, \tag{3.1.23}
$$

$$
\nabla_{\boldsymbol{\eta}} p^{(0)} = \mathbf{0}, \tag{3.1.24}
$$

$$
\nabla_{\boldsymbol{\eta}} p^{(1)} = -\nabla_{\boldsymbol{\xi}} p^{(0)}, \tag{3.1.25}
$$

$$
\partial_t \boldsymbol{m}^{(0)} + \nabla_{\boldsymbol{\eta}} \cdot \left(\boldsymbol{m}^{(0)} \circ \boldsymbol{v}^{(0)}\right) + \nabla_{\boldsymbol{\eta}} p^{(2)} = -\nabla_{\xi} p^{(1)}, \tag{3.1.26}
$$

$$
\partial_t (\rho e)^{(0)} + \nabla_{\boldsymbol{\eta}} \cdot ((\rho e + p)\boldsymbol{v})^{(0)} = 0, \tag{3.1.27}
$$

$$
\partial_t (\rho e)^{(1)} + \nabla_{\boldsymbol{\eta}} \cdot ((\rho e + p)\boldsymbol{v})^{(1)} = -\nabla_{\xi} \cdot ((\rho e + p)\boldsymbol{v})^{(0)}, \tag{3.1.28}
$$

$$
\partial_t (\rho e)^{(2)} + \nabla_{\boldsymbol{\eta}} \cdot ((\rho e + p)\boldsymbol{v})^{(2)} = -\nabla_{\xi} \cdot ((\rho e + p)\boldsymbol{v})^{(1)} \tag{3.1.29}
$$

in $\mathcal{D}$. This hierarchy of equations is the starting point of the analysis presented in Section 2.1.3.

3.1.3. *Examples*

The sub-linear growth conditions stated in Lemma 3.2 provide the key to derive many of the results presented in previous sections. We discuss two examples. First, consider Equation (2.1.36) and let $p^{(0)} \in \mathcal{U}_m$. Then Equation (3.1.24) implies $p^{(0)} = p^{(0)}(\boldsymbol{\xi}, t)$. Equation (3.1.9) together with the mapping $\boldsymbol{g}$ allows the integration of (3.1.25) over the open ball $\mathbf{B}_\eta\left(\frac{1}{\mathrm{M}}\right)$. Using sub-linear growth condition, we have

$$\begin{aligned}\nabla_\xi p^{(0)} &= -\frac{1}{|\mathbf{B}_\eta\left(\frac{1}{\mathrm{M}}\right)|}\int_{\mathbf{B}_\eta\left(\frac{1}{\mathrm{M}}\right)} \nabla_\eta p^{(1)}\,\mathrm{d}\boldsymbol{\eta} = -\frac{1}{|\mathbf{B}_\eta\left(\frac{1}{\mathrm{M}}\right)|}\int_{\partial\mathbf{B}_\eta\left(\frac{1}{\mathrm{M}}\right)} p^{(1)}\cdot\boldsymbol{n}\,\mathrm{d}s \\ &= O(\mathrm{M}^d)\; O(\mathrm{M}^{1-d})\; o(\mathrm{M}^{-1}) = o(1), \qquad (\mathrm{M}\to 0).\end{aligned}$$

Hence, we obtain $p^{(0)} = p^{(0)}(t)$ and the first-order momentum equation (3.1.25) gives $p^{(1)} = p^{(1)}(\boldsymbol{\xi}, t)$ as stated in (2.1.36). In the second example we emphasize the meaning of small-scale averaging in the derivation of Equation (2.1.41). Consider the small-scale average operator

$$\overline{U}(\boldsymbol{\xi}, t) := \lim_{\mathrm{M}\to 0}\frac{1}{\left|\mathbf{B}_\eta\left(\frac{1}{\mathrm{M}}\right)\right|}\int\limits_{\mathbf{B}_\eta\left(\frac{1}{\mathrm{M}}\right)} U(\boldsymbol{\eta}, \boldsymbol{\xi}, t)\,\mathrm{d}\boldsymbol{\eta}.$$

Again, using the sub-linear growth condition, one has

$$\frac{1}{\left|\mathbf{B}_\eta\left(\frac{1}{\mathrm{M}}\right)\right|}\int\limits_{\mathbf{B}_\eta\left(\frac{1}{\mathrm{M}}\right)} \nabla_\eta p^{(2)} + \nabla_\eta\cdot\left(\boldsymbol{m}^{(0)}\circ\boldsymbol{v}^{(0)}\right)\,\mathrm{d}\boldsymbol{\eta} = o(1), \qquad (\mathrm{M}\to 0).$$

As seen above, $p^{(1)} = \overline{p^{(1)}}$. Thus, averaging the momentum equation (3.1.26) leads to

$$\begin{aligned}\mathbf{0} &= \lim_{\mathrm{M}\to 0}\frac{1}{\left|\mathbf{B}_\eta\left(\frac{1}{\mathrm{M}}\right)\right|}\int\limits_{\mathbf{B}_\eta\left(\frac{1}{\mathrm{M}}\right)} \left(\partial_t\boldsymbol{m}^{(0)} + \nabla_\eta\cdot\left(\boldsymbol{m}^{(0)}\circ\boldsymbol{v}^{(0)}\right) + \nabla_\eta p^{(2)} + \nabla_\xi p^{(1)}\right)\,\mathrm{d}\boldsymbol{\eta} \\ &= \lim_{\mathrm{M}\to 0}\frac{1}{\left|\mathbf{B}_\eta\left(\frac{1}{\mathrm{M}}\right)\right|}\int\limits_{\mathbf{B}_\eta\left(\frac{1}{\mathrm{M}}\right)} \partial_t\boldsymbol{m}^{(0)}\,\mathrm{d}\boldsymbol{\eta} + \nabla_\xi p^{(1)} \\ &= \overline{\partial_t\boldsymbol{m}^{(0)}} + \nabla_\xi p^{(1)},\end{aligned}$$

which is the first equation of system (2.1.41).

4. Numerics

4.1. Discrete identification of a multiple-scale low-Mach-number flow regime

In the following sections, unless otherwise stated, all quantities are assumed to be in dimensional form. The superscript $\hat{}$ denotes the dimensional form. For the sake of simplicity we neglect the superscript whenever its omission does not lead to misunderstandings.

The identification of a low-Mach-number long-wave regime is closely related to the determination of a discrete equivalent $\breve{M}$ of the Mach number $\hat{M} \in (0, 1]$ and to the decomposition of the primitive variables $\hat{\mathbf{U}} = (\hat{\rho}, \hat{\boldsymbol{v}}, \hat{p})^T$ needed in the multiple scale *ansatz*. In particular, the density $r\hat{h}o$ and the velocity $\hat{\boldsymbol{v}}$ can be decomposed in the form

$$\hat{\rho} = \overline{\rho} + \rho', \quad \hat{\boldsymbol{v}} = \overline{\boldsymbol{v}} + \boldsymbol{v}',$$

where the superscript $'$ denotes short wave phenomena and the overbar characterizes long-wave parts, respectively. On the other hand, it is appropriate to decompose the pressure into three terms

$$\hat{p} = \hat{p}^{(0)} + \breve{M}\hat{p}^{(1)} + \breve{M}^2\hat{p}^{(2)}. \tag{4.1.1}$$

Consider, first, the pressure decomposition. Notice that no truncation error of order $o(\breve{M}^2)$ appears in Equation (4.1.1). Here, in contrast to the *ansatz* introduced in the asymptotic analysis, the pressure splitting is exact and $\hat{p}^{(0)}$, $\hat{p}^{(1)}$, and $\hat{p}^{(2)}$ are not solutions of the asymptotic equations discussed in Section 2.1. The idea, however, is to try to construct functions $\hat{p}^{(0)}$, $\hat{p}^{(1)}$, and $\hat{p}^{(2)}$ that have the same asymptotic behavior as the corresponding pressure components of the asymptotic sequence. First, consider the leading-order pressure $\hat{p}^{(0)}$. If the reference parameter $\breve{M}$ is sufficiently small, we require $\hat{p}^{(0)}$ to be spatially homogeneous and the first-order pressure $\hat{p}^{(1)}$ has to represent exclusively long-wave phenomena. Due to the exactness of the pressure decomposition (4.1.1) the second-order pressure $\hat{p}^{(2)}$ can then be computed from $\hat{p}$, $\hat{p}^{(0)}$ and $\hat{p}^{(1)}$ and represents the remaining long- and short-wave influences. If the data are in the low-Mach- number regime, we expect this construction to provide a discrete pressure decomposition that guarantees the boundedness constraints

$$\hat{p}^{(i)} \leq C\,\hat{p}_{\text{ref}},\, i = \{1, 2, 3\}\,. \tag{4.1.2}$$

If not, we will assume the flow field not to fall into the single-time, multiple-space-scale regime considered here (notice, however, that this *ansatz* excludes multiple-time, single-space scale regimes as considered, *e.g.*, in [5], [3], [34], [35], [4] and references therein). Notice also that the constant C must be independent of $\breve{M}$.

We propose discrete-filter operations that, given a pressure distribution, determine $\breve{M}$ and the relevant underlying length scales and simultaneously provide a pressure decomposition that, in the low-Mach-number long-wave regime, satisfies the above boundedness constraint. It turns out that pressure decomposition (4.1.1), determination of an effective numerical value $\breve{M}$ corresponding to the physical Mach number M and extraction of short and long wavelengths have to be synchronized in a suitable way to achieve a decomposition satisfying the boundedness constraint (4.1.2).

Notice that if $\breve{M}$ is much smaller than the ratio between the smallest flow scale $\hat{l}_{\text{ref}}$ and the maximal diameter of the domain $\hat{\Omega}$, *i.e.*,

$$\frac{1}{\check{M}} \gg \frac{d_{\max}(\hat{\Omega})}{\hat{l}_{\text{ref}}} = d_{\max}(\Omega),$$

long-wave acoustic phenomena on a scale $\boldsymbol{\xi} = \check{M}\,\boldsymbol{x}$ cannot be accommodated and the multiple-scale expansion degenerates into a single-scale expansion. In this case computing the first-order pressure and the long-wave parts of density and velocity is inappropriate. The limit of $\check{M} = \mathrm{M} = 0$ will be discussed in more detail in Section 4.3. If we define

$$\hat{p}^{(0)}(t) := \hat{p}_{ref}(t) = \frac{1}{|\hat{\Omega}|} \int_{\hat{\Omega}} \hat{p}(\boldsymbol{x}, t)\, \mathrm{d}\boldsymbol{x},$$

then the requirements mentioned above regarding the leading-order pressure $\hat{p}^{(0)}$ hold for all $\check{M} \in (0, 1]$. Furthermore, it is possible to rewrite the pressure decomposition (4.1.1) as

$$\phi = \overline{\phi} + \phi',$$

with $\phi := \hat{p} - \hat{p}^{(0)}$, $\overline{\phi} := \check{M}\,\hat{p}^{(1)}$ and $\phi' := \check{M}^2 \hat{p}^{(2)}$. We can describe a decomposition algorithm in the following way:

Let I denote the index set of the discretization. Decompose every given signal $(f_i)_{i\in I}$ of a function f in the form

$$f_i = \overline{f}_i + f_i', \quad \forall i \in I,$$

where $(\overline{f}_i)_{i\in I}$ represents only long-wave phenomena and $(f_i')_{i\in I}$ contains the remaining long- and short-wave parts. Furthermore $(f_i')_{i\in I}$ has to be small compared to $(\overline{f}_i)_{i\in I}$ with regard to the maximum norm, i.e.

$$\|(\overline{f}_i)_{i\in I}\|_\infty \gg \|(f_i')_{i\in I}\|_\infty.$$

An optimal decomposition algorithm should satisfy the following requirements:

A. The decomposition as well as $\check{M}$ have to be calculated simultaneously to satisfy (4.1.1) and (4.1.2) in an optimal way.

B. The reference parameter $\check{M}$ should continuously depend on the data of the discretization.

C. The algorithm should be almost parameter-free and must terminate automatically.

D. The method should locally be self-adaptive with respect to the data of the discretization, *i.e.* the decomposition should be invariant in regions where the signal is sufficiently smooth.

E. Relevant features of the solution should be neither dislocated nor smoothed.

F. The algorithm must be independent of the type of discretization. It must also be robust to grid refinements and to numerical noise. In this context it seems to be worthwhile to prove the continuity of the decomposition operators used.

G. The method must be fast, since the physical quantities have to be decomposed at each time step. Thus, if n denotes the number of discretization points or control volumes, the algorithm has to be of order $O(n \log n)$ or even faster.

Due to the last requirement, averaging operators based on convolutions with a box function or a Gaussian kernel must be discarded. We also disregard filtering algorithms based on Fourier transformations. These would require certain manipulations of high frequencies associated with aliasing errors and non-periodicity of the analyzed signals. The net effects on the resulting signal components are ambiguous and hard to control, especially on unstructured grids. Besides, Fourier decomposition is a global operation.

Wavelets have local properties in space and time, but until now they are restricted to structured grids. This makes them too rigid in the context of remark (F). Furthermore, the reference parameter $\check{M}$ must be precisely determined for small values, but this is impossible by means of a single wavelet analysis. Sampling the high-frequency parts of the wavelet analysis again, it is possible for us to determine all frequencies at the cost of loosing the multiple-scale properties and the order of the algorithm.

A survey of scale-space evolution algorithms which are based on parabolic differential equations is given in [36]. Besides the advantages of a curve evolution based on linear diffusion equations there are serious problems arising in this approach (Weickert [36, p. 6]):

a. ”Gaussian smoothing does not only reduce noise, but also blurs important features such as edges and, thus, makes them harder to identify. Since Gaussian scale-space is designed to be completely uncommitted, it cannot take into account any *a-priori* information on structures which are worth being preserved (or even enhanced).

b. Linear diffusion filtering dislocates edges when moving from finer to coarser scales. So structures which are identified at a coarse scale do not give the right location and have to be traced back to the original image[..]. In practice, relating dislocated information obtained at different scales is difficult and bifurcations may give rise to instabilities. These coarse-to-fine tracking difficulties are generally denoted as the correspondence problem.”

To overcome these problems anisotropic and nonlinear diffusion processes or even reactive-diffusion filters are being considered, but these decomposition strategies are not parameter-free and controlling the termination of the resulting algorithms is still an open problem. Furthermore, the computational effort associated with this class of complex filter algorithms increases in comparison with the simpler linear diffusion approaches, which already have an operation count similar to convolution processes. Hence, such techniques are also unsuitable for the kind of problem considered.

4.1.1. *Long-wave short-wave filters based on polygonal curves*

In the area of discrete geometrical data analysis, [37], polygonal curves are simplified to extract the important visual parts neither changing the coarse structure of the borderline nor dislocating the relevant features. This is done via a step–by–step algorithm. During each curve-analysis step a certain number of successive edges are replaced by a straight line connecting the endpoints of such a set of edges. The key to success of this very simple algorithm

is hidden in the order of these replacements. In each step of the evolution a relevance measure assigns a cost value to each pair of edges. If the cost value is small, that is, the structure embraced by the pair of edges is insignificant, it will be replaced. The sequence of replacements enforced by the relevance measure produces a hierarchy of structures.

In our case a suitable relevance measure has to be defined to classify those points of a discrete distribution $(f_i)_{i\in I}$ which are not represented by the function $\overline{f}$ which has to be calculated. Then, the values of these points have to be replaced to give $\overline{f}$ some kind of discrete smoothness.

First of all, we must derive an appropriate definition to distinguish long-wave and short-wave phenomena. In contrast to the Fourier *ansatz* we will call any function to be of long-wave type, if the distance between its turning points is sufficiently large. On the basis of this definition, a sine function belongs to the same class as an arbitrary function having equivalent minimal distances between its turning points.

This definition of 'long-waviness' suffers from the drawback that high-frequency parts in the sense of Fourier can conceal themselves in long-wave structures. An example is given by a wave steepening into a shock. Although the frequency increases rapidly with respect to the Fourier series, the distance between two turning points can still remain constant during the steepening process. Consequently, the wavelength of the function as defined by our 'turning point' measure is constant. Thus, it might be necessary to execute a Fourier analysis of the signal *after* it has been decomposed.

Generally, in areas with short-wave structures turning points are very frequent, whereas in areas with long wave structures only a few turning points can be found. We will exploit this property of the wavelength to define a cost function and finally derive the relevance measure.

4.1.2. *A discrete-wavelength decomposition algorithm*

For the sake of simplicity we confine ourselves to a single-space dimension. Let $(\sigma_i)_{i\in I}$ be a given disjunct decomposition of the domain Ω into control volumes, boxes for short. Let I be an index set and n its size: $n := \#(I)$. We associate the values $(f_i)_{i\in I}$ to the centers of the boxes. Connecting each value with its neighbors with a segment leads to a piecewise linear function comparable to the polygonal contours investigated in [38]. We denote an edge connecting the values f_i and f_{i+1} by $k_{i+\frac{1}{2}}$ and the turn angle (the angle enclosed by the edges $k_{i-\frac{1}{2}}$ and $k_{i+\frac{1}{2}}$) by α_i.

Using the sign of α_i, we can now subdivide the domain Ω into overlapping concave and convex subdomains Ω_j, $j \in J$, where J denotes the index set of subdomains. Each sub-domain consists of points with the same sign of the turning angle plus the left and right turning points. Therefore, each point on the boundary of a sub-domain is called a discrete turning point of the function f. Note that discrete turning points always appear in pairs. Between a pair of turning points there might be points with vanishing turning angles.

The discrete-curve decomposition of a function f produces a sequence of functions $\{f^0 = f, \ldots, f^m\}$ and a sequence of index sets $\{I^0 = I, \ldots, I^m\}$ with $\#I^{l+1} < \#I^l$ and $\#I^m \leq 2$. In this description the index set I^l denotes those points which are still unchanged at the beginning of the l-th decomposition step. To determine those points which are to be removed during the l-th step, every point f_i^l, $i \in I^l$, is allocated a cost value $k(i, I^l) \in \mathbf{R}^+$ via the relevance measure to be determined in the next section. Let

$$k_{\min}(I^l) := \min\{k(i, I^l) : i \in I^l\}.$$

The set $I_{\min}(I^l)$ denotes the set of points with minimal costs at the l-th step,

$$I_{\min}(I^l) := \{i \in I^l : \ k(i, I^l) = k_{\min}(I^l)\}.$$

Now the algorithm removes the index set $I_{\min}(I^l)$ from I^l,

$$I^{l+1} = I^l \setminus I_{\min}(I^l).$$

4.1.3. *The relevance measure and the singular reference parameter*

The relevance measure represents the significance of each individual structure compared to all others and therefore controls the sequence of the decomposition steps.

In our case the relevance measure should be characterized by the wavelength of the function. The wavelength itself was fixed by the distance of the turning points from each other. So the cost function of a cell average f_i should primarily be a function of the sum of the distances from its neighboring turning points with different signs of the turning angles compared to the angle at index i. The cost function should only secondarily depend on other properties like its relative position between its turning points or its curvature. The sum of the distances to the so-called neighboring turning points are equal to the length of the concave or convex subdomains $|\Omega_j|$ projected onto the x-axis. Note that σ_i can be a member of up to three different subdomains. Because the number of subdomains changes during the evolution, we also introduce a sequence of index sets $\{J^0 = J, \ldots, J^m\}$ of subdomains Ω_j.

Now, define the cost function $k(i, I^l) \in \mathbf{R}^+$ to be

$$k(i, I^l) := \Big| \min_{j \in \{J^l,\ \sigma_i \in \Omega_j\}} |\Omega_j| - \min_{j \in J^l} |\Omega_j| \Big| * |\alpha_i|, \quad \forall i \in I^l. \tag{4.1.3}$$

Obviously, the cost function represents a non-negative function which is equal to zero for all points of the smallest sub-domain. Hence, in addition to the points with collinearly arranged function values, all points of the smallest sub-domain are removed during the next step.

If we define the minimal wavelength of the function f_l as the minimal distance of two neighboring subdomains $\Omega_j,\ \Omega_{j+1}$, *viz.*,

$$\lambda_{\min}(f^l) := \min_{j \in J^l} \left(|\Omega_j| + |\Omega_{j+1}| - |\Omega_j \cap \Omega_{j+1}| \right)$$

with $\Omega_j := \emptyset,\ \forall j \notin J^l$, then the inequality

$$\lambda_{\min}(f^l) \leq \lambda_{\min}(f^{l+1})$$

does not hold for all $l \in \{0, \ldots, (m-1)\}$, in general. Nevertheless, for the stopping criterion, it follows

$$\lambda_{\min}(f^0) \leq \lambda_{\min}(f^m) = |\Omega|.$$

In the case $\lambda_{\min}(f^0) \neq |\Omega|$ the inequality is sharp. Thus, the minimal wavelength increases during the evolution, although it is theoretically possible that the progress is not monotone.

Now we can easily define the reference parameter $\check{M}$ as

$$\check{M}(f^l) := \min \left\{ \frac{1}{\lambda_{\min}(f^l)}, 1 \right\}. \tag{4.1.4}$$

4.1.4. *Properties of the scale-decomposition scheme*

A summary of all steps of the algorithm described in the previous chapters is now given:

1. Set $\check{M} = 1,\ l = 0,\ \overline{f}_i = f_i,\ f_i' = 0,\ \forall i \in I^0 = I$;
2. Subdivide Ω into overlapping concave and convex subdomains Ω_j of the function $\overline{f}_i,\ \forall i \in I^0$;
3. Compute $\check{M}$ by means of Equation (4.1.4) and check the validity of the estimates in (4.1.2) as well as $\#I^l > 2$. If one of these conditions is not satisfied, the evolution is stopped;
4. Assign a relevance measure $k(i, I^l)$ to each box $\sigma_i,\ i \in I^l$, using the cost function (4.1.3);
5. Compute $I_{\min}(I^l) = \{i \in I^l : k(i, I^l) = 0\}$;
6. Reduce the index set of the maintained function values,
   $I^{l+1} = I^l \setminus I_{min}(I^l)$;
7. Compute $\overline{f}_i,\ i \in I^0 \setminus I^{l+1}$ taking the maintained points $f_i,\ i \in I^{l+1}$ into account;
8. Compute $f_i' = f_i - \overline{f}_i,\ i \in I^0 \setminus I^{l+1}$;
9. Increase the index of the evolution, $l = l + 1$;
10. Go to (2.).

We add some remarks regarding the smoothness of the discrete function $\overline{f}$. The use of a simple linear interpolation in order to define discrete values for the smooth function $\overline{f}$ at those points which are actually removed does not lead to a suitable recovery procedure, since it is possible that all points in larger parts of the domain have been removed. The tempting alternative of cubic splines has the considerable disadvantage that it may or may not generate new turning points. This would necessitate a recursive decomposition procedure with an undetermined, possibly infinite number of steps until termination.

We have decided to employ the following *ansatz*. First of all, we add some of the removed points in such a way that no additional turning points are introduced. Only then we apply one of the recovery techniques mentioned above. The resulting scheme yields good results already in the case that the recovery step is given in the form of a linear interpolation documented in Section (4.1.5) below.

In [38] those properties which are independent of the relevance measure chosen are jointly employed in the numerical framework. Now, we want to investigate in addtion the properties that are dependent on the underlying relevance measure (4.1.3) in order to introduce them in a proper manner.

a. The decomposition of the pressure is enforced simultaneously with the computation of the reference parameter. During each step of the decomposition procedure the wavelength of the smoothed function increases, while the reference parameter will decrease.

b. The accuracy of the value of $\check{M}$ depends only on the quality of the discretization.

c. The algorithm is parameter-free and terminates automatically. At the end of the evolution process a straight line is obtained, if $\#I^{ab} \leq 2$.

d. The method is self-adaptive to the data. Due to the chosen relevance measure, only subdomains of Ω including short-wave phenomena will be processed during one decomposition step. All other points remain unchanged.

e. The scheme does not introduce any shape-rounding effects and there is no dislocation of relevant features, because the remaining points do not change their values.

f. The cost function is not continuous and passes this property to the algorithm employed to decompose the physical quantities. Nevertheless, owing to the fact that parts of the domain Ω are treated as a whole in the evolution, numerical experiments emphasize that the splitting does not depend on the discretization. Furthermore, noise is a short-wave phenomenon and therefore noise elimination takes place in the early stages of the evolution process.

g. The algorithm requires $O(n \log n)$ operations.

4.1.5. *Numerical results*

We have chosen two one-dimensional test cases to demonstrate the numerical accuracy of the decomposition algorithm. In both cases we use a regular discretization of the domain $\Omega = [-51, 51]$ into control volumes σ_i with $|\sigma_i| = \frac{1}{10},\ \forall i \in I, I = \{0, \ldots, 1019\}$.

First, we considered a long sinusoidal pressure wave ($\check{M} = \frac{1}{102}$) which is disturbed by a regular short-wave noise function,

$$\hat{p} = \hat{p}^{(0)} + \check{M}\hat{p}^{(1)} + \check{M}^2\hat{p}^{(2)}$$

with the reference of the pressure $\hat{p}_{\text{ref}}$ set to $\hat{p}_{\text{ref}} = \frac{4}{\check{M}^2}$ and

$$p^{(0)} = 1,\ p^{(1)} = 2\gamma(1 + \cos(2\pi\check{M}x),\ p^{(2)} = 2\gamma \sin(80\pi\check{M}x).$$

Figures 1 and 2 show the analytical long- and short-wave components of the pressure wave $\hat{p}$. The total pressure distribution defined the by adding of long- and short-wave components is shown in Figure 3. In Figures 4 and 5 the decomposed long- and short-wave components are plotted. The long-wave part of the pressure is reproduced very well and it is separated from the short-wave perturbation. There are only two pairs of turning points left, so the reference parameter $\check{M}$ has taken the value of the frequency of the analytical pressure wave in a natural way.

The other example is concerned with a density distribution moving in a long-wave acoustic field. The initial conditions are

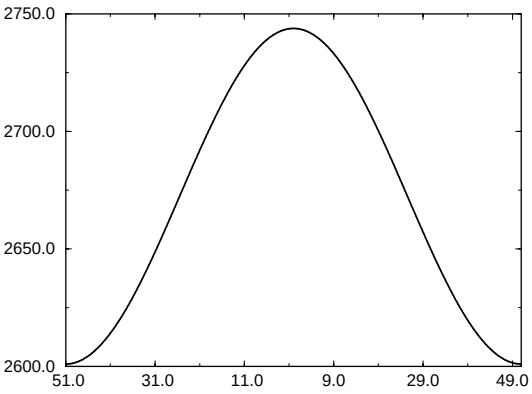

Figure 1. Long wave pressure part.

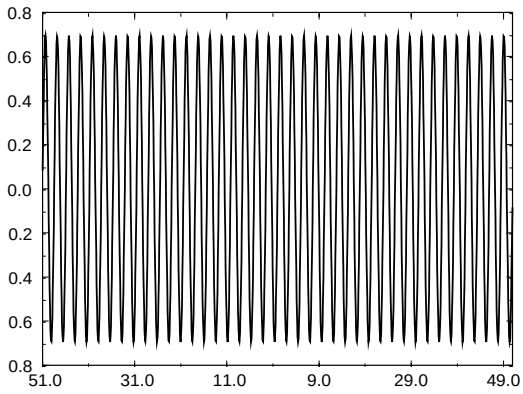

Figure 2. Pressure perturbation.

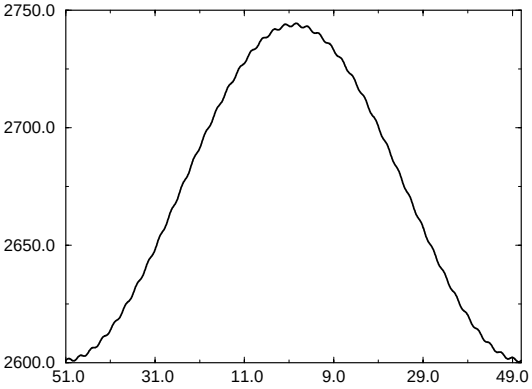

Figure 3. Total pressure distribution $\hat{p}$.

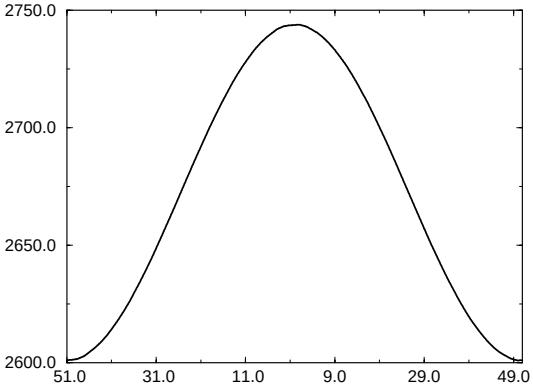

Figure 4. Filtered long wave part.

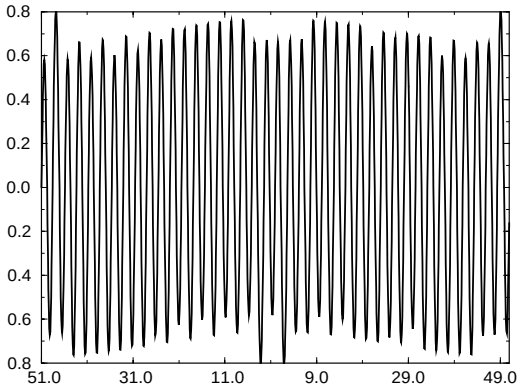

Figure 5. Remaining noise.

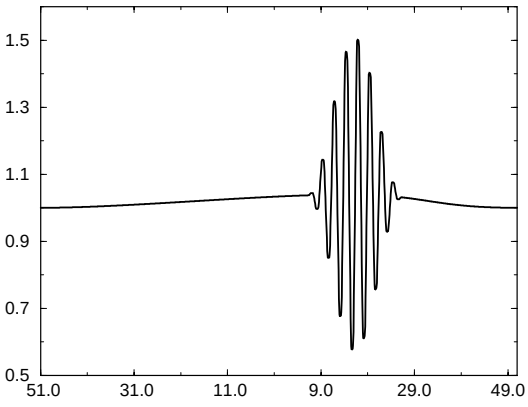

Figure 6. Density profile.

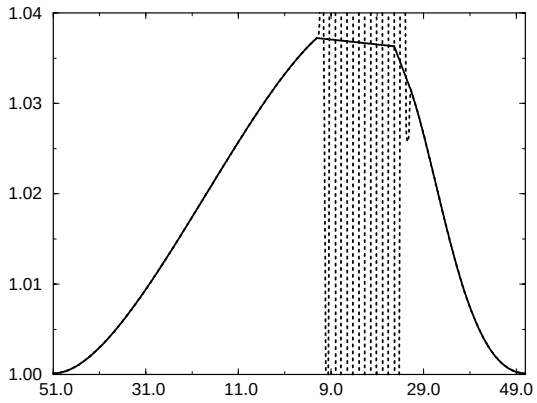

Figure 7. Filtered long wave signal.

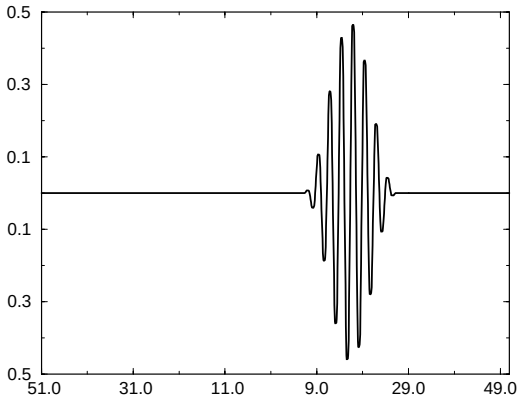

Figure 8. Short wave oscillations.

$$\hat{\rho}(x, t=0) = 1 + \frac{1}{51}\left(1 + \cos\left(\frac{2\pi x}{102}\right)\right) + \Phi(x)\frac{1}{2}\sin\left(\frac{80\pi x}{102}\right),$$

$$\hat{v}(x, t=0) = \sqrt{\gamma}\left(1 + \cos\left(\frac{2\pi x}{102}\right)\right),$$

$$\hat{p}(x, t=0) = 51^2\left(1 + \frac{\gamma}{51}\left(1 + \cos\left(\frac{2\pi x}{102}\right)\right)\right),$$

and

$$\Phi(x) = \begin{cases} \frac{1}{2}\left(1 - \cos(\frac{10\pi x}{102})\right), & \text{if } 0 \le x \le \frac{102}{5}, \\ 0 & \text{otherwise.} \end{cases}$$

The signal of the density is filtered at time $T = 5,071$.

This example clearly shows the advantages of the proposed decomposition algorithm. The decomposition is almost completely restricted to the sub-domain where the short-wave oscillations of the density distribution are found. In the other parts of Ω the filtered function and the original one are almost the same, neglecting numerical noise of size 10^{-6}. Therefore, no shape-rounding effects have taken place.

4.2. Extension of incompressible methods to weakly compressible flows

In the following we will show how to use the asymptotic analysis described in Section 2 to extend an incompressible method to the weakly compressible regime. Incompressible solvers are usually based on the primitives variables. We adopt this formulation here and use a staggered grid to stabilize the pressure-velocity coupling. We restrict ourselves to describing the extension of a projection method. The modification for the SIMPLE-type scheme is given in [39].

4.2.1. *A compressible projection method*

Projection methods for incompressible flows have been introduced by Chorin [40, 41]. In such methods discrete approximate solutions to the incompressible Navier-Stokes equations are advanced in time through two steps. First, the new-time-level density and an intermediate velocity field are obtained by a discrete integration of the convection-diffusion system

$$\begin{aligned} &\rho_t + \boldsymbol{v} \cdot \nabla \rho = 0, \\ &\boldsymbol{v}_t + (\boldsymbol{v} \circ \nabla)\, \boldsymbol{v} = -\frac{1}{\rho \mathrm{Re}} \nabla \cdot \tau, \end{aligned} \tag{4.2.1}$$

over $t^n < t \leq t^{n+1}$ with the old-time-level distributions $\boldsymbol{v}^n$, ρ^n as initial data

$$\boldsymbol{v}(t^n) = \boldsymbol{v}^n \qquad \rho(t^n) = \rho^n \,. \tag{4.2.2}$$

(Note that the original method was designed for constant density flow, for which (4.2.1a) is void. The density-advection equation is ignored.)

The auxiliary velocity field $\boldsymbol{v}^{*,n+\frac{1}{2}}$ obtained from this step is not divergence-free due to the absence of the pressure gradient in the momentum equation. A correction is constructed through discrete integration over $t^n < t \leq t^{n+1}$ of the projection equation

$$\boldsymbol{v}_t + \frac{1}{\rho} \nabla p^{(2)} = 0, \tag{4.2.3}$$

with the intermediate field $\boldsymbol{v}^{*,n+\frac{1}{2}}$ as initial data, and with the divergence constraint for the new-time-level velocity field,

$$\nabla \cdot \boldsymbol{v}^{n+1} = 0 \,. \tag{4.2.4}$$

In the weakly compressible regime, we split the full compressible Navier-Stokes equations into two subsystems in a similar way. The convection-diffusion system now reads as

$$\begin{aligned} \rho_t + \boldsymbol{v} \cdot \nabla \rho \quad &= 0, \\ \boldsymbol{v}_t + (\boldsymbol{v} \circ \nabla)\, \boldsymbol{v} \ &= -\frac{1}{\rho \mathrm{Re}} \nabla \cdot \tau, \\ p_t + \boldsymbol{v} \cdot \nabla p \quad &= 0, \end{aligned} \tag{4.2.5}$$

and the 'sonic' system as

$$\begin{aligned} \rho_t + \rho \nabla \cdot \boldsymbol{v} \quad &= 0, \\ \boldsymbol{v}_t + \frac{1}{\mathrm{M}^2 \rho} \nabla p \ &= 0, \\ p_t + \gamma p \nabla \cdot \boldsymbol{v} \ &= \frac{\gamma}{\mathrm{Pr}\, \mathrm{Re}} \nabla \cdot q, \end{aligned} \tag{4.2.6}$$

which contains all effects that spread with sound velocity and degenerate to an elliptic constraint as $\mathrm{M} \to 0$. Heat conduction with heat flux q is retained here, since it influences the divergence constraint as seen in Equation (2.1.30) whereas diffusion does not. Neglecting the viscous and heat-conduction terms, we may call this decomposition a hyperbolic-elliptic

splitting that is motivated by the wave speed as mentioned above, but also by the asymptotic analysis, (see [2, 39]). In the system (4.2.5) all the terms which are associated with elliptic expressions in the zero-Mach-number limit are neglected.

The convection-diffusion system is discretized by means of an explicit MUSCL-type upwind scheme for the convective terms and implicit second-order central differences for the diffusion part. Thus, the CFL-time step condition contains only the finite flow velocity.

The sonic system is discretized implicitly to avoid time-step restrictions due to the sound velocity tending to infinity in the limit. Here, the pressure expansion $p\left(\mathbf{x}, t; \hat{\mathrm{M}}\right) = p^{(0)}(t) + \hat{\mathrm{M}} p^{(1)}(\xi, t) + \hat{\mathrm{M}}^2 p^{(2)}(\bar{\mathbf{x}}, \xi, t)$ comes into play. Notice that the numerical parameter $\hat{\mathrm{M}}$ is now identified with the Mach number M, as we consider a case where compressibility effects do not change dramatically as the solution evolves in time. First, the total pressure has to be decomposed into its leading, first- and second-order contributions. Using the fact the leading-order pressure $p^{(0)}$ becomes constant on both space scales and the first-order term $p^{(1)}$ on the small space scale, they may be defined by averaging procedures,

$$p^{(0)} := \frac{1}{|V|} \int_V p \, \mathrm{d}V, \tag{4.2.7}$$

and

$$p^{(1)} := \frac{1}{\hat{\mathrm{M}}|V_{\mathrm{ac}}|} \int_{V_{\mathrm{ac}}} \left(p - p^{(0)}\right) \mathrm{d}V, \tag{4.2.8}$$

where V_{ac} is the acoustic domain. On a two-dimensional Cartesian grid of constant grid spacing h and coordinates x and y, V_{ac} is the rectangle $[x-h/(2\mathrm{M}), x+h/(2\mathrm{M})]\times[y-h/(2\mathrm{M}), y+h/(2\mathrm{M})]$. The second-order pressure $p^{(2)}$ then becomes

$$p^{(2)} := \frac{1}{\hat{\mathrm{M}}^2}\left(p - p^{(0)} - \hat{\mathrm{M}} p^{(1)}\right). \tag{4.2.9}$$

for consistency. For $\hat{\mathrm{M}} \to 0$, the acoustic domain exceeds the computational domain and $p^{(1)}$ becomes zero and drops out of the equations. As $\hat{\mathrm{M}}$ becomes very small, but non-zero, the influence of the pressure term $p^{(2)}$ on the thermodynamics of the system becomes negligible. It is thus regarded as a new variable independent of the total thermodynamic pressure, which is consistent with the earlier asymptotic results.

The temporal evolution of $p^{(0)}$ and $p^{(1)}$ can be determined from (2.1.32) and (2.1.44). From Equation (2.1.32), we obtain $p_t^{(0)}$ by applying a suitable ODE-integrator. To determine $p_t^{(1)}$, the acoustic system (2.1.44) has to be solved. To do so, we have two possibilities. The first is that the large-scale derivatives ∇_ξ are replaced by $\nabla_x/\hat{\mathrm{M}}$ using the chain rule and the equations are solved on the same grid as used to resolve the flow structures. This requires an implicit scheme, since the time step for an explicit scheme would be restricted by a CFL-condition including the speed of sound. Thus, the time step would tend to zero for $\hat{\mathrm{M}} \to 0$. On the other hand, Equations (2.1.44) include only large scale effects. No resolution of short-scale phenomena is necessary and a much coarser grid can be used. The coarsening factor is known to be $1/\hat{\mathrm{M}}$, which is the factor between the two space scales $\boldsymbol{x}$ and $\boldsymbol{\xi}$. In a discretization based on such an adapted coarse grid the Mach number cancels from the CFL-condition for the acoustic equations and they can be solved explicitly with low computational effort. The only potentially expensive computational step remains the extraction of the appropriate long-wave solution components needed to initiate the coarse-grid time step. The naïve integral filters from

(4.2.7), (4.2.8) must be replaced by more elaborate techniques as discussed in Section 4.1 to overcome this obstacle.

System (4.2.6) is solved in the following way. Introducing the pressure decomposition and rewriting it as a system for density, velocity and the incompressible pressure $p^{(2)}$, we obtain

$$\begin{aligned} \rho_t + \rho\nabla\cdot\boldsymbol{v} &= 0, \\ \boldsymbol{v}_t + \frac{1}{\rho}\nabla p^{(2)} &= -\frac{1}{\hat{\mathrm{M}}\rho}\nabla p^{(1)}, \\ \hat{\mathrm{M}}^2 p_t^{(2)} + \gamma p\nabla\cdot\boldsymbol{v} &= \frac{\gamma}{\mathrm{Pr\,Re}}\nabla\cdot q - p_t^{(0)} - \hat{\mathrm{M}}p_t^{(1)}. \end{aligned} \tag{4.2.10}$$

For $q = 0$, this system can be viewed as the second step of the incompressible projection method since the right-hand sides of Equations (4.2.10b) and (4.2.10c) vanish for $\hat{\mathrm{M}} \to 0$ and the equations coincide with system (4.2.6).

Equations (4.2.10) are solved by nested iterations. All equations are discretized implicitly. Then, the density is fixed at the value obtained from the convection-diffusion step solving Equations (4.2.5). The leading- and first-order pressure terms at the new time level are already determined, $p^{(0),n+1} = p^{(0),n} + \Delta t p_t^{(0)}$ and $p^{(1),n+1} = p^{(1),n} + \Delta t p_t^{(1)}$, where $p^{(0),n}$ and $p^{(1),n}$ are obtained from the discretized Equations (4.2.7), (4.2.8). The old-time-level pressure $p^{(2),n}$ was given by Equation (4.2.9), the one at the new time level has to be guessed. Usually, it is either assumed to be $p^{(2),*} = p^{(2),n}$ or $p^{(2),*} = 0$. Then, the estimate for the total pressure at the next time level is set according the consistency condition $p^* = p^{(0),n+1} + \hat{\mathrm{M}}p^{(1),n+1} + \hat{\mathrm{M}}^2 p^{(2),*}$. With these, the new time level velocity $\boldsymbol{v}^*$ can be guessed from the discretized velocity equation (4.2.10b). The new-time-level pressure can then be set to be the guess plus a correction,

$$p^{(2),n+1} = p^{(2),*} + \delta p^{(2)}, \qquad p^{n+1} = p^* + \hat{\mathrm{M}}^2\delta p^{(2)}. \tag{4.2.11}$$

Inserted into the discretized pressure equation (4.2.10c), a Poisson-equation is obtained for the pressure-correction term $\delta p^{(2)}$ which reads as

$$\begin{aligned} &\frac{\hat{\mathrm{M}}^2}{\Delta t}\delta p^{(2)} - \gamma p^*\nabla\cdot\left(\tfrac{\Delta t}{\rho}\nabla\delta p^{(2)}\right) = \\ &\quad -\gamma p^*\nabla\cdot\boldsymbol{v}^* + \frac{\gamma}{\mathrm{Re\,Pr}}\nabla\cdot q - p_t^{(0)} - \hat{\mathrm{M}}p_t^{(1)} \\ &\qquad -\frac{\hat{\mathrm{M}}^2}{\Delta t}\left(p^{(2),*} - p^{(2),n}\right). \end{aligned} \tag{4.2.12}$$

The estimate p^* for the total pressure is used as the linearisation term here. With the solution $\delta p^{(2)}$ of this equation, the estimates $p^{(2),*}$ and p^* are improved according to (4.2.11), the corresponding velocity estimate is calculated and the process is repeated up to convergence. With the velocity obtained from this inner iteration, a new density estimate is obtained and the inner loop is started again. Most of the computing time for the simulation is spent in solving the linear system resulting from discretizing the pressure-correction equation (4.2.12). For this we use preconditioned Krylov-Subspace schemes or multi-grid techniques.

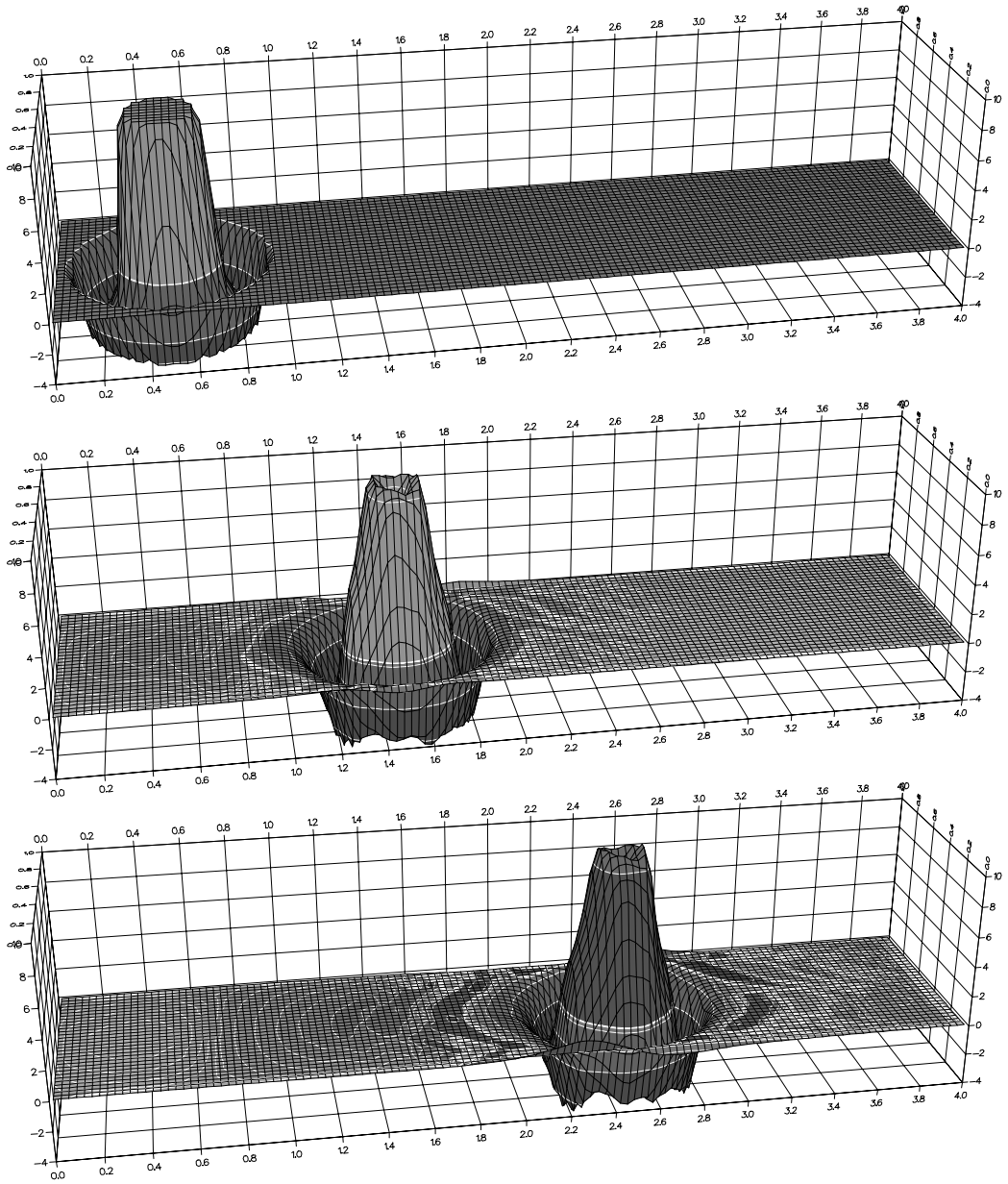

Figure 9 Vorticity at times t=0,1,2.

4.2.2. *Numerical results*

The algorithm given above does not depend on any special spatial discretization. For the numerical examples to be given now, a Cartesian staggered-grid arrangement was applied defining the scalar variables at the cell centers, the horizontal vector components on the vertical cell interfaces and the vertical components on the horizontal interfaces. As already mentioned, the convection-diffusion system (4.2.5) uses an explicit MUSCL-type scheme for the convective terms, and implicit central differences for the diffusive part. The sonic system

Figure 10. Streamline visualization of the lid driven cavity flow at Re = 1000.

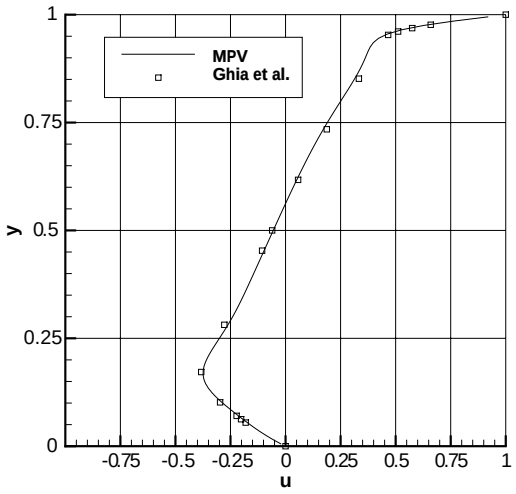

Figure 11. Horizontal velocity at the vertical cross section through the center of the cavity.

(4.2.10) is discretized with implicit central differences for all terms.

Gresho and Chan's transported vortex. The first test case is an incompressible Euler calculation proposed by Gresho [43, 44] as a test case with known, but non-trivial solution. A triangular vortex is convected through a channel while revolving around its center. It should be transported without any damping of the vorticity. Figure 9a shows the vorticity distribution at the initial stage, Figures 9b and 9c the vorticity after one and two turnarounds. The vortex is transported one spatial unit to the right during one revolution.

It can be clearly seen, that the vorticity is well reproduced. There is only limited damping of the magnitude; the distortions are due to the fact that a rotational symmetric vortex has to be approximated on a Cartesian grid. These asymmetries are reduced with grid refinement. The calculations shown here have been carried out on a 160×40 mesh for a 4×1-units domain.

The standard driven cavity test. This second test case involves an incompressible viscous flow at Reynolds number Re = 1000. It is characterized by a large vortex in the center of the cavity and two smaller ones in the lower left and right corners, see Figure 10.
The computational domain is the unit square, discretized by 100×100 grid points. At first, the standard incompressible test case is compared to results in the literature. Figure 11 shows the horizontal velocity at the vertical cross section at $x = 0{\cdot}5$, Figure 12 the vertical velocity at y=0·5. The solid lines show the results obtained with the MPV code. They are in very good agreement with the benchmark solutions obtained by Ghia *et al.* [45] on a 129×129 Cartesian grid.
Driven cavity with differentially heated side-walls. The driven-cavity test case can be extended to the weakly compressible regime by differential heating of the vertical walls. The left wall was kept at constant temperature of $30°C$ $(293{\cdot}6K)$. The right wall was heated to $293{\cdot}6K + \Delta T$. As long as the temperature difference ΔT is small, the Boussinesq approximation can

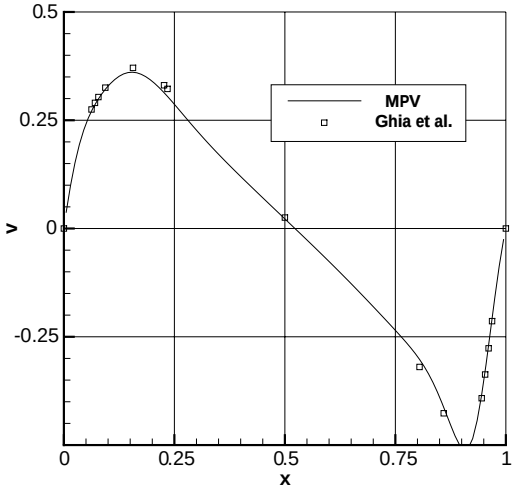

Figure 12. Vertical velocity at the horizontal cross section through the center of the cavity.

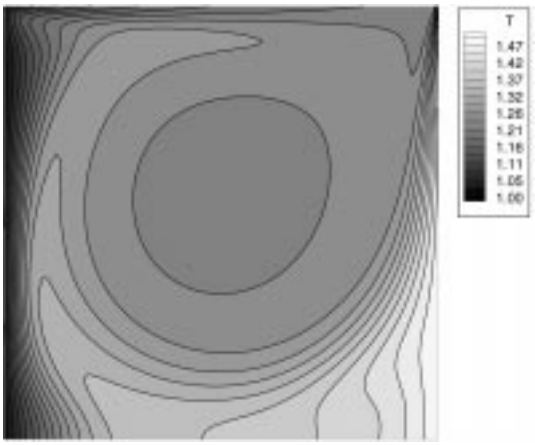

Figure 13. Isotherms for a driven cavity with differentially heated vertical walls with temperature difference $\Delta T = 150$ K..

be applied. Results of calculations with the full MPV-scheme and incompressible calculations involving the Boussinesq approximation were quite similar in this case. For ΔT larger than a few degrees, the Boussinesq approximation is no longer valid. To show this discrepancy, we applied a temperature difference $\Delta T = 150K$ and compared the results of the MPV scheme with those obtained by an incompressible Boussinesq approximation. The Mach number for this test case is $M = 0{\cdot}0005$, the Prandtl number $Pr = 0{\cdot}7$ and the Reynolds number Re $=$ 1000 as above. Figure 13 shows the temperature distribution of the steady state.

Figures 14 and 15 show the temperature profiles at the left and right walls.
The solid lines give the results of the MPV scheme, the dashed lines are the results obtained by means of an incompressible solver with Boussinesq approximation. It can be clearly seen that the incompressible code shows a much thicker thermal boundary layer than the MPV scheme. This is due to the fact that it cannot reproduce the thermal density changes.

Baroclinic vorticity generation by long-wave acoustics. The next test problem considered is again a weakly compressible one and shows the approximation of acoustic waves. Here, we want to show the interaction of a long-wave-length acoustic wave with small entropy fluctuations on the local length scale. The initial data,

$$\begin{aligned}
\rho(x, y, 0) &= 1{\cdot}0 + 0{\cdot}2M(1{\cdot}0 + \cos(\pi x/L)) + \Phi(y) \\
p(x, y, 0) &= 1{\cdot}0 + M\gamma(1{\cdot}0 + \cos(\pi x/L)) \\
u(x, y, 0) &= \sqrt{\gamma}(1 \cdot 0 + \cos(\pi x/L)), \\
v(x, y, 0) &= 0{\cdot}0,
\end{aligned}$$

with

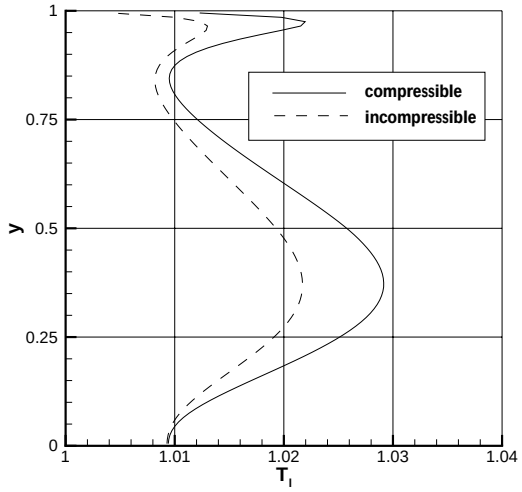

Figure 14. Horizontal velocity at the vertical cross section through the center of the cavity.

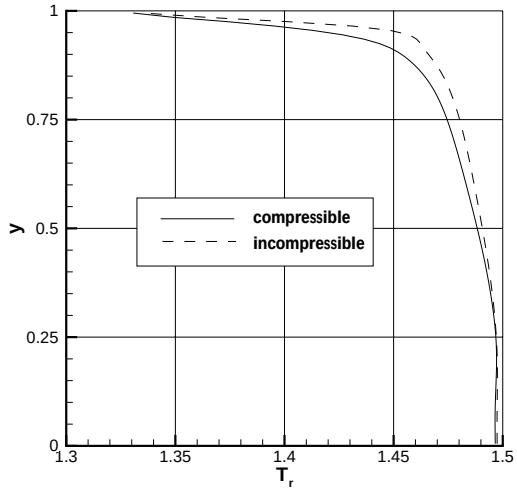

Figure 15. Vertical velocity at the horizontal cross section through the center of the cavity.

$$\Phi(y) = \begin{cases} \frac{0{\cdot}8}{L_y} y & \text{for } 0 \le y \le \frac{1}{2}L_y, \\ \frac{0{\cdot}8}{L_y}\left(y - \frac{1}{2}L_y\right) - 0{\cdot}4 & \text{for } \frac{1}{2}L_y \le y \le L_y, \end{cases}$$

represent a saw-tooth-like density stratification in the vertical direction set into motion by a right-running acoustic pulse in the horizontal direction. At $\hat{\mathrm{M}} = 1/20$, the computational domain is a double-periodic domain of $[-L : L] \times [0 : L_y]$ with $L = \frac{1}{\hat{\mathrm{M}}} = 20$ and $L_y = \frac{2L}{5} = 8$, just long enough to let one period of the acoustic wave take place. Due to the non-homogeneous density, the fluid is subject to a higher acceleration for lower density values and a lower acceleration at higher densities. This leads to the well-known phenomenon of baroclinic instability. A shear layer of sinusoidal shape is generated and moved with the acoustic wave. Figure 16 shows the density at different times. The first plot shows the initial data, the second one the first forming of the sinusoidal shape at time $t = 6$. The interface starts rolling up and small vortices are formed. This can be clearly seen at the later times $t = 9, 11, 14$.

The smallest structures resolved have a thickness of a few grid zones length, smaller ones are damped out by numerical viscosity. In Figure 17 vorticity contours are given at the same times. It can be seen that in the initially vortex-free flow two thin regions of vorticity are created along the density interface. As the interface starts rolling up, counter-rotating vortices are formed. These computations demonstrate that the interaction of the long-wave-length acoustic wave with the local flow structures creates small-scale vortices.

A model problem for the flow in a disk brake. Here we discuss some simulations of the cooling flow in a simplified disk-brake facility. The key issue in this problem is the increase of the rate of heat transport due to the stripping of the boundary layer by the brake block. To study this problem, the heat-transport coefficient is evaluated qualitatively and the physical phenomena

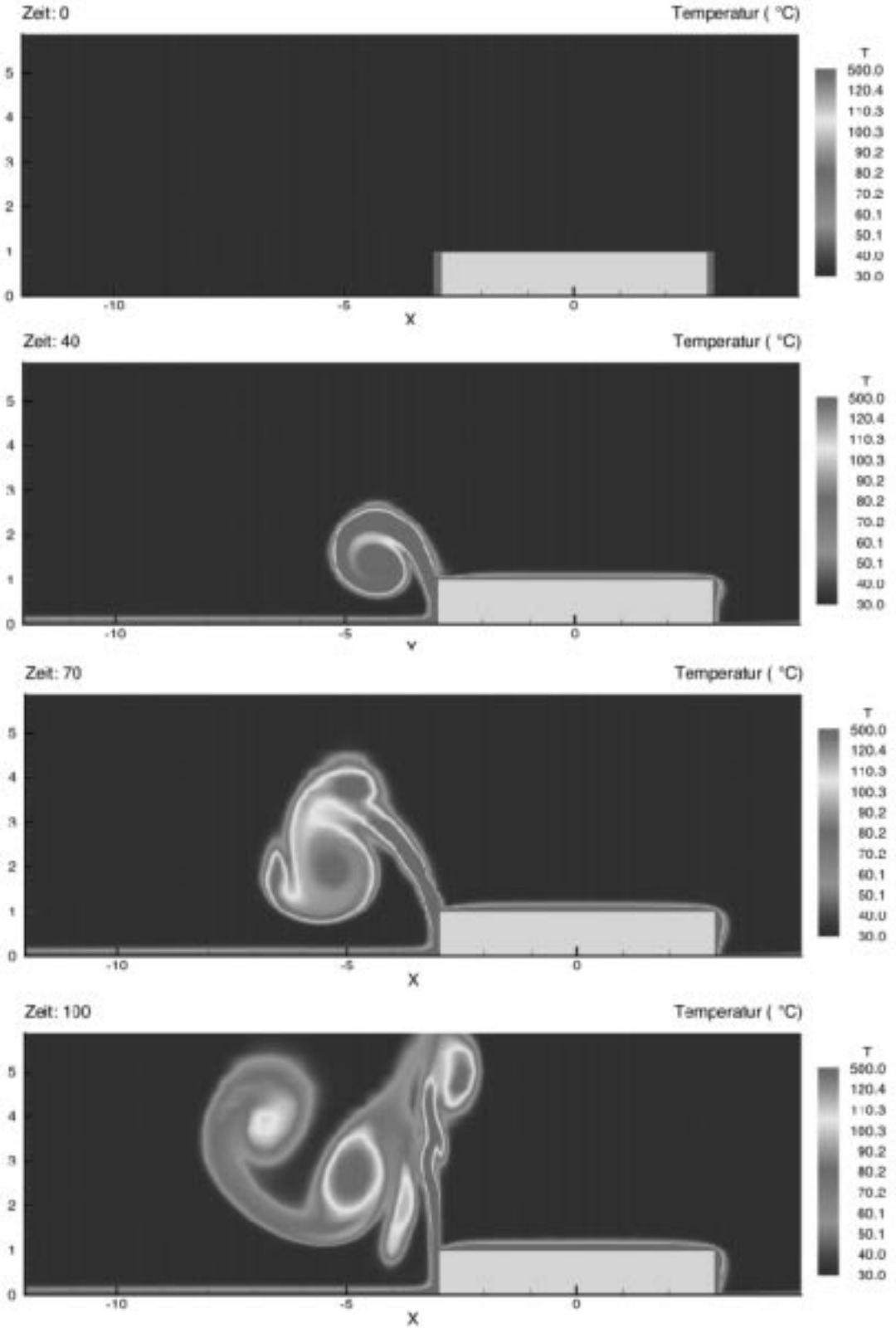

Figure 18 Temporal development of the temperature distribution in the brake-facility.

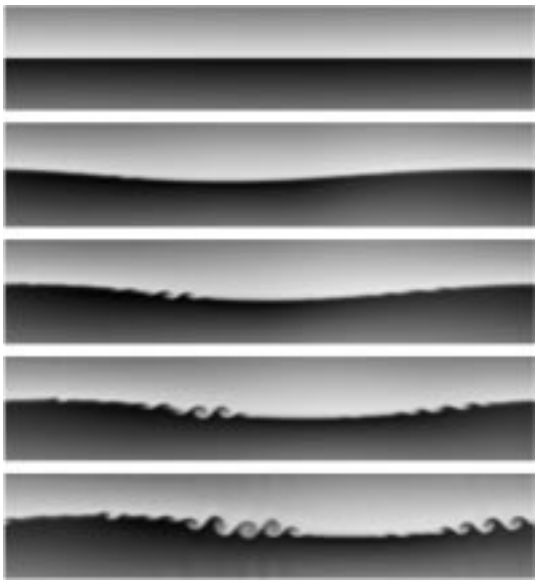

Figure 16. Density at times $t = 0, 6, 9, 11, 14$.

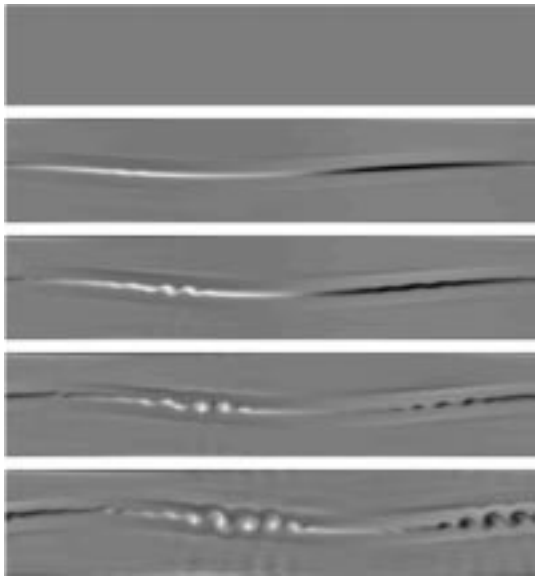

Figure 17. Vorticity at times $t = 0, 6, 9, 11, 14$.

are investigated. For the sake of simplicity the brake block is modeled as a fixed standing rectangular obstacle. The brake disk moves at constant velocity. The starting point is the dimensionless compressible Navier-Stokes equations. With following reference values

$\rho_{\text{ref}} = 1{\cdot}205$ [kg/m^3]

$T_{\text{ref}} = 303{\cdot}15$ [K]

$p_{\text{ref}} = 1{\cdot}0499 \times 10^5$ [N/m^2]

$l_{\text{ref}} = 2 \times 10^{-2}$ [m]

$c_p = 1{\cdot}0006 \times 10^3$ [J/(kg K)]

$\lambda = 2.637 \times 10^{-2}$ [W/(m K)]

$U_{\text{ref}} = 21{\cdot}8$ [m/sec^2]

$\nu(T = 500°C) = 7{\cdot}890 \times 10^{-5}$ [m^2/sec]

$\mu(= \rho_{\text{ref}} \cdot \nu) = 9{\cdot}50 \times 10^{-5}$ [kg/(m sec)],

the three dimensionless numbers, Reynolds-, Prandtl- and Mach number, important for the flow become

$\text{Re} = 5525{\cdot}98$

$\text{Pr} = 3{\cdot}627$

$\text{M} = 0{\cdot}0738.$

The total computing area covers the range from $-18l_{\text{ref}}$ to $18l_{\text{ref}}$ in the x-direction and from $0l_{\text{ref}}$ to $6l_{\text{ref}}$ in the y-direction. The brake block is fixed at the origin and has length $6l_{\text{ref}}$ and

height $1l_{\text{ref}}$. We have used an equidistant grid in the x-direction ($\Delta x = 0.1l_{\text{ref}}$). In the y-direction we adopted a non-equidistant grid ($\Delta y_{\min} = 0 \cdot 03l_{\text{ref}}$) for a better resolution in the boundary layer. For the simulation we assume periodic conditions for all variables at the left and right boundary, outflow conditions at the upper boundary and no-slip conditions at the brake block and brake disk. As initial condition the state at rest is assumed. The temperatures at the brake block and brake disk are given as $500°C$ and at the outflow $30°C$. In Figure 18 the time-development of the hot temperature boundary layer is shown. During the so-called 'stripping-process' of the boundary layer at the brake block a strong left-rotating vortex develops rapidly and interacts with the outer flow. This process transports heat away from the brake disk very efficiently. Behind the brake block cold air is in contact with the hot brake disk and the heat-transport coefficients are large. A new boundary layer forms in this region.

For small brake-disk velocities and low temperatures, the numerical results are similar to those of an incompressible simulation. For higher temperatures (about $500°C$ when braking while driving down a hill or during sudden braking at high velocities) a compressible calculation is necessary. Future work will examine the stability of the boundary layer. By use of the linear stability analysis based on the Orr-Sommerfeld equations appropriate perturbations will be overlaid to the flow field.

4.2.3. *Summary*

The numerical results for the test problems clearly demonstrate that the MPV concept works very well in the incompressible as well as in the low-Mach- number regime. No modifications are necessary for viscous and inviscid fluid flows. The basics are the results of a multi-scale asymptotic analysis and these results are used to motivate a pressure decomposition where every term of the asymptotic series plays a different physical role. The asymptotic equations themselves are only used to obtain estimates which have to be corrected. Therefore, the scheme always solves the full compressible Euler or Navier-Stokes equations and is not restricted to very small Mach numbers, as it would be when solving the asymptotic equations only. The MPV concept proposed may be used to extend any incompressible solver to the low-Mach-number regime.

4.3. A FULLY CONSERVATIVE ZERO-MACH-NUMBER VARIABLE-DENSITY FLOW SOLVER

The conservation laws governing the evolution of a compressible calorically perfect gas are given by (2.1.15). Neglecting viscous effects, chemical reactions and taking into account a gravitational force field, we have these equations:

$$\begin{aligned} \rho_t + \nabla \cdot (\rho \overline{\boldsymbol{v}}) &= 0\,, \\ (\rho \overline{\boldsymbol{v}})_t + \nabla \cdot (\rho \overline{\boldsymbol{v}} \circ \overline{\boldsymbol{v}}) + \frac{1}{\mathrm{M}^2} \nabla p &= \frac{1}{\mathrm{Fr}^2} \rho \overline{\boldsymbol{g}}, \\ (\rho e)_t + \nabla \cdot ((\rho e + p)\boldsymbol{v}) &= \frac{\mathrm{M}^2}{\mathrm{Fr}} \rho \boldsymbol{v} \cdot \overline{\boldsymbol{g}}, \end{aligned} \tag{4.3.1}$$

with the equation of state

$$p = (\gamma - 1)(\rho e - \tfrac{1}{2}\mathrm{M}^2 \rho \boldsymbol{v} \cdot \boldsymbol{v}). \tag{4.3.2}$$

After scaling, the acceleration $\boldsymbol{g}$ is a constant unit vector. All variables are dimensionless and $O(1)$. Beside the Mach number M, a new characteristic number appears in (4.3.1). This is the

Froude number $\mathrm{Fr} := v_{\mathrm{ref}}/\sqrt{g l_{\mathrm{ref}}}$. In the limit of $\mathrm{M} \to 0$, but finite Fr, solutions of (4.3.1) exhibit the singular behavior analyzed in Section 2.1 (see also [2], [46], [6]). Let us stress the issues which are particularly relevant for the computation of numerical approximations of (4.3.1) in the $\mathrm{M} \to 0$ limit:

1. ∇p tends to zero, but $\nabla p/\mathrm{M}^2$ tends to some non-trivial function $\nabla p^{(2)}$.

2. The total energy per unit volume ρe tends to $p/(\gamma - 1)$ and the right-hand side of the energy equation tends to zero. Thus, the energy fluxes $\nabla \cdot ((\rho e + p)\boldsymbol{v})$ must satisfy a constraint for the time derivative of ρe to have zero gradients. This is a constraint for the divergence of the velocity field $\boldsymbol{v}$.

3. Assume this constraint is $\nabla \cdot \boldsymbol{v} = 0$ (this is a special, but important case). Then the first equation of (4.3.1) requires the density ρ to be simply advected along particle paths. Thus, if ρ is constant at the initial time (and density variations are not entering the computational domain through the boundary), it should remain constant at any time.

4. The eigenvalues of the Jacobian of the flux function associated with the homogeneous part of (4.3.1) degenerate: These eigenvalues are $\boldsymbol{v} \cdot \boldsymbol{n}$ and $\boldsymbol{v} \cdot \boldsymbol{n} \pm c/\mathrm{M}$ with $c^2 = \gamma p/\rho$ and $\boldsymbol{n}$ any unit vector.

Due to this singular behavior, when attempting to compute numerical solutions of (4.3.1) for $\mathrm{M} \to 0$, using a standard finite-volume method for compressible flow, one faces at least the following difficulties:

1. A finite arithmetic single variable representation of the pressure p does not allow a meaningful computation of $\nabla p/\mathrm{M}^2$.

2. The energy fluxes do not satisfy the correct divergence constraint. As a consequence the total energy does not tend to $p/(\gamma - 1)$ and has non-zero gradients.

3. The velocity field does not satisfy the correct divergence constraint.

4. The numerical method fails to compute the correct rate of change of density along particle paths. For the special case in which the divergence constraint for the velocity is simply $\nabla \cdot \boldsymbol{v} = 0$, the numerical method fails to preserve an initially constant density distribution.

5. Explicit methods suffer from a Courant-Friedrichs-Lewy [47] time step stability restriction of the kind $\delta t < O(\mathrm{M})$.

The first and the last difficulties can be overcome by replacing (4.3.1) with its asymptotic limit:

$$\begin{aligned}
\rho_t + \nabla \cdot (\rho \overline{\boldsymbol{v}}) &= 0, \\
(\rho \boldsymbol{v})_t + \nabla \cdot (\rho \boldsymbol{v} \circ \boldsymbol{v}) + \nabla p^{(2)} &= \frac{1}{\mathrm{Fr}^2} \rho \boldsymbol{g}, \\
(\rho e)_t + \nabla \cdot ((\rho e + p) \boldsymbol{v}) &= 0, \\
p &= (\gamma - 1) \rho e \,, \\
p &= p^{(0)}(t) \,.
\end{aligned} \tag{4.3.3}$$

Let us comment on the above equations. According to the results discussed in Section 2.1, the pressure field p has been decomposed into a zero-gradient time dependent thermodynamic component $p^{(0)}$ plus a second-order perturbation $\mathrm{M}^2 p^{(2)}$. The thermodynamic pressure $p^{(0)}$ is given by (2.1.38). For $(\gamma - 1)(\rho e)_t$ to be equal to $\mathrm{d}p^{(0)}/\mathrm{d}t$, the energy fluxes through the boundary ∂V of any arbitrary control volume $V \subset \Omega$ must satisfy the following constraint

$$\frac{1}{|V|} \oint_{\partial V} (\rho e + p) \boldsymbol{v} \cdot \boldsymbol{n} \mathrm{d}s = -\frac{1}{\gamma - 1} \frac{\mathrm{d}p^{(0)}}{\mathrm{d}t}. \tag{4.3.4}$$

Since $\rho e + p$ has no variations in space, Equation (4.3.4) is a divergence constraint for the velocity field $\boldsymbol{v}$. It implicitly defines the perturbation pressure $p^{(2)}$: At any time the gradients $\nabla p^{(2)}$ must guarantee that the acceleration $\boldsymbol{v}_t$ has a well-defined spatially-constant time-dependent divergence. We can compute this divergence by taking the time derivative of Equation (4.3.4). In the special case $\mathrm{d}p^{(0)}/\mathrm{d}t = 0$ (closed vessel, periodic boundary conditions, etc.) Equation (4.3.4) becomes the well-known $\nabla \cdot \boldsymbol{v} = 0$ constraint of the 'incompressible' Euler equations and $\nabla p^{(2)}$ a Lagrangian multiplier projecting convective and gravitational accelerations onto the space of divergence-free vector fields.

System (4.3.3) enjoys a time-step stability restriction of the kind $\delta t < O(1)$ and explicitly introduces a two-variable representation of the pressure field which allows a meaningful finite arithmetic computation of pressure gradients in the $M = 0$ limit. Notice that, because of the implicitness of $p^{(2)}$, (4.3.3) is *not* a hyperbolic system. Our aim is to solve (4.3.3) numerically by means of a finite-volume method in conservation form:

$$\mathbf{U}_V^{n+1} = \mathbf{U}_V^n - \frac{\delta t}{|V|} \sum_{I \in \mathcal{I}_{\partial V}} |I| \mathbf{F}_I + \delta t \mathbf{W}_V \qquad \forall\, V \in \mathcal{V}. \tag{4.3.5}$$

Here $V \in \mathcal{V}$ is a cell of a conformal space discretization of the flow domain Ω and $|V|$ is the volume of V. $I \in \mathcal{I}$ is an interface between two adjacent cells and $|I|$ is the area of I. By $\mathcal{V}$, $\mathcal{I}$ we denote the set of all cells and of all interfaces, respectively. $\mathcal{I}_{\partial V} \subset \mathcal{I}$ represents the set of those interfaces which lay on the boundary ∂V of V. $\mathbf{U}_V^n$ is a numerical approximation to the average $\mathbf{u}_V^n$ of the solution $\mathbf{u}$ of (4.3.3) over the cell V at time t^n. $\mathbf{F}_I$ and $\mathbf{W}_V$ are numerical approximations to the averages $\mathbf{f}_I$ and $\mathbf{w}_V$ of the flux function $\mathbf{f}$ and of the right-hand side $\mathbf{w}$ of (4.3.3). These averages are taken over the time interval $[t^n, t^{n+1} := t^n + \delta t]$ and over the interface I and the cell V for $\mathbf{f}_I$ and $\mathbf{w}_V$, respectively:

$$\mathbf{u} := \begin{pmatrix} \rho \\ \rho \boldsymbol{v} \\ \rho e \end{pmatrix}, \qquad \mathrm{f} := \begin{pmatrix} \rho \boldsymbol{v} \cdot \boldsymbol{n} \\ \boldsymbol{v} \rho \boldsymbol{v} \cdot \boldsymbol{n} + p^{(2)} \boldsymbol{n} \\ h \rho \boldsymbol{v} \cdot \boldsymbol{n} \end{pmatrix}, \qquad \mathbf{w} := \begin{pmatrix} 0 \\ \rho \boldsymbol{g} / \mathrm{Fr}^2 \\ 0 \end{pmatrix}.$$

In the above expressions h is the enthalpy per unit mass of the gas: $\rho h := \rho e + p$. Let us focus the attention on the numerical flux $\mathbf{F}_I$:

$$\mathbf{F}_I := \mathbf{f}(\mathbf{U}_I, \boldsymbol{n}_I) = \begin{pmatrix} (\rho\overline{\boldsymbol{v}})_I \cdot \boldsymbol{n}_I \\ \boldsymbol{v}_I(\rho\boldsymbol{v})_I \cdot \boldsymbol{n}_I \\ h_I(\rho\boldsymbol{v})_I \cdot \boldsymbol{n}_I \end{pmatrix} + \begin{pmatrix} 0 \\ p_I^{(2)}\boldsymbol{n}_I \\ 0 \end{pmatrix} . \tag{4.3.6}$$

We want to construct numerical fluxes $\mathbf{F}_I$ or, equivalently, interface averages $\mathbf{U}_I$, that fulfill the following requirements:

1. On smooth solutions $\mathbf{F}_I$ approximates the average flux $\mathbf{f}_I$ up to errors of order $O(\delta t^2)$.

2. The energy fluxes satisfy the divergence constraint

$$\frac{1}{|V|} \sum_{I \in \mathcal{I}_{\partial V}} |I| h_I (\rho\boldsymbol{v})_I \cdot \boldsymbol{n}_I = -\frac{1}{\gamma - 1} \frac{p_V^{(0),n+1} - p_V^{(0),n}}{\delta t}, \qquad \forall\, V \in \mathcal{V} . \tag{4.3.7}$$

   This is a discrete form of the divergence constraint (4.3.4) which is consistent with the finite-volume method (4.3.5).

3. The mass fluxes guarantee the correct rate of change of density along particle paths. Notice that, in the special case $\mathrm{d}p^{(0)}/\mathrm{d}t = 0$, this can be achieved if (and only if) the interface velocities $\boldsymbol{v}_I$ which are responsible for the advection of the density are divergence-free in the sense that

$$\frac{1}{|V|} \sum_{I \in \mathcal{I}}^{\partial V} |I|\, \boldsymbol{v}_I \cdot \boldsymbol{n}_I = 0 .$$

4. The discrete velocity field $\boldsymbol{v}_{\mathcal{V}}^{n+1}$ satisfies some discrete form of the divergence constraint (4.3.4).

In the next subsection we describe how to construct numerical fluxes which fulfill the requirements listed above. This is done via a semi-implicit procedure. First, we compute an explicit approximation to the fluxes of an auxiliary hyperbolic system. In our implementation this is done in a predictor stage in which the influence of pressure gradients on the convective fluxes is neglected over a half time step. Secondly, a Poisson-type equation for cell-centered pressures $p_{\mathcal{V}}^{(2)}$ is solved. These pressures allow the computation of convective fluxes of mass and energy that fulfill requirement 1) to 3) and the update of density and total energy cell averages. At this point the grid-cell interface pressure-induced momentum fluxes $p_I^{(2)}\boldsymbol{n}_I$ are yet unknown. This pressure is obtained by solving another suitable discrete form of the energy conservation law. This yields a second elliptic problem. The solution of this problem leads to a new cell-centered velocity field $\boldsymbol{v}_{\mathcal{V}}^{n+1}$ which *exactly* satisfies a discrete divergence constraint that is consistent with energy conservation. For a detailed description of the flux construction algorithm and of the discrete operators involved in such construction we refer to [7]. In Section 4.3.2 we discuss some numerical results.

4.3.1. *Semi-implicit construction of numerical fluxes*

The auxiliary system

$$\begin{aligned} \rho_t + \nabla \cdot (\rho \overline{\boldsymbol{v}}) &= 0\,, \\ (\rho \boldsymbol{v})_t + \nabla \cdot (\rho \boldsymbol{v} \circ \boldsymbol{v}) + \nabla p &= \frac{1}{\mathrm{Fr}^2} \rho \boldsymbol{g}\,, \\ (\rho e)_t + \nabla \cdot ((\rho e + p^{(0)}) \boldsymbol{v}) &= 0\,, \end{aligned} \tag{4.3.8}$$

with equation of state

$$p = (\gamma - 1)\rho e \tag{4.3.9}$$

and flux function

$$\mathbf{f}^* := \begin{pmatrix} & \rho \boldsymbol{v} \cdot \boldsymbol{n} \\ \boldsymbol{v} & \rho \boldsymbol{v} \cdot \boldsymbol{n} + p \boldsymbol{n} \\ h^{(0)} & \rho \boldsymbol{v} \cdot \boldsymbol{n} \end{pmatrix}, \qquad \rho h^{(0)} := \rho e + p^{(0)}$$

enjoys the following properties:

1. The system has the same convective fluxes as the zero-Mach-number governing equations (4.3.3).

2. The system is hyperbolic.

3. The eigenvalues of the Jacobian of the flux function $\mathbf{f}^*$ are $\boldsymbol{v} \cdot \boldsymbol{n}$ and $\boldsymbol{v} \cdot \boldsymbol{n} \pm c$ with $c^2 := (\gamma - 1)h^{(0)}$ (see [6]).

4. Solutions of (4.3.8) satisfy, for homogeneous pressure p and zero flow divergence at time $t = 0$, the following estimates at time $t > 0$ (see [7]):

$$\nabla \cdot \boldsymbol{v} = O(t), \qquad \nabla p = O(t^2).$$

Let $\mathbf{F}^*_{\mathit{1}}$ be numerical fluxes obtained with an explicit high-resolution upwind method for the auxiliary system (4.3.8). In our implementation, for instance, the method is a MUSCL scheme (see [48], [49], [50], [51], [52]) based on slope limiting of characteristic variables and the numerical flux proposed by Einfeldt [53] which has been extended for system (4.3.8) according to the characteristic analysis presented in [6].

Due to the first and the last of the above items, the difference between the rate of change of the conserved variables $\mathbf{u}$ as given by (4.3.3) and the rate of change of $\mathbf{u}$ in the auxiliary system (4.3.8) is, over short times t and up to terms $O(t^2)$:

$$\mathbf{u}_t|_{(4.3.3)} - \mathbf{u}_t|_{(4.3.8)} = - \begin{pmatrix} 0 \\ \nabla p^{(2)} \\ 0 \end{pmatrix}. \tag{4.3.10}$$

On each interface $I \in \mathcal{I}$ the numerical flux $\mathbf{F}_I$ can therefore be obtained from the auxiliary numerical flux $\mathbf{F}_I^*$ by correcting the interface average momenta $(\rho \boldsymbol{v})_I$ and velocities $(\boldsymbol{v})_I$ as follows:

$$(\rho \boldsymbol{v})_I = (\rho \boldsymbol{v})_I^* - \frac{\delta t}{2} (\nabla p^{(2)})_I , \tag{4.3.11}$$

$$(\boldsymbol{v})_I = (\boldsymbol{v})_I^* - \frac{\delta t}{2} \frac{1}{\rho_I} (\nabla p^{(2)})_I . \tag{4.3.12}$$

The term $(\nabla p^{(2)})_I$ represents the interface average gradients of the unknown pressure $p^{(2)}$. Let us approximate $p^{(2)}$ with a piecewise linear function between cell-centered values $p_{\mathcal{V}}^{(2)}$. Inserting (4.3.11) into the discrete divergence constraint (4.3.7), one obtains a discrete Poisson-type problem for the cell-centered values $p_{\mathcal{V}}^{(2)}$. The associated discrete Laplace operator has an enthalpy-weighted five points (in two space dimensions) compact stencil.

Once $(\rho \boldsymbol{v})_I$, $(\boldsymbol{v})_I$ have been computed ($\rho_I = \rho_I^*$ and $h_I = h_I^*$ because no correction in density or energy is needed, see (4.3.10)) the convective part of $\mathbf{F}_I$ is known and one can update both density and energy. Notice that, per construction

$$\begin{aligned} (\rho e)_V^{n+1} &= (\rho e)_V^n - \delta t \frac{1}{|V|} \sum_{I \in \mathcal{I}_{\partial V}} |I| h_I (\rho \boldsymbol{v})_I \cdot \boldsymbol{n}_I \\ &= (\rho e)_V^n + \delta t \frac{1}{\gamma - 1} \frac{p_V^{(0),n+1} - p_V^{(0),n}}{\delta t} = \frac{1}{\gamma - 1} p_V^{(0),n+1} . \end{aligned} \tag{4.3.13}$$

For the computation of $(\rho \boldsymbol{v})_{\mathcal{V}}^{n+1}$, however, we still need the pressure component of the momentum flux $p^{(2)} \boldsymbol{n}$ at the interfaces. This is the last term of the numerical flux (4.3.6). This pressure is computed by imposing requirement number 4), *i.e.*, the discrete velocity field $\boldsymbol{v}_{\mathcal{V}}^{n+1}$ shall satisfy some discrete form of the divergence constraint (4.3.4). Let $(\rho \boldsymbol{v})_{\mathcal{V}}^{**}$ be the intermediate cell averages

$$(\rho \boldsymbol{v})_V^{**} := (\rho \boldsymbol{v})_V^n - \frac{\delta t}{|V|} \sum_{I \in \mathcal{I}_{\partial V}} |I| \boldsymbol{v}_I (\rho \boldsymbol{v})_I \cdot \boldsymbol{n}_I + \delta t \frac{\rho \boldsymbol{g}}{\mathrm{Fr}^2}, \qquad \forall\, V \in \mathcal{V} . \tag{4.3.14}$$

The finite-volume method (4.3.5) for the final cell averages $(\rho \boldsymbol{v})_{\mathcal{V}}^{n+1}$ can be expressed in terms of $(\rho \boldsymbol{v})_{\mathcal{V}}^{**}$ and of the unknown interface pressures $p_{\mathcal{I}}^{(2)}$ as:

$$(\rho \boldsymbol{v})_V^{n+1} = (\rho \boldsymbol{v})_V^{**} - \frac{\delta t}{|V|} \sum_{I \in \mathcal{I}_{\partial V}} |I| \, p_I^{(2)} \boldsymbol{n}_I, \qquad \forall\, V \in \mathcal{V} . \tag{4.3.15}$$

Let $\overline{\mathcal{V}}$ be a *dual* discretization of Ω. $\overline{\mathcal{V}}$ consists of control volumes $\overline{V}$ centered around the nodes of the original grid. The interfaces between the cells of $\overline{\mathcal{V}}$ are denoted by $\overline{I}$. As usual $\overline{\mathcal{I}}$ is the set of all such interfaces.

In Figure 19 a cell-centered and a node-centered control volume, V and $\overline{V}$, are drawn for a two-dimensional Cartesian grid. We compute $p_{\mathcal{I}}^{(2)}$ by linear interpolation on the set of nodal values $p_{\overline{\mathcal{V}}}^{(2)}$. These nodal values are computed following an idea originally proposed by Geratz [54]. Consider a second-order finite-volume method for the total energy ρe on the dual discretization:

$$(\rho e)_{\overline{V}}^{n+1} := (\rho e)_{\overline{V}}^n - \frac{\delta t}{|\overline{V}|} \sum_{\overline{I} \in \overline{\mathcal{I}}_{\partial \overline{V}}} \frac{|\overline{I}|}{2} \left((\rho h \boldsymbol{v})_{\overline{I}}^n + (\rho h \boldsymbol{v})_{\overline{I}}^{n+1} \right) \cdot \boldsymbol{n}_{\overline{I}}, \qquad \forall\, \overline{V} \in \overline{\mathcal{V}} \tag{4.3.16}$$

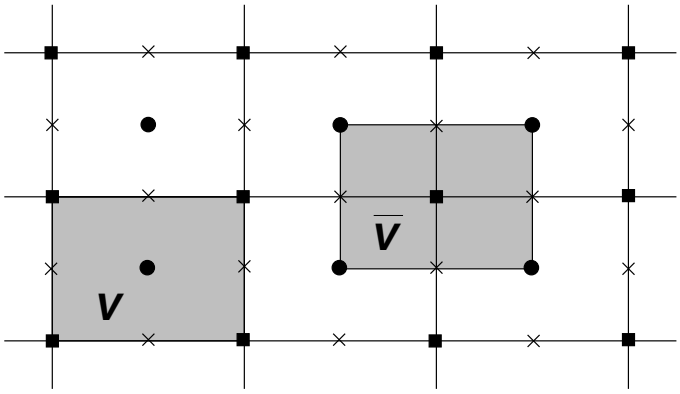

Figure 19 Cell (V) and node centered ($\overline{V}$) control volumes; cell centers, nodes and the midpoints of the interfaces are marked by circles, squares and crosses, respectively

and require the energy fluxes through the interfaces of the dual discretization to satisfy the divergence constraint

$$\frac{\delta t}{|\overline{V}|}\sum_{\overline{I}\in\overline{\mathcal{I}}_{\partial\overline{V}}}\frac{|\overline{I}|}{2}\left((\rho h\boldsymbol{v})_{\overline{I}}^{n}+(\rho h\boldsymbol{v})_{\overline{I}}^{n+1}\right)\cdot\boldsymbol{n}_{\overline{I}}=-\frac{1}{\gamma-1}\frac{p_{\overline{V}}^{(0),n+1}-p_{\overline{V}}^{(0),n}}{\delta t},\qquad\forall\,\overline{V}\in\overline{\mathcal{V}}\,. \tag{4.3.17}$$

Equation (4.3.17) is a discrete form of the divergence constraint (4.3.4) which is consistent with the finite-volume method (4.3.16). $p^{(0),n+1}$ is the same as was computed and used in the first projection step. The dual interface averages can be expressed to the desired-order accuracy by means of cell averages:

$$(\rho h\boldsymbol{v})_{\overline{\mathcal{I}}}^{(\cdot)}=L_{\overline{\mathcal{I}}}^{\mathcal{V}}\left((\rho h\boldsymbol{v})_{\mathcal{V}}^{(\cdot)}\right)\,. \tag{4.3.18}$$

$L_{\overline{\mathcal{I}}}^{\mathcal{V}}$ is a (linear) operator mapping cell averages into interface averages. Together with (4.3.15) and (4.3.18), Equation (4.3.17) defines a discrete Poisson-type problem for the nodal values $p_{\overline{\mathcal{V}}}^{(2)}$. This problem is the equivalent of (4.3.7), (4.3.11) on the dual grid. Its associated discrete Laplace operator has an enthalpy-weighted nine points (in two space dimensions) compact stencil. In the special case $\mathrm{d}p^{(0)}/\mathrm{d}t = 0$ the nodal values $p_{\overline{\mathcal{V}}}^{(2)}$ guarantee that the discrete velocity field $\boldsymbol{v}_{\mathcal{V}}^{n+1}$ satisfies the divergence constraint

$$\frac{1}{|\overline{V}|}\sum_{\overline{I}\in\overline{\mathcal{I}}_{\partial\overline{V}}}|\overline{I}|L_{\overline{I}}^{\mathcal{V}}(\boldsymbol{v}_{\mathcal{V}}^{n})\cdot\boldsymbol{n}_{\overline{I}}=0\quad\Rightarrow\quad\frac{1}{|\overline{V}|}\sum_{\overline{I}\in\overline{\mathcal{I}}_{\partial\overline{V}}}|\overline{I}|L_{\overline{I}}^{\mathcal{V}}(\boldsymbol{v}_{\mathcal{V}}^{n+1})\cdot\boldsymbol{n}_{\overline{I}}=0\,. \tag{4.3.19}$$

We have fulfilled requirements 1) – 4) and the construction of the numerical fluxes $\mathbf{F}_I$ is completed.

4.3.2. *Numerical results*

We discuss the numerical results obtained on five test problems. The first four problems are chosen to assess the accuracy and the efficiency of the method and test its capability to cope with large density variations and small-scale gravity-driven flows. For these tests either the exact solution or at least some properties of the exact solution are known. This allows a

meaningful validation of the method and provides a flavor of the difficulties that must be faced in the numerical simulation of more realistic flows. Problem number five is included to show that the proposed numerical method can be extended to cope with boundary-driven compression/expansion, viscous forces and heat transfer. All test problems can be run with trivial geometries and boundary conditions.

The computations have been performed on regular Cartesian grids. The discrete operators and the linear systems for the cell-centered and for the node-centered pressures are those explicitly given in [7]. These two linear systems must be solved at each time step. This has been done by means of a multi-grid preconditioned conjugate-gradient method. The difference with respect to the standard conjugate-gradient solver is that, in each iteration, the new residual vector is computed by applying a multi-grid cycle to the previous residual vector. There are several ways of visiting the grid levels during the multi-grid procedure, such as a V-cycle, W-cycle, F-cycle [55] and nested cycle. In our case, the F-cycle turned out to provide the best contraction rate. As smoother a Gauss-Seidel method was used with two pre- and post- smoothing steps on each grid level. In two space dimensions a standard nine-point prolongation operator was used. This operator is defined through bilinear interpolation. In three dimensions trilinear interpolation provides a 27-point prolongation operator. The adjoint prolongation operator served as restriction operator. In the presence of large density variations, the coefficients of both linear systems can change by orders of magnitude. In this case the linear coarse-grid operators need to be constructed by Galerkin's approximation [55].

As expected, the computations show that the CPU time needed to solve the systems depends linearly on the number of unknowns. The solution of the linear systems accounts for about 95% of the time required for a computation and demands a memory allocation of roughly one K-byte per computational point. In each solution the residuals

$$r_2(p_{\mathcal{V}}^{(2)}) := \left\| D_{\mathcal{V}}^{\mathcal{I}} \left((\rho h^0 \boldsymbol{v})_{\mathcal{I}}^* \right) - \frac{\delta t}{2} D_{\mathcal{V}}^{\mathcal{I}} \left(h_{\mathcal{I}}^{0,*} G_{\mathcal{I}}^{\mathcal{V}} \left(p_{\mathcal{V}}^{(2)} \right) \right) \right\|_2,$$

$$r_2(p_{\overline{\mathcal{V}}}^{(2)}) := \left\| D_{\overline{\mathcal{V}}}^{\mathcal{V}} \left(h_{\mathcal{V}}^{n+1} (\rho \boldsymbol{v})_{\mathcal{V}}^{**} \right) + D_{\overline{\mathcal{V}}}^{\mathcal{V}} \left((\rho h \boldsymbol{v})_{\mathcal{V}}^n \right) - \delta t D_{\overline{\mathcal{V}}}^{\mathcal{V}} \left(h_{\mathcal{V}}^{n+1} G_{\mathcal{V}}^{\overline{\mathcal{V}}} \left(p_{\overline{\mathcal{V}}}^{(2)} \right) \right) \right\|_2$$

have been driven down to 10^{-7}. In the above definitions $\|a_{\mathcal{V}}\|_2$ represents the Euclidean norm of a vector whose components are the values $a_{\mathcal{V}}$, *i.e.*,

$$\|a_{\mathcal{V}}\|_2 := \left(\sum_{V \in \mathcal{V}} a_V^2 \right)^{1/2}$$

and similarly for $\|a_{\overline{\mathcal{V}}}\|_2$.

Convergence studies. This test problem was originally proposed in Almgren *et al.* [56]. It has been designed to assess the accuracy of the method on constant-density flows. For any time t and $0 < x < 1$, $0 < y < 1$, the velocity field

$$u(x, y, t) := 1 - 2\cos(2\pi(x - t))\sin(2\pi(y - t)),$$

$$v(x, y, t) := 1 + 2\sin(2\pi(x - t))\cos(2\pi(y - t)),$$

together with the pressure $p^{(2)}(x, y, t)$

$$p^{(2)}(x, y, t) := -\cos(4\pi(x - t)) - \cos(4\pi(y - t))$$

Table 1. Constant density: errors and convergence rates in the 2-norm and in the maximum norm.

	32×32	Rate	64×64	Rate	128×128
2-norm	0·193646	2·07	0·0458949	2·10	0·010705
max-norm	0·236456	2·09	0·0553504	2·11	0·012821

is an exact solution of the zero-Mach-number governing equations (4.3.3) with constant pressure $p(x, y, t)$, constant density $\rho(x, y, t)$ and periodic boundary conditions on the unit square. Starting from $t = 0$, we have computed numerical approximations $u^N_{i,j}$ to the cell-averages $u(x_i, y_j, t^N)$ of the exact velocity u at time $t^N = 3$. Similarly $v^N_{i,j}$, $\rho^N_{i,j}$ are numerical approximations to the cell-averages $v(x_i, y_j, t^N)$ and $\rho(x_i, y_j, t^N)$ of the exact v, ρ at time $t^N = 3$.

Three equally spaced regular Cartesian grids of spacings $h = 1/32$, $h = 1/64$ and $h = 1/128$ have been used on the unit square. On each grid the time step was chosen according to a fixed Courant number of 0·8. The initial cell averages $(\rho \boldsymbol{v})^0_{i,j}$ have been computed for $\boldsymbol{v}^0_{i,j}$ to be discretely divergence free

$$(\rho \boldsymbol{v})^0_{i,j} = (\rho \boldsymbol{v})(x_i, y_j, 0) - G^{\overline{\nu}}_{i,j}\left(p^{(2),0}_{\overline{\nu}}\right),$$

i.e., the initial pressure $p^{(2),0}_{\overline{\nu}}$ is a solution of the Poisson problem

$$D^{\nu}_{\overline{\nu}}\left(\frac{1}{\rho^0_{i,j}} G^{\overline{\nu}}_{i,j}\left(p^{(2),0}_{\overline{\nu}}\right)\right) = D^{\nu}_{\overline{\nu}}\left(\frac{(\rho \boldsymbol{v})(x_i, y_j, 0)}{\rho^0_{i,j}}\right)$$

with $\rho^0_{i,j} = \rho(x_i, y_j, 0) = 1$. In the MUSCL scheme for the computation of the auxiliary numerical fluxes $\mathbf{F}^*_{\boldsymbol{1}}$ unlimited slopes have been used. For each grid we have measured the 2-norm e_2 and the maximum norm e_∞ of the cell-error $e_{i,j}$ at time $t^N = 3$:

$$e_{i,j} := \left|\rho(x_i, y_j, t^N) - \rho^N_{i,j}\right| + \left|u(x_i, y_j, t^N) - u^N_{i,j}\right| + \left|v(x_i, y_j, t^N) - v^N_{i,j}\right|,$$

$$e_2 := \left(\sum_{i,j} \left(e_{i,j} h\right)^2\right)^{1/2}, \quad e_\infty := \max_{i,j}\left\{e_{i,j}\right\}.$$

Notice that this is essentially a measure of the velocity error: due to the exact projection of the interface velocity, the density error in the 2-norm is of the same order as $r_2(p^{(2)}_{\mathcal{V}})$, *i.e.*, 10^{-7}. Table 1 shows e_2, e_∞ on the three grids, together with the corresponding convergence rates. These have been computed as follows: Given, *e.g.*, coarse and fine grid 2-norm errors $e_{2,c}$, $e_{2,f}$ and the corresponding grid spacings h_c, h_f the convergence rate is

$$\frac{\log(e_{2,c}/e_{2,f})}{\log(h_c/h_f)}.$$

We have constructed the exact velocity field (4.3.2) by differentiating the streamline function

Table 2. Variable density: errors and convergence rates in the 2-norm and in the maximum norm.

	32×32	Rate	64×64	Rate	128×128
2-norm	0·229332	2·02	0·0563924	2·16	0·0125899
max-norm	0·263492	1·98	0·0664518	1·68	0·0207160

$$\phi(x, y, t) := y - x + \frac{1}{\pi}\cos(2\pi(x-t))\cos(2\pi(y-t))$$

and taking $u := \partial\phi/\partial y$, $v := -\partial\phi/\partial x$. The function ϕ represents a vortical motion $\varphi := \phi - y + x$ superimposed on a translation. The vortical motion is simply advected by the velocity field $\boldsymbol{v}$, *i.e.*,

$$\frac{\mathrm{D}\varphi}{\mathrm{D}t} := \frac{\partial\varphi}{\partial t} + \boldsymbol{v}\cdot\nabla\varphi = 0\,,$$

as one can verify by inspection. Thus, variable-density exact solutions to the governing equations (4.3.3) can be constructed if we take

$$\rho(x, y, t) := f(\varphi)$$

with some smooth function f. We used

$$f(\varphi) := 2 + (\pi\varphi)^2\,. \tag{4.3.20}$$

The constant on the right-hand side is taken to avoid negative densities. The square ensures that densities monotonically increase from the center to the outer boundary of each vortex: a density distribution with local maxima in vortex cores would undergo Rayleigh-Taylor instability. With (4.3.20) an exact solution for the density of (4.3.3) is

$$\rho(x, y, t) := 2 + 0{\cdot}5\cos^2(2\pi(x-t))\cos^2(2\pi(y-t)).$$

In Table 2 the error norms for the variable-density computations are shown. As for the constant-density case we obtain second-order accuracy both in the 2-norm and in the maximum norm.

Advection of a vortex. We consider the advection of a vortex in a channel. The computational domain is the rectangle $[0, 4] \times [0, 1]$. The upper and lower boundaries are walls; periodic boundary conditions are imposed at the left and right boundaries. The grid consists of 80×20 cells. The initial condition is:

$$\rho(x, y, 0) = 1, \qquad u(x, y, 0) = 1 - v_\theta(r)\sin\theta,$$
$$p(x, y, 0) = 1, \qquad v(x, y, 0) = v_\theta(r)\cos\theta$$

with

$$v_\theta(r) = \begin{cases} r/0{\cdot}2 & \text{if } 0 < r < 0.2 \\ 2 - r/0{\cdot}2 & \text{if } R < r < 0.4 \\ 0 & \text{if } r > 0{\cdot}4 \end{cases} \quad \text{and} \quad r = \sqrt{(x-0{\cdot}5)^2 + (y-0{\cdot}5)^2}$$

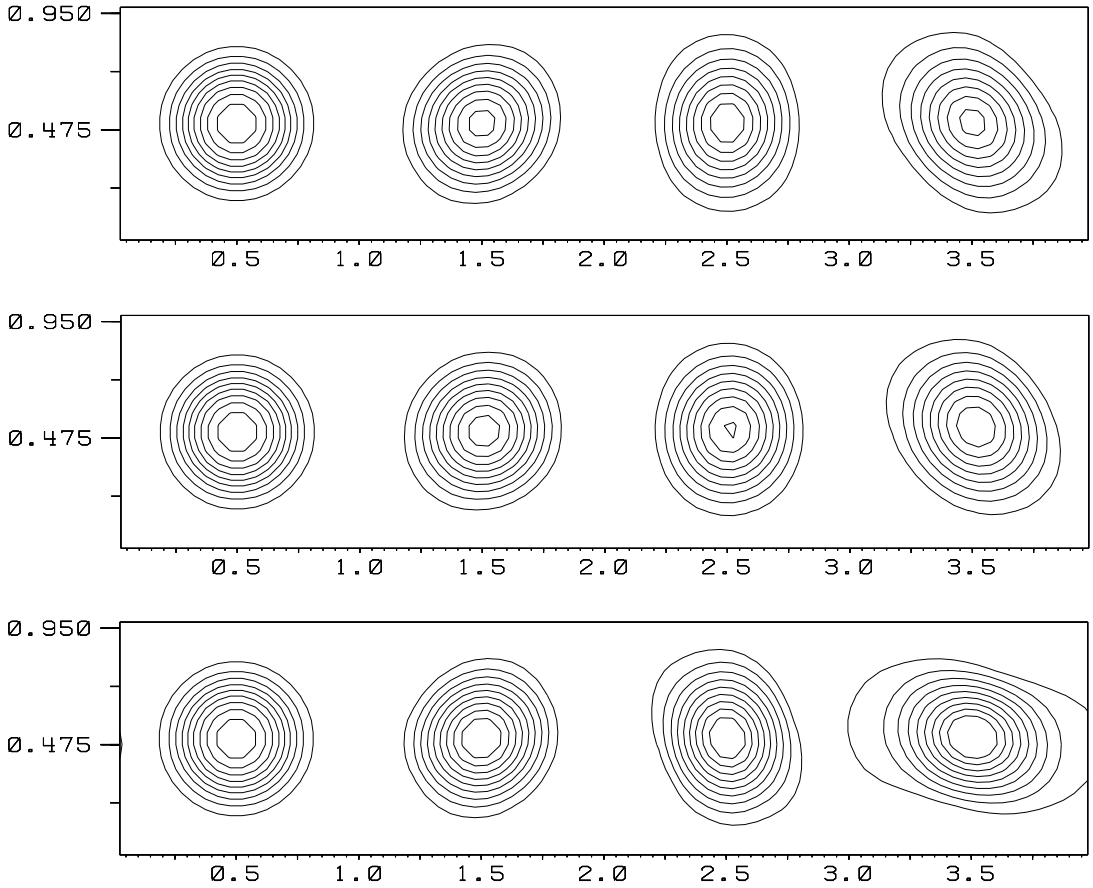

Figure 20. Advection of a vortex at times t =0·0, 1·0, 2·0, 3·0: 9 contour lines of the stream-function in [0·02,0·18]. Unlimited slopes (top), monotonized central-difference (middle) and Sweby's limiter with $k := 1{\cdot}8$ (bottom).

For the above initial data the exact velocity for $t > 0$ can be computed: $u(x, y, t) = u(x - u_\infty t, y, 0)$ and $v(x, y, t) = v(x - u_\infty t, y, 0)$, *i.e.*, the initial data are simply advected by the background velocity u_∞. This problem was originally proposed by Gresho *et al.* [57].

In Figure 20 we show contour lines of the stream function for three computations. They have been done using different slope limiters in the MUSCL step of the Godunov-type method for the computation of the auxiliary fluxes. Due to the rough discretization the results exhibit a significant deformation of the vortex. In contrast to the results shown in [57] Figure 13, however, the core of the vortex is advected along the axis of the channel in agreement with the exact solution. The first computation (unlimited slopes) shows a loss of vorticity comparable with [57] by exhibiting a stronger deformation of the vortex. The second and the third computations (monotonized central-difference and Sweby's limiter with $k := 1{\cdot}8$, see, *e.g.*, Schulz-Rinne [58]) show a slightly stronger deformation of the initial vorticity distribution, but a much better conservation of the maximum level of vorticity.

Driven cavity flows. The driven-cavity test problems proposed in [59] have been the subject of many numerical computations (see, *e.g.*, [60], [61]), and the Section 4.2 above. For Reynolds numbers (Re) up to 1000 most computations seem to converge towards a steady state and

there is an excellent agreement between stationary solutions obtained with different numerical schemes. Thus, these problems are very well suited to validate new numerical methods. Here driven cavity flows at Reynolds numbers 100 and 1000 have been computed. Our main goals are:

- Show that the method can be easily extended to cope with viscous flows;
- Investigate the behavior of the method with respect to the coupling between pressure and velocity fields;
- Investigate the behavior of the method with respect to convergence towards stationary solutions;
- Compare our numerical results with established reference solutions.

In agreement with [59], we consider a viscous zero-Mach-number flow with no heat conduction. Viscous effects only enter in the momentum equation through a viscous stress and are accounted for via operator-splitting techniques. A delicate issue in the numerical computation of incompressible flows is that of the coupling between pressure and velocity fields. For finite discretizations this problem (often referred to as 'local grid decoupling' or 'checkerboard instability') can be described as follows. Assume that the null space of the discrete gradient operator, $\ker(G_{\mathcal{V}}^{\overline{\mathcal{V}}})$, contains highly oscillating fields. Since $G_{\mathcal{V}}^{\overline{\mathcal{V}}}$ has a local stencil, this is usually the case whenever $\dim(\ker(G_{\mathcal{V}}^{\overline{\mathcal{V}}})) > 1$. If the solution $p_{\overline{\mathcal{V}}}$ of the Poisson-type problem has components in $\ker(G_{\mathcal{V}}^{\overline{\mathcal{V}}})$, one obtains pressure oscillations which do not influence the velocity field: pressure and velocity field decouple.

For two-dimensional equally spaced Cartesian grids and the implementation described in [7] one finds that $\dim(\ker(G_{\mathcal{V}}^{\overline{\mathcal{V}}})) = 2$ and $\ker(G_{\mathcal{V}}^{\overline{\mathcal{V}}})$ contains, besides constant pressures $p_{\overline{\mathcal{V}}}^{c}$, a non-trivial highly oscillating mode $p_{\overline{\mathcal{V}}}^{o}$. Therefore, we expect to observe pressure-velocity decoupling whenever the iterative linear system solver converges towards solutions $p_{\overline{\mathcal{V}}}$ with components in $\ker(G_{\mathcal{V}}^{\overline{\mathcal{V}}})$. The method of conjugate gradients preserves, by exact arithmetics, the components of $p_{\overline{\mathcal{V}}}^{k}$ in $\ker(G_{\mathcal{V}}^{\overline{\mathcal{V}}})$. Since we always start our iteration with $p_{\overline{\mathcal{V}}}^{0} := 0$ we expect a numerical solution obtained in a reasonable number of iteration steps to be oscillation free. This is confirmed by our numerical results. On the other hand, numerical solutions obtained through a random choice of $p_{\overline{\mathcal{V}}}^{0}$ may exhibit pressure-velocity decoupling.

The understanding of the pressure-velocity decoupling in the limit of vanishing grid size requires a deeper analysis. We have investigated numerically the effects 1) of grid refinement at constant convection-based Courant number CFL of 0·8 and 2) of time-step refinement for a fixed grid size. Some results are shown in Figures 21 and 22. Neither in the first nor in the second case do we observe the onset of pressure-velocity decoupling. Figure 23 shows the time history of the residual

$$r_2^n := \sum_{\mathcal{V} \in V} h^2 \|\mathbf{U}_{\mathcal{V}}^n - \mathbf{U}_{\mathcal{V}}^{n-1}|\|_2$$

for a $\mathrm{Re} = 1000$ computation on several grids. The residual is plotted versus the number of computational steps. The cost of a single step on a 64×64 grid is of about 1·3 seconds on a DEC Alpha 21164 CPU running at 500 MHz. For the 128×128 grid-cells computation pres-

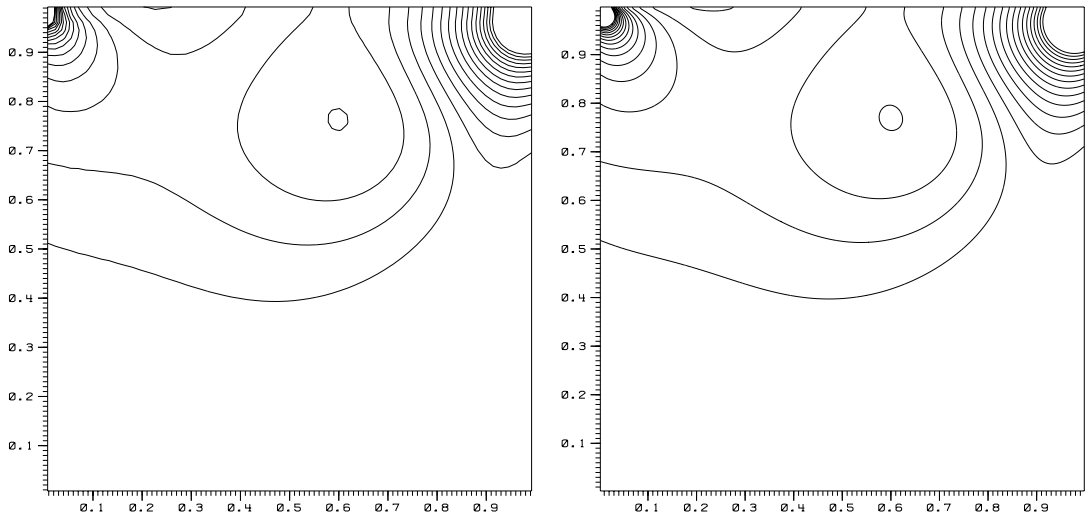

Figure 21. Driven cavity at Re= 100, C =0·8: 30 contour lines of the nodal pressure $p_{\mathcal{V}}^{(2)}$ in [−0·4,0·4]. 64 × 64 (left) and 256 × 256 (right) grid cells.

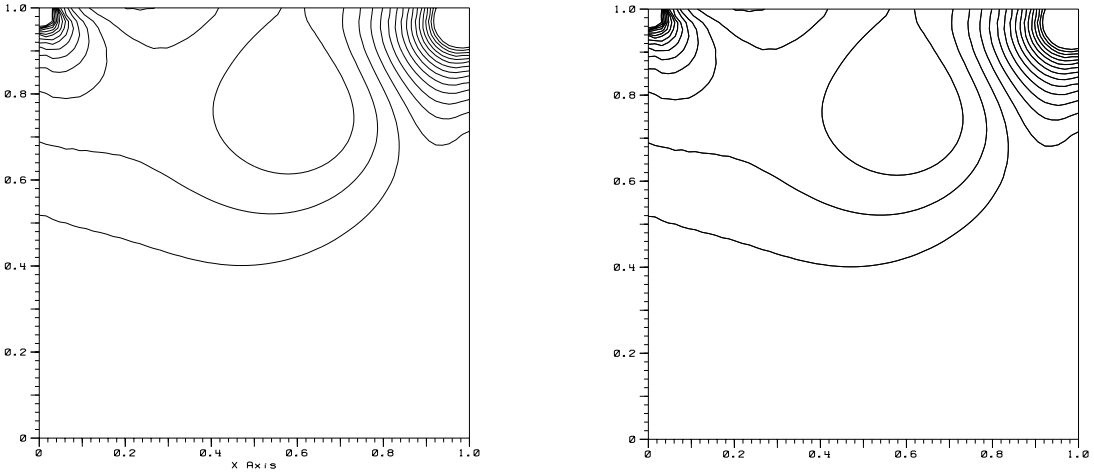

Figure 22. Driven cavity at Re= 100, 64 × 64 grid cells: 30 contour lines of the nodal pressure $p_{\mathcal{V}}^{(2)}$ in [−0·4,0·4]. C =0·08 (left) and C =0·008 (right).

sure and streamlines of the numerical solution after 5000 time steps are shown in Figures 24 and 25. These results are in a good qualitative agreement with the ones presented by Ghia *et al.* [59, p. 400]. For a more quantitative comparison the horizontal (vertical) component of the velocity along the vertical (horizontal) line through the geometric center of the cavity have been drawn in Figure 26. The solid line represents the numerical solution obtained with the present method. The dots are values of a reference solution taken from [59]. The accuracy of this solution has been confirmed by many independent computations.

Falling droplet. A heavy 'droplet' falls through a light fluid atmosphere and impacts into the surface of the heavy fluid in a cavity. The density ratio is 1000:1 and the Froude number equal to one. The flow is assumed to be inviscid and there is no account for surface tension or for a

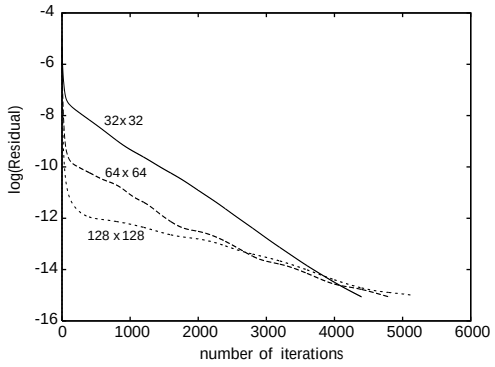

Figure 23. Driven cavity at Re= 1000: Residual versus number of iterations for 32×32, 64×64 and 128×128 grid cells computations; coarser grid solutions have been taken as initial data for finer grid solutions.

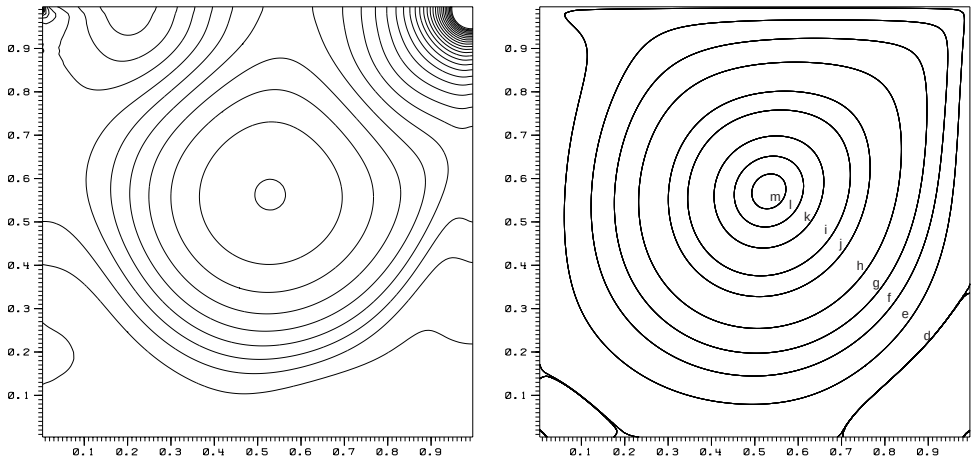

Figure 24. Driven cavity at Re= 1000, 128×128 grid cells: 30 contour lines of the nodal pressure $p_{\overline{\mathcal{V}}}^{(2)}$ in [-0·4;0·4] (left) and streamlines (right). Streamline values and labels from [41].

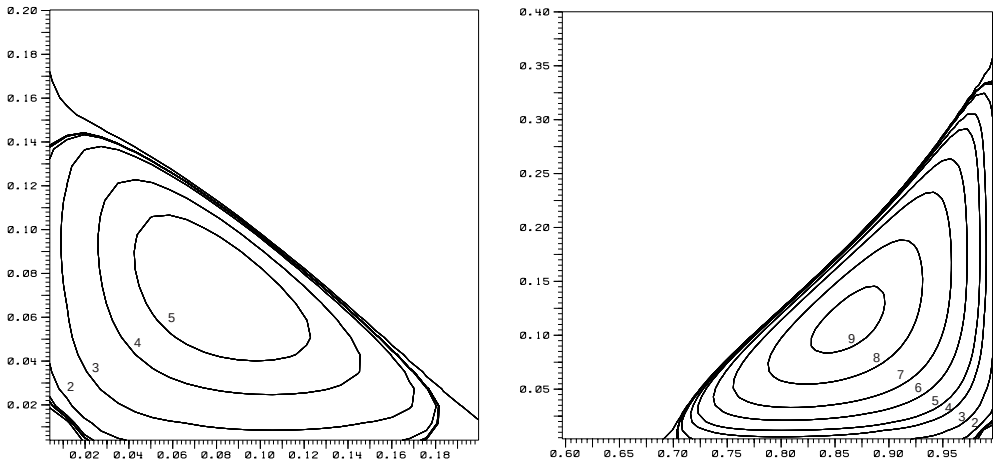

Figure 25. Driven cavity at Re=1000, 128×128 grid cells: streamlines in the left and right bottom secondary vortices. Values and labels from [41].

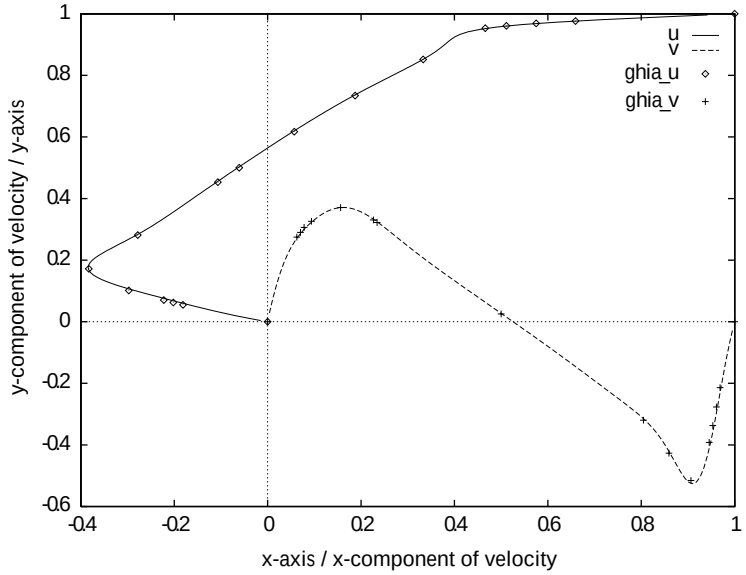

Figure 26. Driven cavity at Re=1000, 128 × 128 grid cells: horizontal (vertical) component of the velocity along the vertical (horizontal) line through the geometric center of the cavity; present results (solid line) and reference solution from [41].

change of the equation of state (hence, the quotes on 'droplet'!). The computational domain is the rectangle $[0, 1] \times [0, 2]$. We present both two- and three-dimensional computations. The goal is to investigate the capability of the method to cope with large density variations.

From a numerical point of view the effect of density variations is to increase the condition number of the discrete Poisson-type operators associated with the numerical computation of the pressure $p^{(2)}$. One might expect poor convergence in the iterative solution of the linear systems and, in the worst case, oscillations in the pressure field $p_{\mathbf{I}}^{(2)}$. Since our interface pressures $p_{\mathbf{I}}^{(2)}$ are computed via a discrete Poisson-type operator which, for two-dimensional equally spaced Cartesian grids, exhibits local grid decoupling, we are thus particularly interested in the behavior of $p_{\mathbf{I}}^{(2)}$ in the two dimensional case.

Two-dimensional case. This problem was originally proposed in Puckett *et al.* [62] to test a tracking method for incompressible variable-density flows. Here the interface between light and heavy fluid is captured, but we still expect our second-order method to describe properly the main features of the flow. The computational grid consists of 64 × 128 cells. The initial data are:

$$\rho(x, y, 0) = \begin{cases} 1000{\cdot}0 & \text{if } 0{\cdot}0 \le y \le 1{\cdot}0 \text{ or } 0{\cdot}0 \le r \le 0{\cdot}2, \\ 1{\cdot}0 & \text{if } 1{\cdot}0 < y \le 2{\cdot}0 \text{ or } 0{\cdot}2 < r, \end{cases}$$

$$p(x, y, 0) = 1, \quad \boldsymbol{v}(x, y, 0) = 0 \quad \text{and} \quad r = \sqrt{(x - 0{\cdot}5)^2 + (y - 1{\cdot}75)^2}\,.$$

Figure 27 shows density contours at a sequence of output times. After the impact of the droplet some areas of lighter fluid appear within the heavy fluid (last three frames). This is consistent with the results shown in [62] where this effect was referred to as 'trapped air bubbles'. For this sequence we monitored the cell interface pressure $p_{\mathbf{I}}^{(2)}$ without noticing any spurious oscillations or local grid decoupling effects. The multi-grid preconditioned conjugate-gradients

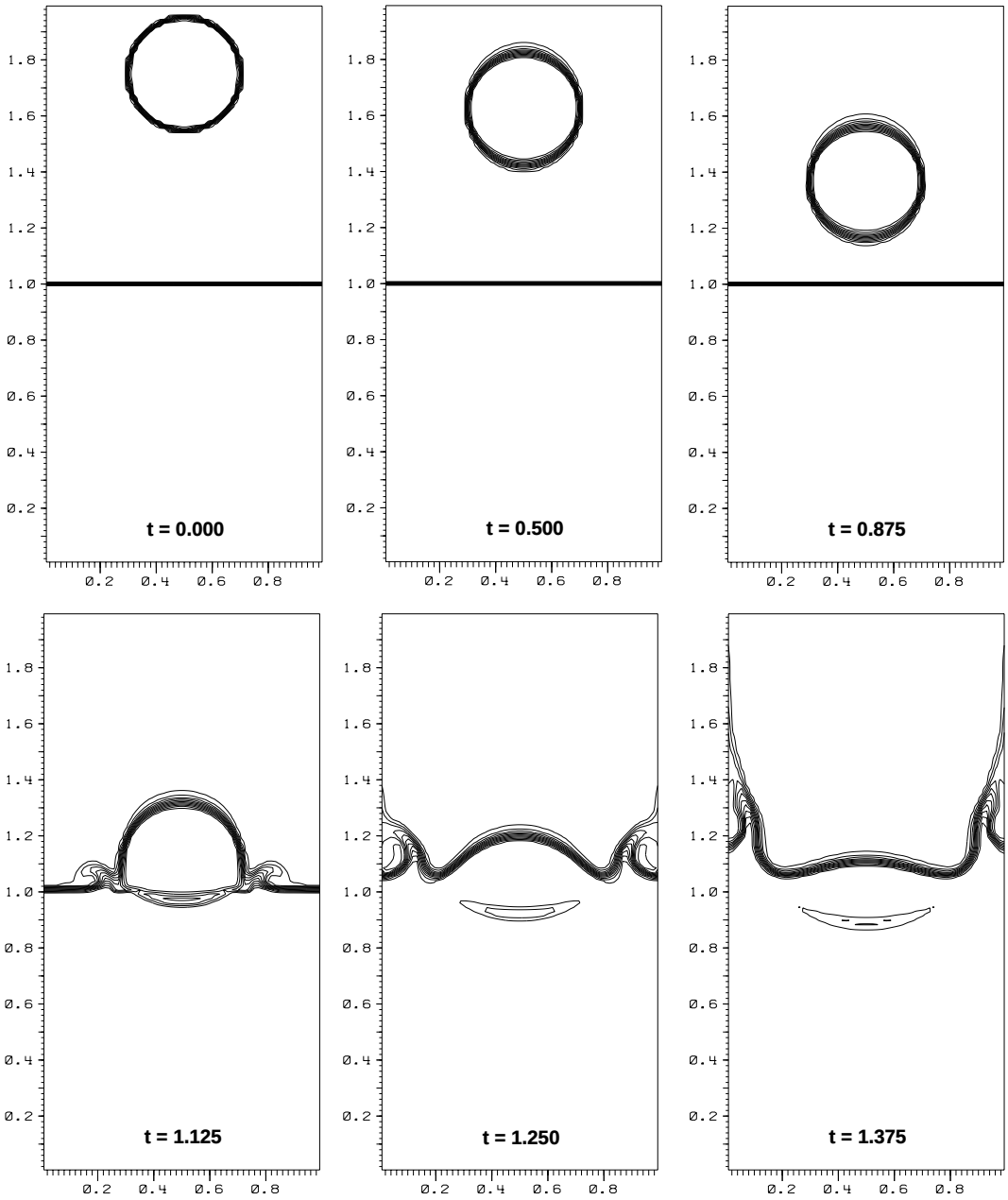

Figure 27. Two-dimensional falling 'droplet' at $Fr = 1$ and density ratio 1000: Contour lines of density in [1,1000].

technique allows the iterative solution of the linear systems for the pressure in about the same number of iterations as for the constant-density case.

Three-dimensional case. This is a simple extension of the previous case to three space dimensions. The grid consists of $64 \times 64 \times 128$ cells. The initial data are:

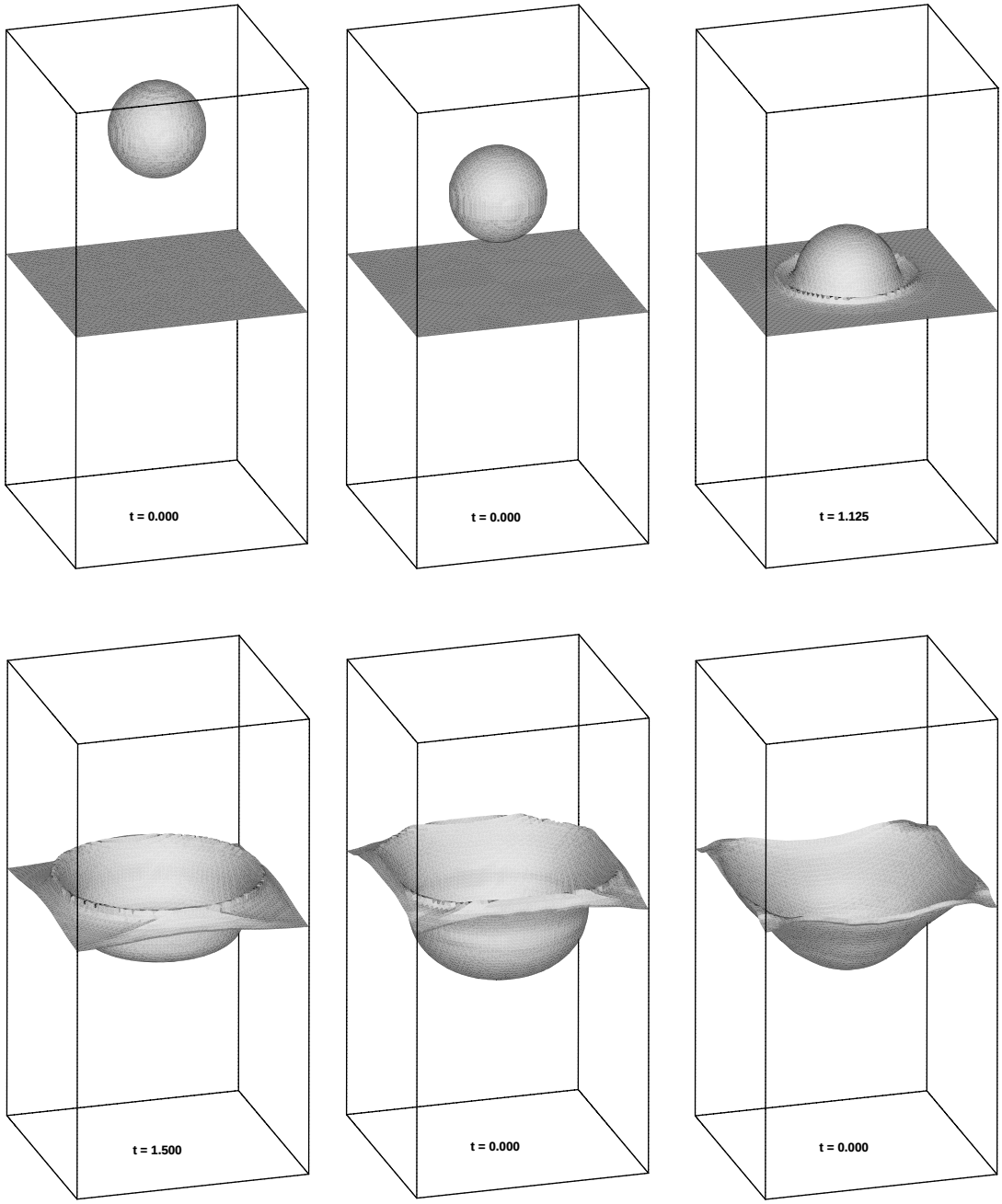

Figure 28. Three-dimensional falling 'droplet' at Fr= 1 and density ratio 1000: Iso-surface $\rho = 500$ of density.

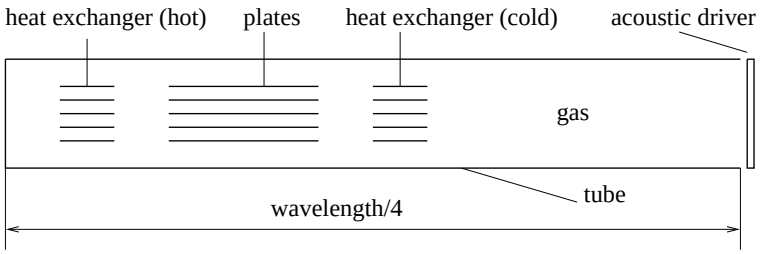

Figure 29. Sketch of a simplified thermo-acoustic refrigerator.

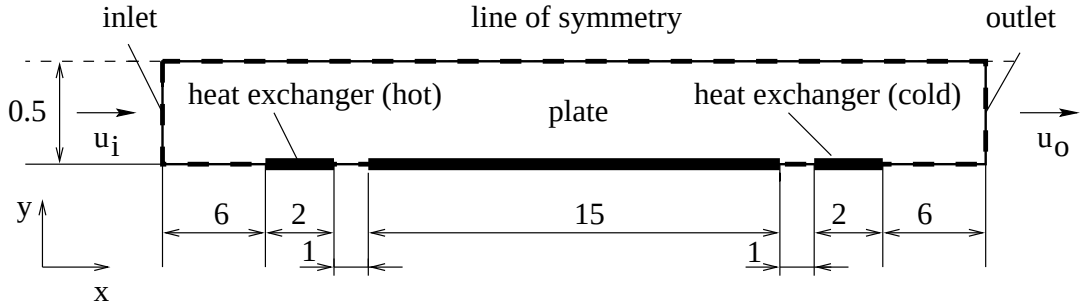

Figure 30. Computational domain (dotted line).

$$\rho(x, y, 0) = \begin{cases} 1000{\cdot}0 & \text{if } 0{\cdot}0 \le z \le 1{\cdot}0 \text{ or } 0{\cdot}0 \le r \le 0{\cdot}2, \\ 1{\cdot}0 & \text{if } 1{\cdot}0 < z \le 2{\cdot}0 \text{ or } 0{\cdot}2 < r, \end{cases}$$

$$p(x, y, 0) = 1, \quad \boldsymbol{v}(x, y, 0) = 0 \quad \text{and} \quad r = \sqrt{(x - 0{\cdot}5)^2 + (y - 0{\cdot}5)^2 + (z - 1{\cdot}75)^2}\,.$$

Figure 28 shows the density iso-surface 500 as the droplet falls and impacts into the surface of the heavy fluid in the closed cavity.

Thermo-acoustic refrigerator. This example shows that our method can treat compressible zero-Mach-number flows with heat conduction. A thermo-acoustic refrigerator basically consists of a resonance tube, a stack of plates, two heat exchangers and an acoustic driver (usually a loudspeaker), (see, [63, 64, 65]). The basic components of a thermo-acoustic refrigerator are sketched in Figure 29: The flow within the tube is characterized by two length scales, namely the short hydrodynamic and the long acoustic scale. The Mach number in the tube is very small, typically $O(10^{-3})$. Thus, the flow between the plates, which are much shorter than the tube, can be assumed to be incompressible with a prescribed velocity field imposed on the inlet and outlet boundaries. The calculation focuses on the flow along the plate and the heat exchangers. The plate is modeled as a zero thickness plate with finite thermal mass. The thickness of the heat exchangers is zero as well. The geometry of the domain for this simplified simulation is shown in Figure 30.

The problem is defined in terms of several characteristic numbers: the Prandtl number Pr, the Reynolds number Re and the ratio of specific heats γ. The temperatures of the heat exchangers T_{hot}, T_{cold} are kept constant. The temperature distribution within the plate is governed by a heat conduction equation:

Table 3. Specific numbers.

Pr	0·68	u_{inlet}	$0{\cdot}7711\cos(t)$
Re	200	v_{inlet}	0·0
γ	5/3	u_{outlet}	$1{\cdot}0267\cos(t)$
T_{hot}	1·0267	v_{outlet}	0·0
T_{cold}	0·9733	λ	0·05
Pe_s	300	κ	41·14

$$\frac{\partial T}{\partial t} = \frac{1}{\text{Pe}_s}\left(\frac{\partial^2}{\partial x^2}T + \frac{2\kappa}{\lambda}\frac{\partial}{\partial y}T\bigg|_{\text{gas}}\right). \tag{4.3.21}$$

Where Pe_s denotes the Peclet number of the solid, κ represents the ratio of the thermal conductivities and λ is the thermal penetration depth. The specific values are listed below. After 200 acoustic cycles a periodical solution is reached. Figure 31 shows the temperature at different times during the 201-th acoustic cycle. The heat fluxes through the surface of the exchangers during an acoustic cycle are shown in Figure 32.

4.3.3. *Summary*

The results discussed above show that a finite-volume compressible-flow solver can be extended to handle incompressible, zero-Mach-number flows. Our approach is general enough to include a wide variety of underlying compressible-flow schemes. The major ingredients of the required extensions are two pressure Poisson solutions. These allow us to enforce zero-Mach-number elliptic divergence constraints for the convective numerical fluxes, as well as for the final cell-centered velocity fields.

The design of the scheme directly draws on the low-Mach-number asymptotic analysis of the governing equations in conservation form presented in Section 2.1. This analysis shows how the well-known velocity- divergence constraint of incompressible flows emerges in a natural way from an associated divergence constraint on the energy flux as the Mach number vanishes. The insight gained in this way is used to construct numerical fluxes of mass, momentum and energy that are consistent with the zero-Mach-number limit. The scheme thus represents a discretization of the full conservation equations rather than one of an asymptotic limit system which would explicitly introduce a velocity-divergence constraint! The computational examples given are chosen to demonstrate various features of the proposed method. Thus, we show second-order accuracy for a test problem proposed by Almgren *et al.*, [56], and we obtain competitive results on the test problem of an advected zero circulation vortex as proposed by Gresho and Chen, [57]. After adding a first-order-in-time extension to viscous incompressible flow, we find very close agreement with published results in the literature for standard driven-cavity test problems (see Ghia, Ghia and Shin, [59]). Notably, grid refinement at constant convection-based CFL number of 0·8 as well as decreasing time steps at constant spatial resolution do not affect the results. This suggests stability and convergence of the method, even though we cannot provide rigorous proofs at this stage. Excellent behavior of the scheme is found for variable density flows. A ‘falling droplet’ with a density ratio of 1000, simulated by a suitable choice of an initial entropy distribution in an ideal gas, is handled without evidence of pressure, velocity or density oscillations.

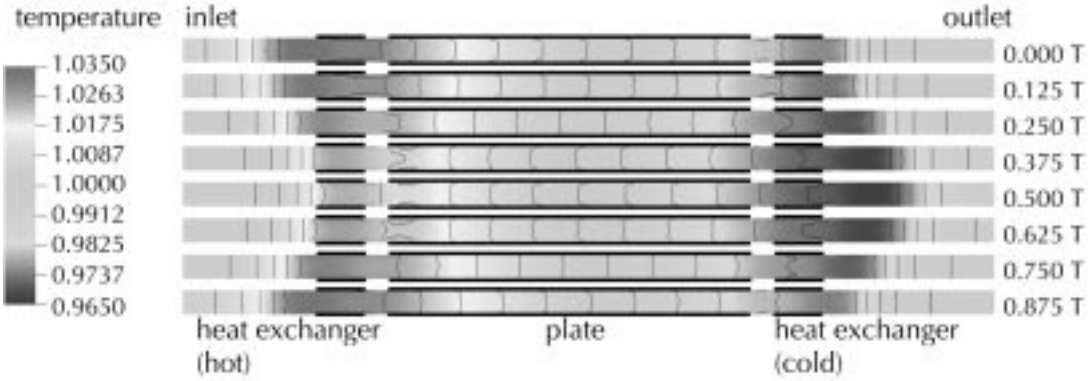

Figure 31. Temperature field during different times of an acoustic cycle; $T := 2\pi$.

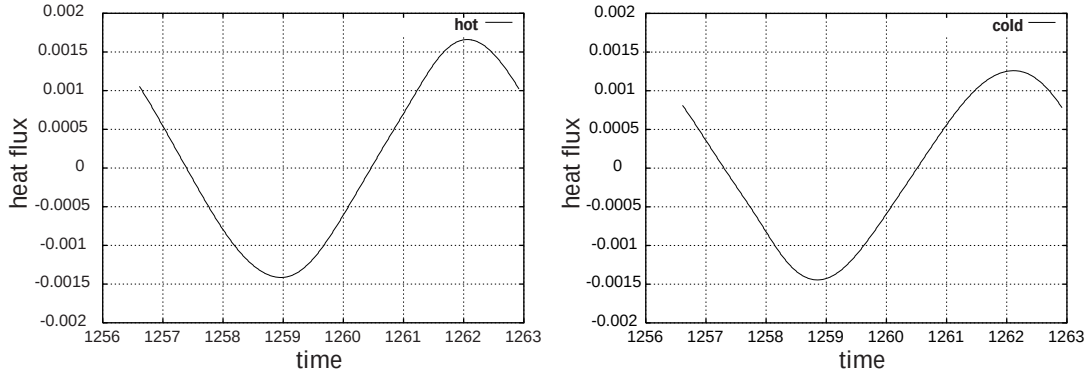

Figure 32. Heat fluxes through the surface of the hot (left) and cold (right) heat exchanger during an acoustic cycle.

4.4. A GODUNOV-TYPE SCHEME FOR WEAKLY COMPRESSIBLE FLOWS

This section is devoted to the extension of a standard conservative finite-volume method designed for the compressible Euler equations to unsteady low-Mach-number flows. Neglecting the gravitational force field, we can rewrite the conservation laws (4.3.1) in one space dimension in the form

$$\partial_t \mathbf{u}(x,t) + \partial_x \mathbf{f}(\mathbf{u}(x,t)) = \mathbf{0} \quad \text{in } \Omega \times \mathbf{R}_0^+, \tag{4.4.1}$$

where $\mathbf{u} = (\rho, m = \rho v, \rho e)^T$ denotes the vector of conserved variables and $\mathbf{f}(\mathbf{u}) = (m, mv + p/\check{\mathrm{M}}^2, Hm)^T$ represents the convective-flux function. As seen in Section 4.3, the eigenvalues of the Jacobian of the flux function are v and $v \pm c/\check{\mathrm{M}}^2$ with the speed of sound $c = \sqrt{\gamma \frac{p}{\rho}}$. Our aim is to construct a finite-volume (FV) Godunov-type method for (4.4.1) which is adaptive in the sense that 1) for $\mathrm{M} \to 0$ it reduces to a FV method for zero-Mach-number flows of the kind described in Section 4.3, 2) for $\mathrm{M} \to 1$ it becomes a standard compressible flow solver. We proceed in three steps:

- Decompose the flux function in the form
  $$\mathbf{f}(\mathbf{u}) = \mathbf{h}(\mathbf{u}) + \mathbf{a}(\mathbf{u}); \tag{4.4.2}$$
- Employ a modified Riemann solver to approximate the fluxes of the system

$$\partial_t \mathbf{u} + \partial_x \mathbf{h}(\mathbf{u}) = \mathbf{0}; \tag{4.4.3}$$

- Correct the obtained fluxes to get an approximate solution of system (4.4.1) which is uniformly accurate independently of the Mach number.

In the first step we define a suitable decomposition of the flux function **f** of Equation (4.4.2). The aim is to decompose **f** in such a way that subsystem (4.4.3) can be efficiently solved with some standard Godunov-type scheme. Moreover, we want the correction to be applied in step 3 to vanish as $\check{\mathrm{M}} \to 1$. Thus, a suitable decomposition should fulfill the following requirements

- System (4.4.3) is hyperbolic and the eigenvalues of the Jacobian of the flux function **h** are $O(1)$ as $\check{\mathrm{M}} \to 0$.

- The flux function **h** has to reproduce **f** in the case that $\check{\mathrm{M}}$ tends to one, *i.e.*,
  $\lim_{\check{\mathrm{M}} \to 1} \mathbf{a}(\mathbf{u}) = \mathbf{0}$.

In agreement with [6] we define the flux function **h** as follows

$$\mathbf{h}(\mathbf{u}) = \begin{pmatrix} m \\ mv + p \\ H^* m \end{pmatrix}. \tag{4.4.4}$$

Here the 'enthalpy' H^* is defined in terms of a non-local pressure p_{NL}:

$$H^* = \frac{\rho e + p_{\mathrm{NL}} + \check{\mathrm{M}}^2 p}{\rho}.$$

This pressure is computed by use of the averaging operator

$$\varphi_\sigma(t) = (\mathcal{M}_\sigma \varphi)(t) = \frac{1}{|\sigma|} \int_\sigma \varphi(x,t)\, \mathrm{d}x, \quad \forall \sigma \subset \Omega$$

as

$$p_{\mathrm{NL}} = \left(1 - \check{\mathrm{M}}^2\right) p_\Omega(0). \tag{4.4.5}$$

A straightforward calculation shows that the eigenvalues of the Jacobian of the flux function **h** are v and

$$v \pm \underbrace{\sqrt{\frac{p + (\gamma - 1)(p_{\mathrm{NL}} + \check{\mathrm{M}}^2 p)}{\rho}}}_{=: c^*}.$$

Moreover, the Jacobian of **h** has a complete set of eigenvectors. Furthermore, one has

$$\mathbf{a}(\mathbf{u}) = \mathbf{f}(\mathbf{u}) - \mathbf{h}(\mathbf{u}) = \begin{pmatrix} 0 \\ -\dfrac{\check{\mathrm{M}}^2 - 1}{\check{\mathrm{M}}^2} p \\ -(\check{\mathrm{M}}^2 - 1) pv - p_{\mathrm{NL}} v \end{pmatrix}. \tag{4.4.6}$$

Taking into account the definition of the non-local pressure (4.4.5) we easily see that $\mathbf{a}(\mathbf{u})$ satisfies the condition

$$\lim_{\check{\mathrm{M}}\to 1} \mathbf{a}(\mathbf{u}) = \mathbf{0}.$$

Therefore, the decomposition $\mathbf{f}(\mathbf{u}) = \mathbf{h}(\mathbf{u}) + \mathbf{a}(\mathbf{u})$ satisfies both requirements (4.4.4) and (4.4.6). For the numerical computation of unsteady flows it is advisable to use a second-order time stepping method. Let $\mathbf{u}^n(x)$ denote an approximation of the solution vector $\mathbf{u}(x, t^n)$ of

$$\partial_t \mathbf{u} + \partial_x \mathbf{g}(\mathbf{u}) = \mathbf{0}. \tag{4.4.7}$$

Then

$$\begin{aligned} \mathbf{u}_{\mathbf{g}}^0(x) &= \mathbf{u}(x, t^0) \\ \mathbf{u}_{\mathbf{g}}^{n+1}(x) &= \mathbf{u}_{\mathbf{g}}^n(x) - \delta t \Phi_{\mathbf{g}}(\mathbf{u}, \delta t), \quad n = 0, 1, \ldots \end{aligned} \tag{4.4.8}$$

with

$$\Phi_{\mathbf{g}}(\mathbf{u}, \delta t) = -\partial_x \mathbf{g}\left(\mathbf{u}_g^n(x) - \frac{\delta t}{2}\partial_x \mathbf{g}\left(\mathbf{u}_{\mathbf{g}}^n(x)\right)\right)$$

represents a consistent second order predictor-corrector time discretization. Let $\Phi = \left(\Phi_{(\rho)}, \Phi_{(m)}, \Phi_{(\rho e)}\right)^T$ be a second-order method for the Euler equations (4.4.1) and $\Phi_{\mathbf{h}}$ a second-order method for the auxiliary system (4.4.3). The difference between the intermediate momenta of the Euler equations and those of the auxiliary system can be written as

$$m^{n+\frac{1}{2}} - m_h^{n+\frac{1}{2}} = \frac{\delta t}{2}\frac{\check{\mathrm{M}}^2 - 1}{\check{\mathrm{M}}^2}\partial_x p^{n+\frac{1}{2}} + O(\delta t^2). \tag{4.4.9}$$

This influence yields the asymptotic correction of the mass fluxes in the form

$$\begin{aligned} \rho^{n+1} &= \rho^n - \delta t \Phi_{(\rho)}(\mathbf{u}, \delta t) + O(\delta t^3) \\ &\overset{(4.4.9)}{=} \rho^n - \delta t \partial_x \left(m_{\mathbf{h}}^{n+\frac{1}{2}} + \frac{\delta t}{2}\frac{\check{\mathrm{M}}^2 - 1}{\check{\mathrm{M}}^2}\partial_x p^{n+\frac{1}{2}}\right) + O(\delta t^3) \\ &= \rho^n - \delta t \Phi_{\mathbf{h},(\rho)}(\mathbf{u}, \delta t) - \delta t \Phi_{\mathbf{a},(\rho)}(\mathbf{u}, \delta t) + O(\delta t^3) \end{aligned}$$

with

$$\Phi_{\mathbf{a},(\rho)}(\mathbf{u}, \delta t) = \frac{\delta t}{2}\frac{\check{\mathrm{M}}^2 - 1}{\check{\mathrm{M}}^2}\partial_x^2 p^{n+\frac{1}{2}}. \tag{4.4.10}$$

The same analysis applied to the intermediate velocity distribution gives ($\rho^{n+\frac{1}{2}} = \rho_{\mathbf{h}}^{n+\frac{1}{2}}$)

$$v^{n+\frac{1}{2}} = v_{\mathbf{h}}^{n+\frac{1}{2}} + \frac{\delta t}{2\rho^{n+\frac{1}{2}}}\frac{\check{\mathrm{M}}^2 - 1}{\check{\mathrm{M}}^2}\partial_x p^{n+\frac{1}{2}} + O(\delta t^2).$$

Consequently, the entire momentum flux including the second-order asymptotic correction terms reads

$$m^{n+1} = m^n - \delta t \Phi_{\mathbf{h},(m)}(\mathbf{u}, \delta t) - \delta t \Phi_{\mathbf{a},(m)}(\mathbf{u}, \delta t) + O(\delta t^3)$$

where

$$\begin{aligned}\Phi_{\mathbf{a},(m)}\,(\mathbf{u},\delta t) = & -\frac{\check{\mathrm{M}}^2-1}{\check{\mathrm{M}}^2}\partial_x p^{n+\frac{1}{2}} + \partial_x (p-p_{\mathbf{h}})^{n+\frac{1}{2}} \\ & +\delta t\frac{\check{\mathrm{M}}^2-1}{\check{\mathrm{M}}^2}\partial_x\left(v_{\mathbf{h}}^{n+\frac{1}{2}}\partial_x p^{n+\frac{1}{2}}\right).\end{aligned} \tag{4.4.11}$$

Analogously, we achieve the energy flux in the form

$$(\rho e)^{n+1} = (\rho e)^n - \delta t\,\Phi_{\mathbf{h},(\rho e)}\,(\mathbf{u},\delta t) - \delta t\,\Phi_{\mathbf{a},(\rho e)}\,(\mathbf{u},\delta t) + O(\delta t^3) \tag{4.4.12}$$

where

$$\begin{aligned}&\Phi_{\mathbf{a},(\rho e)}\,(\mathbf{u},\delta t) \\ &= -(\check{\mathrm{M}}^2-1)\partial_x (pv)^{n+\frac{1}{2}}\partial_x (p_{\mathrm{NL}}v)^{n+\frac{1}{2}} \\ &+\check{\mathrm{M}}^2\partial_x\left((p^{n+\frac{1}{2}}-p_{\mathbf{h}}^{n+\frac{1}{2}})v^{n+\frac{1}{2}}\right) + \frac{\delta t}{2}\frac{\check{\mathrm{M}}^2-1}{\check{\mathrm{M}}^2}\partial_x (H_{\mathbf{h}}^{*,n+\frac{1}{2}}\partial_x p^{n+\frac{1}{2}}) \\ &+\frac{\delta t}{2}\partial_x\left(\left((\check{\mathrm{M}}^2-1)\partial_x (pv)^{n+\frac{1}{2}} + \partial_x (p_{\mathrm{NL}}v)^{n+\frac{1}{2}}\right)v^{n+\frac{1}{2}}\right).\end{aligned} \tag{4.4.13}$$

Two facts are remarkable. First, the additional terms representing the differences between $\Phi_{\mathbf{a}}$ and a straightforward discretization of the asymptotic fluxes $\mathbf{a}(\mathbf{u})$ are of order $O(\delta t^2)$ and hence negligible in the case of a first-order time-stepping procedure. Second, the above-mentioned additional terms can be substituted by an arbitrary first-order approximation without affecting the order of accuracy. For example, one can evaluate the pressure derivative within equation (4.4.9) at any time level $t^m \in [t^n, t^{n+1}]$.

4.4.1. *Evolution of the spatially homogeneous leading-order pressure*

According to the results of the asymptotic single- as well as multiple-scale analysis, the evolution of the spatial homogeneous leading-order pressure $p^{(0)}$ is due to compression from the boundary $\partial\Omega$ or expansion of the reacting gas itself. In agreement with Equation (2.1.38) we employ

$$p^{(0),n+1} = p^{(0),n} - \delta t\gamma p^{(0),n}\left(v_r^n - v_\ell^n\right), \tag{4.4.14}$$

where v_r and v_ℓ represent the velocity at the right and left boundary of the computational domain, respectively.

4.4.2. *Evolution of the acoustic first-order pressure*

The evolution of the acoustic pressure $p^{(1)}$ is governed by the system of linearized acoustics (2.1.41), which can be rewritten in the form

$$\partial_t \overline{m} + \frac{1}{\check{\mathrm{M}}}\partial_x p^{(1)} = 0, \quad \partial_t p^{(1)} + \frac{1}{\check{\mathrm{M}}}\partial_x\left(\overline{c}\;\overline{m}\right) = 0, \tag{4.4.15}$$

where

$$\overline{c} = \sqrt{\gamma \frac{p^{(0)}}{\overline{\rho}}}.$$

The system (4.4.15) is hyperbolic with characteristic signal speeds $\pm\frac{\overline{c}}{\check{\mathrm{M}}} = O\left(\frac{1}{\check{\mathrm{M}}}\right)$. Since the time-step size with explicit discretization of the auxiliary system satisfies $\delta t = O(\delta x)$, it is necessary to employ a suitable discretization technique for the solution of system (4.4.15) to overcome the restrictive Courant-Friedrichs-Lewy condition for an explicit forward Euler time discretization. Implicit time-stepping schemes have the advantage that the numerical domain of dependence always covers the physical one and hence, these methods inherently fulfill the CFL-condition. Due to the fortunate property that the Jacobian of the flux function within the system (4.4.15) is very simple, we decided to employ an implicit discretization. The linear system arising from the linearization of the flux function is solved by means of the BiCGSTAB method [66] preconditioned by an incomplete LU factorization technique. The initialization of the long-wave momentum and density distribution is performed by the decomposition algorithm described in Section 4.1.

4.4.3. *Energy-Poisson-Equation*

Introducing the equation of state written as

$$(\rho e)^{n+1} = \frac{p^{(0),n+1}}{\gamma - 1} + \frac{\check{\mathrm{M}} p^{(1),n+1}}{\gamma - 1} + \frac{\check{\mathrm{M}}^2 p^{(2),n+1}}{\gamma - 1} + \frac{\check{\mathrm{M}}^2}{2} \rho^{n+1} \left(v^{n+1}\right)^2$$

into the energy equation (4.4.12) and omitting terms of order $O(\delta t^3)$ we have

$$\begin{aligned} \frac{\check{\mathrm{M}}^2}{\gamma - 1} p^{(2),n+1} = \; & (\rho e)^n - \frac{p^{(0),n+1}}{\gamma - 1} - \frac{\check{\mathrm{M}} p^{(1),n+1}}{\gamma - 1} - \frac{\check{\mathrm{M}}^2}{2} \rho^{n+1} \left(v^{n+1}\right)^2 \\ & - \delta t \, \Phi_{\mathbf{h},(\rho e)} \left(\mathbf{u}, \delta t\right) - \delta t \, \Phi_{\mathbf{a},(\rho e)} \left(\mathbf{u}, \delta t\right). \end{aligned}$$

Note that the leading-order pressure $p^{(0),n+1}$ and the acoustic pressure $p^{(1),n+1}$ can be computed by means of (4.4.14) and by solving the system of linearized acoustics (4.4.15), respectively. We use a particular implicit discretization of the asymptotic part (4.4.13):

$$\begin{aligned} & \Phi_{\mathbf{a},(\rho e)} \left(\mathbf{u}, \delta t\right) \\ & = -(\check{\mathrm{M}}^2 - 1) \partial_x (pv)^{n+\frac{1}{2}} - \partial_x (p_{\mathrm{NL}} v)^{n+\frac{1}{2}} \\ & \quad + \check{\mathrm{M}}^2 \partial_x \left((p^{n+\frac{1}{2}} - p_{\mathbf{h}}^{n+\frac{1}{2}}) v^{n+1} \right) + \frac{\delta t}{2} \frac{\check{\mathrm{M}}^2 - 1}{\check{\mathrm{M}}^2} \partial_x (H_{\mathbf{h}}^{*,n+\frac{1}{2}} \partial_x p^{n+1}) \\ & \quad + \frac{\delta t}{2} \partial_x \left(\left((\check{\mathrm{M}}^2 - 1) \partial_x (pv)^{n+1} + \partial_x (p_{\mathrm{NL}} v)^{n+1} \right) v^{n+1} \right). \end{aligned} \tag{4.4.16}$$

Using the pressure decomposition in the asymptotic flux function (4.4.16) and assuming that the pressure terms $p^{n+\frac{1}{2}}$ and $p_{\mathbf{h}}^{n+\frac{1}{2}}$ as well as the enthalpy form $H_{\mathbf{h}}^{*,n+\frac{1}{2}}$ are available, we can discretize the derivatives within the asymptotic fluxes by means of central differences to achieve a linear system of equations

$$\mathbf{A}\mathbf{p}^{(2),n+1} = \mathbf{b}, \quad \mathbf{p}^{(2),n+1} = \left(p_1^{(2),n+1}, \ldots, p_k^{(2),n+1} \right)^T \tag{4.4.17}$$

for the calculation of the second-order pressure. The matrix and the right- hand side of Equation (4.4.17) contain density and velocity contributions at the time level t^{n+1}. Due to this fact we employ a fix-point iteration where the asymptotic flux corrections $\Phi_{\mathbf{a}}$ are computed simultaneously. Therefore, we take $v_{\mathbf{h}}^{n+1}$ and $\rho_{\mathbf{h}}^{n+1}$, provided by the discretization of the auxiliary system as the initial guess for the velocity and density (*i.e.* $v^{n+1,0} = v_{\mathbf{h}}^{n+1}$, $\rho^{n+1,0} = \rho_{\mathbf{h}}^{n+1}$), respectively. Now, the matrix and the right-hand side are fixed and one can solve the system (4.4.17) to obtain $p^{(2),n+1,0}$. Using the variables $\rho^{n+1,0}$, $v^{n+1,0}$, and $p^{(2),n+1,0}$, we can evaluate the asymptotic fluxes completely by means of a Crank-Nicolson approach. Clearly, a prescription for the computation of $p^{n+\frac{1}{2}}$, $p_{\mathbf{h}}^{n+\frac{1}{2}}$, and $H_{\mathbf{h}}^{*,n+\frac{1}{2}}$ is required to close the system. The pressure $p_{\mathbf{h}}^{n+\frac{1}{2}}$ and the enthalpy form $H_{\mathbf{h}}^{*,n+\frac{1}{2}}$ are given by the discretization of the auxiliary system (4.4.3) using $\tilde{\delta t} = \frac{\delta t}{2}$. In order to compute the pressure $p^{n+\frac{1}{2}}$, we use the same procedure as mentioned above for the time interval $[t^n, t^{n+\frac{1}{2}} = t^n + \tilde{\delta t}]$ where the approximation

$$
\begin{aligned}
&\Phi_{\mathbf{a},(\rho e)}\,(\mathbf{u}, \delta t) \\
&\quad = -(\check{\mathrm{M}}^2 - 1)\partial_x (pv)^{n+\frac{1}{2}} - \partial_x (p_{\mathrm{NL}} v)^{n+\frac{1}{2}} \\
&\qquad + \check{\mathrm{M}}^2 \partial_x \left((p^{n+\frac{1}{2}} - p_{\mathbf{h}}^{n+\frac{1}{2}}) v^{n+\frac{1}{2}} \right) + \tilde{\delta t} \frac{\check{\mathrm{M}}^2 - 1}{\check{\mathrm{M}}^2} \partial_x \left(H_{\mathbf{h}}^{*,n+\frac{1}{2}} \partial_x p^{n+\frac{1}{2}} \right) \\
&\qquad + \tilde{\delta t} \partial_x \left(\left((\check{\mathrm{M}}^2 - 1)\partial_x (pv)^{n+\frac{1}{2}} + \partial_x (p_{\mathrm{NL}} v)^{n+\frac{1}{2}} \right) v^{n+\frac{1}{2}} \right)
\end{aligned}
$$

is employed and the Crank-Nicolson time-stepping scheme for the asymptotic fluxes is replaced by a backward Euler approach.

4.4.4. *Spatial discretization*

We discretize the Euler equations (4.4.1) on a bounded domain $\Omega \subset \mathbf{R}$. The computational domain is subdivided into control volumes $\sigma_1, \ldots, \sigma_k$. First, consider the auxiliary hyperbolic system (4.4.3). We call $\mathbf{u}$ a weak solution of system (4.4.3) on Ω, if

$$
\frac{\mathrm{d}}{\mathrm{d}t} \int_{\sigma} \mathbf{u} \, \mathrm{d}x + \mathbf{h}(\mathbf{u})\big|_{\sigma^\ell}^{\sigma^r} = \mathbf{0}
$$

holds for all control volumes $\sigma \subset \Omega$ with σ^r and σ^ℓ representing the right and left boundary of σ, respectively. To compute numerical fluxes for the cell averages

$$
\mathbf{u}_i(t) = \left(\mathcal{M}_{\sigma_i} \mathbf{u} \right)(t), \tag{4.4.18}
$$

we used the modified Riemann-problem solver described in [6]. In the limit $\check{\mathrm{M}} \to 1$ this flux is consistent with a standard numerical flux for the Euler equations. To achieve a second-order scheme in space and time, we use linear reconstruction of the characteristic variables in spatial directions as well as a MUSCL approach in time. A detailed description of this Godunov-type algorithm is given in [67].

The approximation of the asymptotic fluxes is done via finite differences. Each physical quantity $\varphi_{i+\frac{1}{2}}$ at the interface between two adjacent boxes σ_i and σ_{i+1} is computed as a mean value of the corresponding cell averages. Similarly, we approximate the derivatives $(\partial_x \varphi)_{i+\frac{1}{2}}$ in the form of central differences.

4.4.5. *Time-dependent scaling*

In order to gain a suitable scaling of the physical quantities one has to calculate the required reference values from a given flow field. In a standard approach the reference values are set at the initial time and kept constant throughout the computation. Here, however, we want to consider flows which may evolve through different regimes. Almost incompressible initial conditions may turn into weakly compressible flows or *vice versa*. Thus, it is necessary to implement some kind of dynamical time-dependent scaling and the reference values must adapt to the evolving numerical solution.

As seen in Section 2.1, a scaling is defined in terms of $\hat{v}_{\text{ref}}$, $\hat{p}_{\text{ref}}$ and $\hat{\rho}_{\text{ref}}$ via the Mach number $\check{\text{M}}$

$$\check{\text{M}} = \frac{\hat{v}_{\text{ref}}}{\sqrt{\frac{\hat{p}_{\text{ref}}}{\hat{\rho}_{\text{ref}}}}}, \tag{4.4.19}$$

which is a measure of the compressibility of the flow. As seen in Section 4.1, $\check{\text{M}}$ is also a measure of the wave length of acoustic waves. We assume that a nearly incompressible flow field is characterized by the following two properties of the dimensional quantities. First, we expect that the divergence of the velocity filed is very small, and second, the flow field shows only tiny fluctuations within the pressure distribution.

The time-dependent reference values for density and pressure are determined by averaging each quantity over the whole domain Ω,

$$\hat{\rho}_{\text{ref}} = \hat{\rho}_{\text{ref}}(t) = \frac{1}{|\Omega|} \int_{\Omega} \hat{\rho}(\boldsymbol{x}, t)\, \mathrm{d}\boldsymbol{x}$$

and

$$\hat{p}_{\text{ref}} = \hat{p}_{\text{ref}}(t) = \frac{1}{|\Omega|} \int_{\Omega} \hat{p}(\boldsymbol{x}, t)\, \mathrm{d}\boldsymbol{x},$$

respectively. Using these values, we can determine the global reference of the speed of sound as

$$\hat{c}_{\text{ref}} = \sqrt{\gamma \frac{\hat{p}_{\text{ref}}}{\hat{\rho}_{\text{ref}}}}.$$

We define three indicators to measure the different properties of weakly compressible fluid flows. One of these is coupled with the pressure distribution as stated in Section 4.1. To prevent misunderstandings, the parameter which is calculated within the decomposition algorithm is called $\check{\text{M}}_l$. The other two characterize the velocity flow field and are given by

$$\check{M}_v = C_v \frac{\max_{\boldsymbol{x} \in \Omega} |\hat{\boldsymbol{v}}|}{\hat{c}_{\text{ref}}}$$

and

$$\check{M}_{\text{div}} = C_{\text{div}} \sqrt{\frac{\max_{\boldsymbol{x} \in \Omega} |\partial_x \hat{\boldsymbol{v}}|}{\hat{c}_{\text{ref}}}}.$$

Now, we can formally define the reference parameter $\check{\mathrm{M}}$. In order to ensure that the standard Godunov-type solver is used in the case that one indicator is greater or equal than a critical value α, $\alpha \leq 1$, we define

$$\tilde{\check{\mathrm{M}}} = \min\left\{\alpha, \max(\check{M}_v, \check{M}_{\mathrm{div}}, \check{\mathrm{M}}_l)\right\},$$

and a function

$$g(\tilde{\check{\mathrm{M}}}) = 1 + \frac{\frac{1}{\alpha} - 1}{\alpha^2}\tilde{\check{\mathrm{M}}}^2.$$

The reference parameter is then given by

$$\check{\mathrm{M}} = g(\tilde{\check{\mathrm{M}}})\tilde{\check{\mathrm{M}}}, \quad \tilde{\check{\mathrm{M}}} \in [0, 1],$$

where Equation (4.4.19) now yields the velocity reference in the form

$$\hat{v}_{\mathrm{ref}} = \frac{\check{\mathrm{M}}\hat{c}_{\mathrm{ref}}}{\sqrt{\gamma}}.$$

We complete the scaling process by taking the reference time equal to the advective time scale:

$$\hat{t}_{\mathrm{ref}} = \frac{\hat{l}_{\mathrm{ref}}}{\hat{v}_{\mathrm{ref}}}.$$

Due to the indicators $\check{M}_v$ and $\check{M}_{\mathrm{div}}$ it is guaranteed that the dimensionless velocity field is limited,

$$\max_{\boldsymbol{x}\in\Omega} |\boldsymbol{v}| = \frac{\max_{\boldsymbol{x}\in\Omega} |\hat{\boldsymbol{v}}|}{\hat{v}_{\mathrm{ref}}} = \sqrt{\gamma}\frac{\check{M}_v}{\check{\mathrm{M}}},$$

and that the divergence-free condition in the limit of a vanishing Mach number is fulfilled,

$$\max_{\boldsymbol{x}\in\Omega} |\partial_x \hat{\boldsymbol{v}}| = \frac{\max_{\boldsymbol{x}\in\Omega} |\partial_x \boldsymbol{v}|}{\hat{v}_{\mathrm{ref}}} = \sqrt{\gamma}\frac{\check{M}^2_{\mathrm{div}}}{\check{\mathrm{M}}}.$$

We want to add some remarks regarding the adaptive concept. As seen before, a time-dependent adaption can easily be achieved by a simple rescaling of each physical quantity after each time step. Because the decomposition of the physical quantities has to be carried out at each time step, the computation of the indicators, as well as of the average values, is not very expensive in comparison to the costs of the decomposition. But it is possible to decrease the computational effort and avoid the rescaling of density and pressure, if their average values do not rapidly change in time. Then, only the velocity field has to be rescaled after each time step to employ the influences of a varying reference parameter $\check{\mathrm{M}}$ to the flow field.

4.4.6. *Numerical results*

In order to test the novel decomposition algorithm described in Section 4.1 we study 1) a weakly compressible flow with large density fluctuations and 2) the transition of a weakly incompressible flow into the compressible regime. These problems were originally proposed in [6].

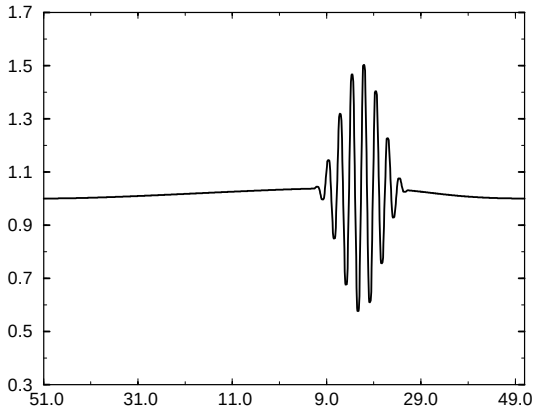

Figure 33. Density distribution at time $t = 5,071$ s.

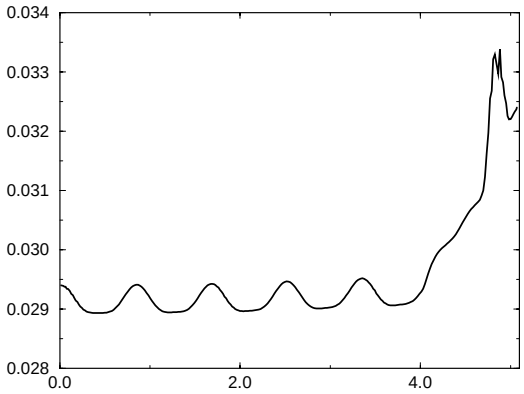

Figure 34. Time dependent adaptation of the Mach number parameter $\hat{M}$.

First, consider a long-wave acoustic signal periodically passing through a region in which the density has some short-wave-length large-amplitude fluctuations. Every period the density distribution will be displaced by the acoustic signal in one direction. The computation is carried over on $\hat{\Omega} = [-51, 51]$ which is subdivided into 1020 regular cells. The initial conditions are given by

$$\hat{\rho}(x, t = 0) = \left(1 + 2\check{\mathrm{M}}\left(1 + \cos(2\check{\mathrm{M}}\pi x)\right) + \Phi(x)\tfrac{1}{2}\sin(80\check{\mathrm{M}}\pi x)\right),$$

$$\hat{v}(x, t = 0) = \sqrt{\gamma}\left(1 + \cos(2\check{\mathrm{M}}\pi x)\right),$$

$$\hat{p}(x, t = 0) = \frac{4}{\check{\mathrm{M}}^2}\left(1 + 2\gamma\check{\mathrm{M}}\left(1 + \cos(2\pi\check{\mathrm{M}}x)\right)\right)$$

and

$$\Phi(x) = \begin{cases} \frac{1}{2}\left(1 - \cos(10\check{\mathrm{M}}\pi x)\right) \ , \text{ if } 0 \le x \le \dfrac{2}{10\check{\mathrm{M}}}, \\ 0, \qquad\qquad\qquad \text{otherwise.} \end{cases}$$

Periodic boundary conditions are imposed on the left and on the right end of $\hat{\Omega}$. The parameter $\check{\mathrm{M}}$ and the reference length $\hat{l}_{\mathrm{ref}}$ are set to $\frac{1}{102}$ and 1, respectively.

In Figure 33 the density profile at the end of the computation ($T = 5,071$) is plotted. The amplitudes of the short-wave density perturbation are almost preserved. The time evolution of the reference parameter $\check{\mathrm{M}}$ is shown in Figure 34. The small oscillations of $\check{\mathrm{M}}$ are due to the fact that the acoustic wave moves faster than the density distribution. Therefore, density fluctuations change their position relative to the extrema of the acoustic wave. At the beginning of the computation the indicator $\check{M}_v$ controls the progress of the reference parameter. Then, the acoustic wave slowly steepens and at the end the indicator $\check{M}_{\mathrm{div}}$ takes over.

In the second example we compute the steepening of an acoustic wave into a shock. We use a regular discretization of the domain $\hat{\Omega} = [-22, 44]$ into 330 boxes with periodic boundary conditions. The initial conditions are

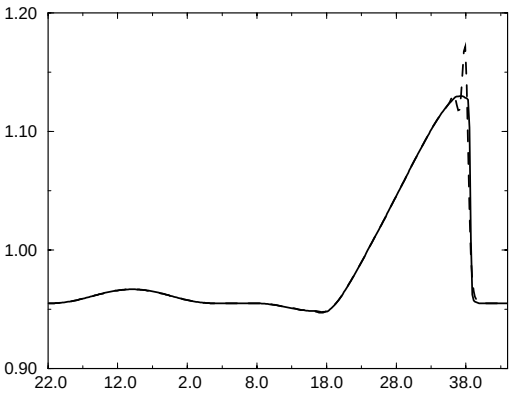

Figure 35. Density distribution at time $t = 33$ s.

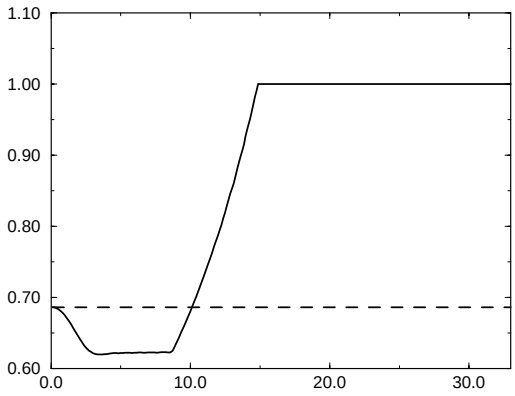

Figure 36. Evolution of the reference parameter.

$$\hat{\rho}(x, t = 0) = \left(0{\cdot}955 + \frac{1}{11}\left(1 - \cos\left(\frac{\pi x}{11}\right)\right)\right),$$

$$\hat{v}(x, t = 0) = \frac{\sqrt{\gamma}}{11}\left(1 - \cos\left(\frac{\pi x}{11}\right)\right),$$

$$\hat{p}(x, t = 0) = \left(2\gamma + \frac{\gamma}{11}\left(1 - \cos\left(\frac{\pi x}{11}\right)\right)\right),$$

for $x \leq 0$ and

$$\hat{\rho}(x, t = 0) = 0{\cdot}955, \quad \hat{v}(x, t = 0) = 0, \quad \hat{p}(x, t = 0) = 2\gamma,$$

otherwise. The reference length is $\hat{l}_{\text{ref}} = 1$. Figure 35 shows the density distribution at time $t = 33$ with and without adaptation of $\check{\text{M}}$. The time evolution of $\check{\text{M}}$ is given in Figure 36. The comparison between the two computations indicates the necessity of dynamically computing $\check{\text{M}}$ and adapting the computational method in the case of transitions from weakly compressible to compressible flow regimes.

4.5. Hyperbolic elliptic splitting for MHD equations

In this section the aim is to use results of Section 2.2 in distinguishing between terms related with pure convection and terms related with the fast wave speeds. As in the case of Euler equations the idea behind this is to get a splitting of the system that enables us to treat the convection terms that remain hyperbolic also in the limit, and the fast-wave-speed terms, that become elliptic in the limit, with different numerical methods.

Especially for fusion plasma, the time-step stability constraint of explicit schemes may often be too restrictive and several implicit or semi-implicit schemes have been proposed (see [68], [69]) and references therein. For the case of small Mach numbers, the implicitness of our approach reduces to a simple pressure-correction equation. The convection system for the MHD equations takes the following form:

$$\rho_t + \rho_x u = 0\,, \tag{4.5.1}$$

$$u_t + uu_x + \frac{1}{2Av^2\rho}(B^2)_x = 0 \,, \tag{4.5.2}$$

$$v_t + uv_x - \frac{1}{\mathrm{Av}^2\rho}B_1B_{2x} = 0 \,, \tag{4.5.3}$$

$$w_t + uw_x - \frac{1}{\mathrm{Av}^2\rho}B_1B_{3x} = 0 \,, \tag{4.5.4}$$

$$B_{2t} + B_2u_x + uB_{2x} - B_1v_x = 0 \,, \tag{4.5.5}$$

$$B_{3t} + B_3u_x + uB_{3x} - B_1w_x = 0 \,, \tag{4.5.6}$$

$$p_t + p_xu = 0 \,. \tag{4.5.7}$$

As usual we can write Equations (4.5.1) – (4.5.7) as a system

$$q_t + Aq_x = 0 \tag{4.5.8}$$

of evolution equations with the vector

$$q = (\rho, u, v, w, B_2, B_3, p)^T \tag{4.5.9}$$

of the physical variables. The Matrix A has the eigenvalues

$$\lambda_1 = u - \frac{1}{\mathrm{Av}}\sqrt{\frac{B^2}{\rho}} \,, \qquad \lambda_2 = u - \frac{1}{\mathrm{Av}}c_A \,, \tag{4.5.10}$$

$$\lambda_3 = \lambda_4 = \lambda_5 = u \,, \tag{4.5.11}$$

$$\lambda_6 = u + \frac{1}{\mathrm{Av}}c_A \,, \qquad \lambda_7 = u + \frac{1}{\mathrm{Av}}\sqrt{\frac{B^2}{\rho}} \tag{4.5.12}$$

(c_A is the Alfvén velocity) and a complete set of eigenvectors. Therefore, system (4.5.1) – (4.5.7) is strictly hyperbolic. The eigenvalues of A correspond to the different wave speeds associated with fluid convection and the magneto-sonic waves. The remaining terms of (2.2.2) reduce to the system of the sonic waves (4.2.6). Therefore, we have all terms that cause fast wave speeds in this system. We call this system the elliptic system. The extension to multiple space dimensions is straightforward.

While the hyperbolic system (4.5.1) – (4.5.7) can be approximated with an explicit scheme, the system of the sonic waves should be discretized implicitly in time. This can be done as described in Section 4.2 for the equations of gas dynamics.

In the case of small Alfvén number the terms $B_2u_x - B_1v_x$ and $B_3u_x - B_1w_x$ become constant in space. Their time behavior is determined by the boundary values, so the information propagates with infinite velocity and may be considered to be elliptic. The leading-order terms of the derivatives of the magnetic terms in the velocity equations now vanish and B becomes constant in space. In this case the splitting of the fast and slow waves may not lead to an efficient approximation in comparison with a fully implicit scheme.

5. Conclusions

In this paper we have introduced the notion of asymptotically adaptive numerical methods. This research was motivated by the fact that singularly perturbed systems typically require very different numerical solution methods, depending on whether they are far from or very close to the singular limit. This issue becomes critical when, in some general application, the solution dynamically evolves towards or away from an asymptotic limit regime. In that case, standard numerical methods will fail one way or the other. Here we have proposed a new strategy for the construction of uniformly applicable discretizations. The approach requires a close interplay between application-oriented asymptotics and numerical analysis. Typically, one must first detect the origin of some failure of an available standard numerical scheme. This failure is then traced back to an asymptotic singular limit. Next, an asymptotic analysis is pursued, yielding valuable insight into the changes of the problem's mathematical structure as this limit regime is approached. This knowledge is then exploited to construct an extended numerical scheme that operates with uniform efficiency and accuracy for arbitrary values of the asymptotic parameter. Finally, for problems in which the asymptotic parameter itself is part of the solution, one needs additional control strategies which determine the actual instantaneous or local parameter value and trigger an automatic adjustment of the numerical discretization.

In this paper we have described a number of typical applications that call for an implementation of the above strategy. These include variable-density low-Mach-number flows, atmospheric flows under a distinguished limit of low-Froude and low-Mach numbers, and Magneto-Hydrodynamics at low Mach or Alfvén numbers. For the 'pure' low-Mach-number case, we have almost completed the program sketched above. A numerical method for fully compressible, multi-dimensional flows has been modified to also 'survive' the zero-Mach-number limit. We have proposed a numerical detection strategy that provides quantitative indicators of whether a flow is in the appropriate asymptotic regime or not. This detection scheme, currently implemented only for a single space dimension, has then be used to design an asymptotically adaptive numerical method that, in fact, operates uniformly accurately and efficiently for arbitrary Mach number. A second application of these asymptotic results has been the extension of an existing standard zero-Mach-number flow solver to the weakly compressible regime. This extension addresses, in particular, the problem of long-wavelength acoustics, which is typically ignored in competing approaches. Our *ansatz* has led to a natural kind of 'multi-gridding': In the regime considered acoustic perturbations live on large length scales only, and are thus amenable to accurate representation on relatively coarse computational grids. The quasi-incompressible, vortical component of the flow field is active on much smaller length scales and is thus represented on a finer grid.

For the atmospheric flow and magneto-hydrodynamics problems we have described asymptotic analyses that provide the necessary insight for understanding characteristic failures of standard numerical schemes. Our current efforts are directed at exploiting these results in the construction of new numerical techniques along the lines described above.

Acknowledgments

The asymptotic analysis of slow atmospheric motions has been developed together with Dr. A. S. Almgren of Lawrence Berkeley National Lab. The numerical simulation of the flow in the stack of a thermo-acoustic refrigerator is part of a collaboration with Prof. Dr. O. Knio

of the Department of Mechanical Engineering of the Johns Hopkins University. We thank the Deutsche Forschungsgemeinschaft and the Potsdam Institut für Klimafolgenforschung for generously supporting our work.

References

1. W. Schneider, *Mathematische Methoden in der Strömungsmechanik*. Braunschweig: Vieweg (1979) 261 pp.
2. S. Klainerman and A. J. Majda, Compressible and incompressible fluids. *Comm. Pure Appl. Math.* 35 (1982) 629–651.
3. J. K. Hunter, A. Majda and R. Rosales, Resonantly interacting weakly nonlinear hyperbolic waves II. Several space variables. *Stud. Appl. Math.* 75 (1986) 187–226.
4. A. Majda, R. R. Rosales and M. Schönbek, A canonical system of integro-differential equations arising in resonant nonlinear acoustics. *Stud. Appl. Math.* 79 (1988) 205–262.
5. R. Klein and N. Peters, Cummulative effects of weak pressure waves during the induction period of a thermal explosion in a closed cylinder. *J. Fluid Mech.* 187 (1988) 197–230.
6. R. Klein, Semi-implicit extension of a Godunov-type scheme based on low Mach number asymptotics I: One-dimensional Flow. *J. Comp. Phys.* 121 (1995) 213–237.
7. Th. Schneider, N. Botta, R. Klein and K. J. Geratz, Extension of finite volume compressible flow sovers to multi-dimensional, variable density zero Mach number flow. *J. Comp. Phys.* 155 (1999) 248–286.
8. F. A. Williams, *Combustion Theory (2nd ed.)*. Menlo Park, CA: Benjamins Cummins (1985) 680 pp.
9. A. Majda and J. Sethian, The derivation and numerical solution of the equations for zero Mach number combustion. *Com. Sci. Techn.* 42 (1985) 185–205.
10. A. Meister, Asymptotic single and multiple scale expansions in the low Mach number limit. *SIAM J. Appl. Math.* 60 (1999) 256–271.
11. M. Oevermann, M. Berger, J. Goodman and R. Klein, A numerical method for two-phase incompressible flow with large density ratio and sharp interface resolution. *J. Comp. Phys.* (2000) submitted.
12. C. A. J. Fletcher, *Computational techniques for fluid-dynamics–Specific techniques for different flow categories*, Vol. 2. Berlin, Heidelberg: Springer (1997) 493 pp.
13. R. I. Issa, Solution of the implicily discretised fluid flow equations by operator-splitting. *J. Comp. Phys.* 62 (1985) 40–65.
14. J. Kim and P. Moin, Application of a fractional step method to incompressible Navier-Stokes equations. *J. Comp. Phys.* 59 (1985) 308–323.
15. S. V. Patankar, *Numerical Heat Transfer and Fluid Flow*. Hemisphere Publishing Corporation (1980) 197 pp.
16. H. Pichler, *Dynamik der Atmosphäre.* Mannheim, Wien, Zürich: bibliografisches Institut (1986) 459 pp.
17. A. E. Gill, *Atmosphere-Ocean Dynamics*. London: Academic Press (1982) 662 pp.
18. J. Pedlosky, *Geophysical Fluid Dynamics* (2nd ed.). Berlin, Heidelberg, New York: Springer (1987) 710 pp.
19. R. K. Zeytounian, *Asymptotic Modeling of Atmospheric Flows*. Heidelberg, Berlin, New York: Springer (1990) 396 pp.
20. R. K. Zeytounian, *Meteorological Fluid Dynamics. Lecture Notes in Physics* m5. Heidelberg, Berlin, New York: Springer (1991) 346 pp.
21. G. Doms and U. Schättler, *Nonhydrostatic Limited-Area LM (Lokal-Modell) of DWD: Part I, Scientific Documentation*. Offenbach: Deutscher Wetterdienst (1997) 169 pp.
22. G. Volpe, On the use and accuracy of cimpressible flow codes at low Mach numbers. AIAA Paper 91-1662 (1991).
23. J. L. Sesterhenn, *Zur numerischen Berechnung kompressibler Strömungen bei kleinen Mach-Zahlen*. PhD thesis Swiss Federal Institue of Technology, Diss. ETH No. 11334 (1995) 71 pp.
24. C. Viozat, Implicit upwind schemes for low Mach number compressible flows. INRIA 3084 (1997).
25. Th. Schneider, N. Botta, K. J. Geratz and R. Klein, Extension of finite volume compressible flow solvers to multi-dimensional, variable density zero Mach number flow. ZIB, Konrad-Zuse-Zentrum für Informationstechnik Berlin SC 98-31 (1998) and J. Comp. Phys. 155 (1999) 248–286.
26. N. Botta, R. Klein and A. S. Almgren, Dry atmosphere asymptotics. PIK Potsdam Institute for Climate Impact Research 55 Potsdam (1999).
27. D. R. Durran, *Numerical Methods for Wave Equations in Geophysical Fluid Dynamics*. New York, Berlin, Heidelberg: Springer (1999) 465 pp.

28. Y. Ogura and N. Phillips, Scale analysis for deep and shallow convection in the atmosphere. *J. Atmos. Sci*. 19 (1962) 173–179.
29. F. Lipps and R. Hemler, A scale analysis of deep moist convection and some related numerical calculations. *J. Atmos. Sci*. 29 (1982) 2192–2210.
30. M. van Dyke, *Perturbation Methods in Fluid Dynamics*. Stanford, CA: Parabolic Press (1975) 271 pp.
31. J. Kevorkian and J. D. Cole, *Perturbation Methods in Applied Mathematics*. New York, Heidelberg, Berlin: Springer (1980) 558 pp.
32. J. Kevorkian and J. D. Cole, *Multiple Scale and Singular Petrubation Methods*. New York, Berlin: Springer (1996) 632 pp.
33. A. Meister, Zur mathematischen Fundierung einer Mehrskalenanalyse der Euler-Gleichungen. *Hamburger Beiträge zur Angewandten Mathematik, Reihe F, Computational Fluid Dynamics and Data Analysis 1* (1997).
34. S. Schochet, Resonant nonlinear geometric optics for weak solutions of conversation laws. *J. Diff. Eqs.* 113 (1994) 106–231.
35. J. L. Joly, G. Métivier and J. Rauch, Resonant one-dimensional nonlinear geometric optics. *J. Funct. Anal*. 114 (1993) 106–231.
36. J. Weickert, A review of nonlinear diffusion filtering. *Scale-Space Theory in Computer Visions, Lecture Notes in Comp. Sciences* 1252 (1997) 3–28.
37. J. L. Latecki and R. Lakämper, Convexity rule for shape decomposition based on discrete contour evolution. *Comp. Vision Image Understanding* 73 (1999) 441–454.
38. J. L. Latecki and R. Lakämper, Polygon evolution by vertex deletion (1999). In preparation.
39. C.-D. Munz, S. Roller, R. Klein and K. J. Geratz, The extension of incompressible flow solvers to the weakly compressible regime. submitted to Comp. and Fluids (2000).
40. A. J. Chorin, A numerical method for solving incompressible viscous flow problems. *J. Comp. Phys.* 2 (1967) 12–26.
41. A. J. Chorin, Numerical solution of the Navier-Stokes equations. *J. Comp. Phys.* 22 (1968) 745–762.
42. R. Temam, Sur l'approximation de la solution des equations de Navier-Stokes par la methode des pas fractionaires. *Arch. Rat. Mech. Anal.* 32 (1969) 135–153.
43. P. M. Gresho, On the theory of semi-implicit projection methods for viscous incompressible flows and its implementation via a finite element method that also introduces a nearly consistent mass matrix. Part 1: Theory. *Int. J. Num. Meth. Fluids* 11 (1990) 587–620.
44. P. M. Gresho, On the theory of semi-implicit projection methods for viscous incompressible flows and its implementation via a finite element method that also introduces a nearly consistent mass matrix. Part 2: Implementation. *Int. J. Num. Meth. Fluids* 11 (1990) 621–659.
45. U. Ghia, K. Ghia and C. Shin, High-Re solutions for incompressible flow using the Navier-Stokes equations and a multigrid method. *J. Comp. Physics* 48 (1982) 387–411.
46. S. Schochet, Asymptotics for symmetric hyperbolic systems with a large parameter. *J. Diff. Eqs.* 75 (1988) 1–27.
47. R. Courant, K. O. Friedrichs and H. Lewy, Über die partiellen Differenzengleichungen der Physik. *Math. Ann.* 100 (1928) 32.
48. B. van Leer, Towards the ultimate conservative difference scheme. I. The quest of monotonicity. *Lect. Notes in Phys.* 18 (1973) 163–168.
49. B. van Leer, Towards the ultimate conservative difference scheme. II. Monotonicity and conservation combined in a second-order scheme. *J. Comp. Phys.* 14 (1974) 361–370.
50. B. van Leer, Towards the ultimate conservative difference scheme. III. Upstream-centered finite-difference schemes for ideal compressible flow. *J. Comp. Phys.* 23 (1977) 263–275.
51. B. van Leer, Towards the ultimate conservative difference scheme. IV. A new approach to nummerical convection. *J. Comp. Phys.* 23 (1977) 276–299.
52. B. van Leer, Towards the ultimate conservative difference scheme. V. A second-order sequel to Godunov's method. *J. Comp. Phys.* 32 (1979) 101–136.
53. B. Einfeldt, On Godunov type methods for gas dynamics. Inst. f. Geometrie u. Praktische Mathematik, RWTH Aachen, Bericht Nr. 41 (1986).
54. K. J. Geratz, *Erweiterung eines Godunov-Typ-Verfahrens für zwei-dimensionale kompressible Strömungen auf die Fälle kleiner und verschwindender Machzahl*. PhD thesis Rheinisch-Westfälische Technische Hochschule Aachen, D 82 (1997) 101 pp.

55. P. Wesseling, *An Introduction to multigrid methods*. Chichester: John Wiley & Sons (1991) 284 pp.
56. A. S. Almgren, J. B. Bell, P. Colella, L. H. Howell and M. L. Welcome, A conservative adaptive projection method for the variable density incompressible Navier-Stokes equations. Ernest Orlando Lawrence Berkeley National Laboratory LBNL-39075 (1996).
57. P. M. Gresho and S. T. Chan, On the theory of semi-implicit projection methods for viscous incompressible flow and its implementation via a finite element method that also introduces a nearly consistent mass matrix. Part 2: Implementation. *Int. J. Num. Meth. Fluids* 11 (1990) 621–659.
58. C. W. Schulz-Rinne, *The Riemann problem for two-dimensional gas dynamics and new limiters for high-order schemes*. PhD thesis Swiss Federal Institute of Technology, Diss. ETH No. 10297 (1993) 122 pp.
59. K. N. Ghia, U. Ghia and C. T. Shin, High-Resolutions for incompressible flow using the Navier-Stokes equations and a multigrid method. *J. Comp. Phys.* 48 (1982) 387–411.
60. W. Y. Soh and J. W. Goodrich, Unsteady solution of the incompressible Navier-Stokes equations. *J. Comp. Phys.* 79 (1988) 113–134.
61. C. H. Bruneau and C. Jouron, an efficient scheme for solving steady incompressible Navier-Stokes equations. *J. Comp. Phys.* 89 (1990) 389–413.
62. E. G. Puckett, A. S. Almgren, J. B. Bell, D. L. Marcus and W. J. Rider, A high-order projection method for tracking fluid interfaces in variable density incompressible flow. *J. Comp. Phys.* 130 (1997) 269–282.
63. A. S. Worlikar, O. M. Knio and R. Klein, Numerical simulation of a thermoacoustic refigerator. II stratified flow around the stack. *J. Comp. Phys.* 144 (1998) 299–324.
64. A. S. Worlikar and O. M. Knio, Numerical study of oscillatory flow and heat transfer in a loaded thermoacoustic stack. *Num. Heat Transf.* 35 (1999) 49–65.
65. Th. Schneider, R. Klein, E. Besnoin and O. Knio, Computational analysis of a thermoacoustic refrigerator. In: *Proceedings of the joint EAA/ASA meeting* March 1999.
66. H. A. van der Vorst, BI-CGSTAB: A fast and smoothly converging variant of BI-CG for the solution of nonsymmetric linear systems. *SIAM J. Sci. Stat. Comp.* 13 (1992) 631–644.
67. E. F. Toro, *Riemann Solvers and Numerical Methods for Fluid Dynamics*. Berlin, Heidelberg, New York: Springer (1997) 624 pp.
68. K. Lerbinger and J. F. Luciani, a new semi-implicit method for MHD computations. *J. Comp. Phys.* 97 (1991) 444–459.
69. O. S. Jones, U. Shumlak and D. S. Eberhardt, An implicit scheme for nonideal magnetohydrodynamics. *J. Comp. Physics* 130 (1997) 231–242.